ABSTRACT

Title of Thesis: THE DA VINCI AERIAL SCREW:
A CHARACTERIZATION OF THE
AERODYNAMICS, PERFORMANCE,
AND ACOUSTICS

Ron Berlin
Master of Science, 2026

Thesis Directed by: Igor Sikorsky Distinguished Professor,
Dr. James Baeder, Department of Aerospace Engineering

Aerial screw rotors are high-solidity rotors which rely on a shape-conforming helical vortex at the blade tip – the "da Vinci vortex" – as the primary thrust generation mechanism, analogous to vortex lift on delta wings. The geometry of an aerial screw is defined by key parameters such as the pitch rate (ζ), taper rate (η), number of blades (N_b), and the maximum radius ($R_{\max}$). Aerial screws generate higher thrust compared to conventional rotors at similar rotation speeds, with the cost of increased power requirements. This work employs a one-at-a-time approach to understand the effect of varying these design parameters on the aerodynamics, performance, and acoustics of aerial screws using high-fidelity computational fluid dynamics (CFD). The flight states investigated include hover, axial climb, and off-axis climb, primarily for aerial screws with a one-foot radius.

The maximum radius is found to positively contribute to the hover efficiency with diminishing returns at larger sizes, attributed to viscous effects becoming less significant at higher Reynolds

numbers. An increasing number of blades significantly decreases the figure of merit due to interactional aerodynamics weakening the da Vinci vortex. An optimal linear pitch rate of $\zeta = 1.2$ is found in hover, balancing vortex strength against the torque-wise orientation of the blade's surface normal vectors. This optimal pitch rate shifts upward with increasing climb speed, reaching $\zeta = 1.8$ at a climb inflow of $\lambda_c = 0.08$, as higher pitch rates better sustain the effective angle of attack against the increasing inflow. In off-axis climb, higher pitch rates produce significantly larger oscillatory side forces and pitching and rolling moments, presenting a key design tradeoff. The taper rate is found to be less influential than the pitch rate in axial and off-axis climb states, where its effect on efficiency becomes nearly negligible.

Bilinear variations of pitch and taper rates are explored in hover to further improve aerial screw performance beyond what linear distributions allow. A bilinear pitch distribution transitioning from $\zeta_1 = 1.0$ in the first half of the screw to $\zeta_2 = 1.4$ in the second half yields a modest improvement over the best linear pitch design. A bilinear taper distribution with an aggressive initial taper of $\eta_1 = 0.8$ transitioning to an untapered second half achieves a 5% improvement over the best linearly tapered design, by strongly feeding the da Vinci vortex in the first half while maximizing lifting area in the second. Combining the best bilinear pitch and bilinear taper profiles yields a figure of merit of 0.64 in hover — a 13.7% improvement over the best linearly varying design. While this aerial screw outperforms all other screw configurations studied, conventional rotors still achieve higher figures of merit in hover, ranging from 0.73 to 0.77.

Phase shifting in azimuthal loads was discovered between linear and bilinear varying designs due to the differencing in local surface inclinations and blade loadings. This finding suggests a potential optimal one-bladed aerial screw which is capable of canceling side forcing, rolling and pitching moments in hover.

An aeroacoustic analysis reveals that despite producing higher thickness noise levels than conventional rotors due to their distributed geometry, aerial screws exhibit significantly more favorable perceived noise characteristics. Their low $1/\mathrm{rev}$ blade passage frequencies result in tonal noise components that are heavily attenuated by A-weighting, and their continuous, distributed wake interactions produce a far less impulsive broadband noise signature compared to conventional rotors. The best performing aerial screw achieves total perceived noise levels comparable to a 4-bladed conventional rotor, with a distinctive directivity pattern that is quiet both in-plane and on-axis. These findings suggest a compelling acoustic advantage for aerial screw designs in noise-sensitive practical applications.

THE DA VINCI AERIAL SCREW: A CHARACTERIZATION OF THE AERODYNAMICS, PERFORMANCE, AND ACOUSTICS

by

Ron Berlin

Thesis submitted to the Faculty of the Graduate School of the
University of Maryland, College Park in partial fulfillment
of the requirements for the degree of
Master of Science
2026

Advisory Committee:
Professor James Baeder
Professor Anubhav Datta
Professor Chloe Johnson

© Copyright by
Ron Berlin
2026

Dedication

I dedicate this to my family, for guiding and supporting me at all points of this journey.

Acknowledgments

I would like to express my sincere gratitude to my advisor, Dr. James Baeder, for providing me with the opportunity to pursue such a fascinating topic of research. His support and guidance has been invaluable to the completion of my thesis and my education beyond the classroom.

Thank you to Dr. Datta and Dr. Johnson for their guidance and support in the classroom as well as in the pursuit of my thesis.

My colleagues at the High-Performance Computing Laboratory of the Alfred Gessow Rotorcraft Center have enhanced my undergraduate and graduate life in many ways. Dr. Bumseok Lee and Dr. Paulo Arias helped me begin my journey in Dr. Baeder's group and Dr. Koushik Marepally helped find new directions of research in this novel topic. A big thank you to the rest of my lab mates for providing indispensable guidance and support throughout my time at the University of Maryland.

I want to express my utmost thanks to my family. To my mother and father for constantly supporting me and pushing me to do things the right way, inside and outside of my academics. Also to my sisters for always providing unwavering guidance and support.

To all of my friends in College Park and those from home, thank you for all the laughs and good times we have shared over the years. The support you have provided me has been irreplaceable.

I would like to acknowledge financial support from Dr. Baeder during my pursuit of

bettering our understanding of the Da Vinci Aerial Screw.

Table of Contents

Dedication ii

Acknowledgements iii

Table of Contents v

List of Tables vii

List of Figures viii

Nomenclature xii

Chapter 1: Introduction to the Leonardo da Vinci Aerial Screw 1
- 1.1 History . . . 1
- 1.2 The Aerial Screw in the 21st Century . . . 4
  - 1.2.1 The da Vinci Vortex . . . 5
  - 1.2.2 Modern Designs . . . 7
  - 1.2.3 Recent Developments . . . 8
- 1.3 Motivation and Objectives . . . 10
- 1.4 Outline of the Thesis . . . 11

Chapter 2: Geometric Definition of the Aerial Screw 12
- 2.1 Rotor Radius . . . 13
- 2.2 Number of Blades . . . 13
- 2.3 Pitch Rate . . . 14
- 2.4 Taper Rate . . . 17
- 2.5 Anhedral and Dihedral . . . 17
- 2.6 Chapter Summary . . . 18

Chapter 3: Methodology of Study 19
- 3.1 Model Generation . . . 19
- 3.2 Meshing . . . 20
- 3.3 Solution Methodology . . . 22
  - 3.3.1 CFD Framework . . . 22
  - 3.3.2 Performance Analysis . . . 22
  - 3.3.3 Delayed Detached Eddy vs Euler Comparison . . . 23
  - 3.3.4 Grid Convergence Study . . . 28

3.4 Chapter Summary . . . 31

Chapter 4: Aerodynamics and Performance Impacts 33
4.1 Effect of Radius (R_{max}) . . . 36
4.2 Number of Blades (N_b) . . . 37
4.3 Pitch Rate (ζ) . . . 39
4.3.1 Linear Pitch Rate . . . 39
4.3.2 Bilinear Pitch Rate . . . 57
4.4 Taper Rate (η) . . . 64
4.4.1 Linear Taper Rate . . . 64
4.4.2 Bilinear Taper Rate . . . 81
4.5 Bilinear Pitch Bilinear Taper . . . 88
4.5.1 Hover . . . 88
4.6 Comparison of Best Performing Aerial Screws . . . 95
4.6.1 Geometry of the Conventional Rotor . . . 97
4.6.2 Investigation of Rotor Wake and Induced Velocities in Hover . . . 99
4.6.3 Performance Comparison of Screw S4 to Conventional Rotor in Axial and Off-Axis Flight . . . 106
4.7 Chapter Summary . . . 114

Chapter 5: Aeroacoustic Analysis of Aerial Screws 117
5.1 Thickness Noise . . . 118
5.2 Tonal Loading Noise (Steady Loads) . . . 121
5.3 Loading Noise (Unsteady Loads) . . . 124
5.4 Total Noise (Thickness and Loading) . . . 131
5.5 Chapter Summary . . . 134

Chapter 6: Discussion of Results 135
6.1 Discussion . . . 135
6.2 Future Considerations . . . 135
6.3 Conclusions . . . 136

Bibliography 139

Bibliography 139

List of Tables

3.1 Cell Count Variation of Aerial Screw Cases 21
3.2 Subiterations and Mathematical Model Study 24
3.3 Grid Convergence Study 29

4.1 Normalized force magnitudes and phase angles for Linear and Bilinear models . . 95
4.2 Different Aerial Screw Geometry Definitions 96
4.3 Comparison of the Operating Speeds, Rotor Sizes and Figures of Merit for Different Aerial Screws and Conventional Rotors 98

List of Figures

1.1 Leonardo's Aerial Screw Depicted in the Page of Paris Manuscript B, Folio 83v . 1
1.2 Concept design with aerial screw style rotor blades developed by Enrico Forlani in 1877. 2
1.3 Full scale helicopter designed and built by Paul Cornu in 1907. 3
1.4 Aerial screw 3D printed test rig used by RMIT in 2014. 4
1.5 Iso-surfaces of vorticity Q-criterion around a notional hovering aerial screw (left: side view, right: top view) 6
1.6 University of Maryland graduate team's aerial screw manned quadrotor. 7
1.7 Technical University of Delft undergraduate team's ducted aerial screw manned vehicle. 8
1.8 UMD Aerial Screw Quadrotor by Prete. 9
1.9 UMD Aerial Screw Quadrotor in Flight by Prete. 9

2.1 Design Variables Defining the Geometry of an Aerial Screw 12
2.2 Axial Component of the Local Surface Unit Normal Vector for Screws with Different Pitch and Taper Rates, Illustrating Contributions of Pressure to Thrust Generation 16

3.1 SolidWorks CAD Model of Linearly Pitched ($\zeta = 1.2$) and Linearly Tapered ($\eta = 0.5$) Aerial Screw 20
3.2 Pointwise Unstructured Surface Mesh of Linearly Pitched ($\zeta = 1.2$) and Linearly Tapered ($\eta = 0.5$) Aerial Screw 21
3.3 Thrust coefficient variation with subiterations for DDES and Euler models 25
3.4 Power coefficient variation with subiterations for DDES and Euler models 25
3.5 Figure of merit variation with subiterations for DDES and Euler models 26
3.6 L2 Norm of Residual vs Iteration for Nearbody Mesh 27
3.7 L2 Norm of Residual vs Iteration for Nested Mesh 27
3.8 L2 Norm of Residual vs Iteration for Farfield Mesh 28
3.9 Thrust coefficient variation with nearbody mesh cell count in hover for best bilinearly tapered aerial screw 30
3.10 Power coefficient variation with nearbody mesh cell count in hover for best bilinearly tapered aerial screw 30
3.11 Figure of merit variation with nearbody mesh cell count in hover for best bilinearly tapered aerial screw 31

4.1 Axial flow iso-surfaces of vorticity Q-criterion ($\zeta = 1.4$ linear pitch case) 34
4.2 Off-axis iso-surfaces of vorticity Q-criterion ($\zeta = 1.4$) (Left: Side view, Right: Isometric view) 35
4.3 Variation of Figure of Merit for Screws of different sizes 36
4.4 Variation of figure of merit with number of blades 37
4.5 Vorticity contours showing the decreased strength of daVinci vortex with increasing number of blades in the screw ($N_b = 1$ - top left, $N_b = 2$ - top right, $N_b = 3$ - bottom middle) 38
4.6 Variation of figure of merit of aerial screws with varying pitch rate 40
4.7 ΔC_P contours for aerial screws with different pitch rates: Top left: $\zeta = 1$, Top right $\zeta = 1.2$ and Bottom left: $\zeta = 1.5$ 41
4.8 Axial component of ΔC_P contours for aerial screws with different pitch rates: Top left: $\zeta = 1$, Top right $\zeta = 1.2$ and Bottom left: $\zeta = 1.5$ 42
4.9 Torque-wise component of ΔC_P contours for aerial screws with different pitch rates: Top left: $\zeta = 1$, Top right $\zeta = 1.2$ and Bottom left: $\zeta = 1.5$ 43
4.10 Vorticity contour of the $\zeta = 1.2$ linearly pitched design 44
4.11 Vorticity contour of the $\zeta = 2.0$ linearly pitched design 45
4.12 Pressure distribution of the $\zeta = 1.2$ linear pitch design 46
4.13 Pressure distribution of the $\zeta = 2.0$ linear pitch design 47
4.14 Variation of figure of merit of aerial screws with varying pitch rate in hover 48
4.15 C_T of optimal linear pitch screw ($\zeta = 1.2$) for varying axial climb speeds 49
4.16 C_P of optimal linear pitch screw ($\zeta = 1.2$) for varying axial climb speeds 50
4.17 FM^* of optimal linear pitch screw ($\zeta = 1.2$) for varying axial climb speeds 50
4.18 Variation of FM^* for varying linear pitch rates at different axial climb speeds 51
4.19 CF_X as a function of azimuth for varying pitch rates in off-axis flight 54
4.20 CF_Y as a function of azimuth for varying pitch rates in off-axis flight 54
4.21 CF_Z as a function of azimuth for varying pitch rates in off-axis flight 55
4.22 CM_X as a function of azimuth for varying pitch rates in off-axis flight 55
4.23 CM_Y as a function of azimuth for varying pitch rates in off-axis flight 56
4.24 CM_Z as a function of azimuth for varying pitch rates in off-axis flight 56
4.25 Variation of figure of merit of aerial screws with varying bilinear pitch rates 58
4.26 Surface load projections onto $r' - \theta$ plane for the bilinear pitch screw with $\zeta = 1$ for upstream half and $\zeta = 1.4$ for downstream half, Top left: ΔC_P, Top right: Axial component and Bottom left: Torque-wise component 59
4.27 Vorticity contour of the $\zeta = 1.0$ to $\zeta = 1.4$ bilinear pitch design 60
4.28 Vorticity contour of the $\zeta = 0.8$ to $\zeta = 1.6$ bilinear pitch design 61
4.29 Pressure distribution of the $\zeta = 1.0$ to $\zeta = 1.4$ bilinear pitch design 62
4.30 Pressure distribution of the $\zeta = 0.8$ to $\zeta = 1.6$ bilinear pitch design 63
4.31 Variation of figure of merit of aerial screws with varying taper rate 65
4.32 Surface load projections onto $r' - \theta$ plane for aerial screw with $\zeta = 1.3$ and $\eta = 0.5$, Top left: ΔC_P, Top right: Axial component and Bottom left: Torque-wise component 66
4.33 Surface load projections onto $r' - \theta$ plane for aerial screw with $\zeta = 1.3$ and $\eta = 0.67$, Top left: ΔC_P, Top right: Axial component and Bottom left: Torque-wise component 67

4.34 Vorticity contour of the $\eta = 0.5$ linear taper rate design . . . 69
4.35 Vorticity contour of the $\eta = 0.66$ linear taper rate design . . . 70
4.36 Pressure distribution of the $\eta = 0.5$ linear taper design . . . 71
4.37 Pressure distribution of the $\eta = 0.66$ linear taper design . . . 72
4.38 Variation of figure of merit of aerial screws with varying pitch rate in hover . . . 73
4.39 Variation of C_T and C_P for varying linear taper rates at different axial climb speeds 74
4.40 Variation of FM^* for varying linear taper rates at different axial climb speeds . . 76
4.41 CF_X as a function of azimuth for varying taper rates in off-axis flight . . . 78
4.42 CF_Y as a function of azimuth for varying taper rates in off-axis flight . . . 78
4.43 CF_Z as a function of azimuth for varying taper rates in off-axis flight . . . 79
4.44 CM_X as a function of azimuth for varying taper rates in off-axis flight . . . 79
4.45 CM_Y as a function of azimuth for varying taper rates in off-axis flight . . . 80
4.46 CM_Z as a function of azimuth for varying taper rates in off-axis flight . . . 80
4.47 Variation of figure of merit of bilinearly tapered aerial screws with varying initial taper rate . . . 82
4.48 Surface load projections onto $r' - \theta$ plane for aerial screw with $\zeta = 1.3$ and bilinear taper with $\eta_1 = 0.8$, Top left: ΔC_P, Top right: Axial component and Bottom left: Torque-wise component . . . 83
4.49 Vorticity contour of the $\eta = 0.8$ initial taper rate design . . . 84
4.50 Vorticity contour of the $\eta = 1.33$ initial taper rate design . . . 85
4.51 Pressure distribution of the $\eta = 0.8$ initial taper design . . . 86
4.52 Pressure distribution of the $\eta = 1.33$ initial taper design . . . 87
4.53 Variation of figure of merit of bilinearly tapered aerial screws with varying initial pitch rate . . . 89
4.54 Variation of figure of merit of bilinearly tapered aerial screws with varying initial taper rate . . . 90
4.55 Vorticity contour of the bilinearly pitched and bilinearly tapered design . . . 91
4.56 Pressure distribution of the bilinearly pitched and bilinearly tapered design . . . 92
4.57 Nondimensional side force (CF_X) in hover comparing a $\zeta = 1.2$ linearly pitched screw and the bilinear screw . . . 93
4.58 Surface Pressure Difference (ΔC_P) across Top and Bottom Surfaces for Screws S1 (top left), S2 (top right), S3 (bottom left) and S4 (bottom right) . . . 97
4.59 Azimuthal Average Wake Velocity Profiles for the Screw S1: Top: Axial Velocity; Middle: Radial Velocity; Bottom: Swirl Velocity . . . 100
4.60 Instantaneous Axial Wake Velocity Profile for Screw S4 at an Axial Location 50% Below Trailing Edge . . . 102
4.61 Instantaneous Radial Wake Velocity Profile for Screw S4 at an Axial Location 50% Below Trailing Edge . . . 102
4.62 Instantaneous Swirl Wake Velocity Profile for Screw S4 at an Axial Location 50% Below Trailing Edge . . . 103
4.63 Instantaneous Wake Vorticity Iso-contours showing Asymmetry and Wake Drifting 104
4.64 Azimuthal Average Wake Velocity Profiles for Different Screws at 50% $R_{\max}$ Axial Station: Top: Axial Velocity; Middle: Radial Velocity; Bottom: Swirl Velocity . . . 105

4.65 Variation of C_T and C_P with axial climb speed for the bilinear screw and conventional rotor . . . 108
4.66 Variation of FM^* with axial climb speed for the bilinear screw and conventional rotor . . . 109
4.67 Conventional rotor propulsive force coefficient (CF_X) as a function of the azimuth in off-axis flight . . . 110
4.68 CF_X as a function of azimuth for comparison to a conventional rotor . . . 111
4.69 CF_Y as a function of azimuth for comparison to a conventional rotor . . . 111
4.70 CF_Z as a function of azimuth for comparison to a conventional rotor . . . 112
4.71 CM_X coefficients as a function of azimuth for comparison to a conventional rotor 112
4.72 CM_Y coefficients as a function of azimuth for comparison to a conventional rotor 113
4.73 CM_Z coefficients as a function of azimuth for comparison to a conventional rotor 113

5.1 Directivity of Thickness Noise (p'_{rms} vs θ), Top: Screws S1, S2, S3 and S4 vs Conventional Rotor C4.1, Bottom: Screw S4 vs Conventional Rotors C2.1, C2.2, C4.1 and C4.2 . . . 119
5.2 Thickness Noise Waveforms for Observer at $\theta = -30°$ for different Rotors . . . 120
5.3 Directivity of Loading Noise due to Steady Loads (p'_{rms} vs θ), Top: Screws S1, S2, S3 and S4 vs Conventional Rotor C4.1, Bottom: Screw S4 vs Conventional Rotors C2.1, C2.2, C4.1 and C4.2 . . . 122
5.4 Loading Noise Waveforms (Steady Loads) for Observer at $\theta = -30°$ for different Rotors . . . 123
5.5 Contours of the RMS fluctuations of Surface Pressure Coefficient for Screws S1, S2, S3 and S4 . . . 125
5.6 Directivity of Loading Noise due to Unsteady Loads (Steady and Blade Wake Interactions combined) (p'_{rms} vs θ), Top: Screws S1, S2, S3 and S4 vs Conventional Rotor C4.1, Bottom: Screw S4 vs Conventional Rotors C2.1, C2.2, C4.1 and C4.2 127
5.7 Loading Noise Waveforms (Steady vs Unsteady Loads) for Observer at $\theta = -30°$ for Rotors S1, C2.1 and C4.1 . . . 128
5.8 Spectral Decomposition of Loading Noise at Observer located at $\theta = -30°$ for Rotors S4, C2.1 and C4.1, Top - Sound Pressure Level (SPL) and Bottom - Perceived Noise Level (A-weighted SPL) . . . 130
5.9 Total Noise Directivity for Different Rotors (SPL (dB)) . . . 132
5.10 Total Perceived Noise Levels for Different Rotors (PNL (dBA)) . . . 133

Nomenclature

ΔC_P ..... Pressure differential

Δs ..... Wall spacing

η ..... Taper rate

λ_c ..... Climb inflow

λ_i ..... Induced inflow

ψ ..... Angle of azimuth

σ ..... Rotor solidity

θ ..... Local radial station on screw surface

ζ ..... Pitch rate

CF_X ..... Force coefficient in x direction

CF_Y ..... Force coefficient in y direction

CF_Z ..... Force coefficient in z direction

CM_X ..... Moment coefficient in x direction

CM_Y ..... Moment coefficient in y direction

CM_Z ..... Moment coefficient in z direction

C_P ..... Power coefficient

C_T ..... Thrust coefficient

FM ..... Figure of merit

FM^* ..... Modified figure of merit

M_{tip} ..... Tip mach number

N_b ..... Number of blades

p'_{rms} ..... Root mean square of acoustic pressure

R_{max} ..... Maximum radius

Re ..... Reynolds number

r' ..... Nondimensional radial coordinate

SPL ..... Sound pressure level

$\frac{t}{t_{Rev}}$ ..... Normalized time

v_r ..... Radial velocity

v_θ ..... Tangential/swirl velocity

v_z or w ..... Axial velocity

y^+ ..... Nondimensional wall spacing

Chapter 1: Introduction to the Leonardo da Vinci Aerial Screw

1.1 History

The aerial screw is one of the earliest concepts for vertical flight, tracing back to the ingenious mind of Leonardo da Vinci from the late 15th century. da Vinci envisioned a helical, screw-like device, as shown in Figure 1.1, that could generate lift by screwing into the air—an idea preceding the existing technology at the time.



Figure 1.1: Leonardo's Aerial Screw Depicted in the Page of Paris Manuscript B, Folio 83v

Three hundred years later, the construction of a high-solidity helicopter was one of the first attempts in translating this concept into functioning technology [1]. Shown in Figure 1.2, Enrico Forlani came up with a concept rotorcraft with coaxial counter-rotating rotors, with aerial screw blade like features.

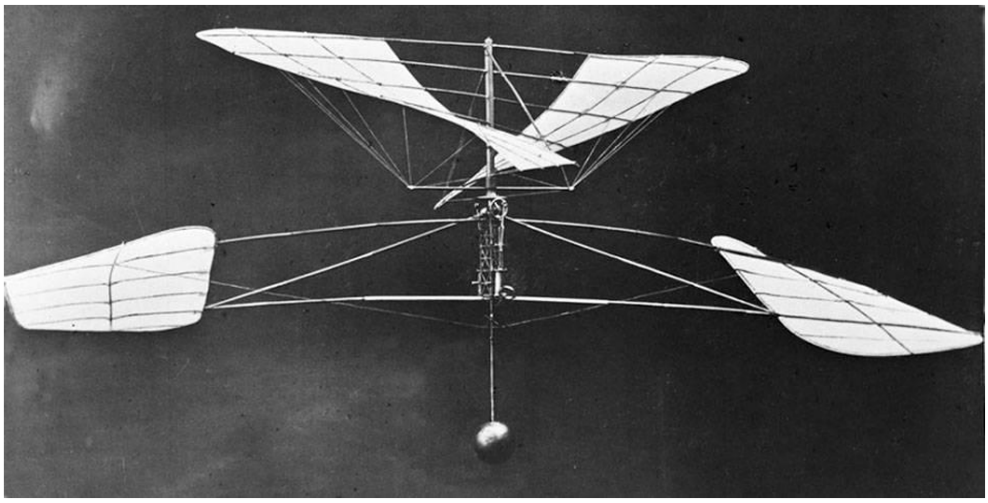

Figure 1.2: Concept design with aerial screw style rotor blades developed by Enrico Forlani in 1877.

Thirty years after, Paul Cornu came up with a novel rotorcraft design as shown in Figure 1.3. Cornu introduced a counter-rotating rotor system as well. Cornu's design drew inspiration from da Vinci's aerial screw with a rotor of relatively large solidity and the flat plate profiles of the blades. It was recorded that Cornu's machine was able to hop 5 meters into the air which was thanks to the, unknown at the time, ground effect. Despite other designs similar to Forlani's and Cornu's being created around the same time, the physics behind screw-type propellers remained inconclusive due to limitations in materials, fabrication techniques, and measurement accuracy [2].

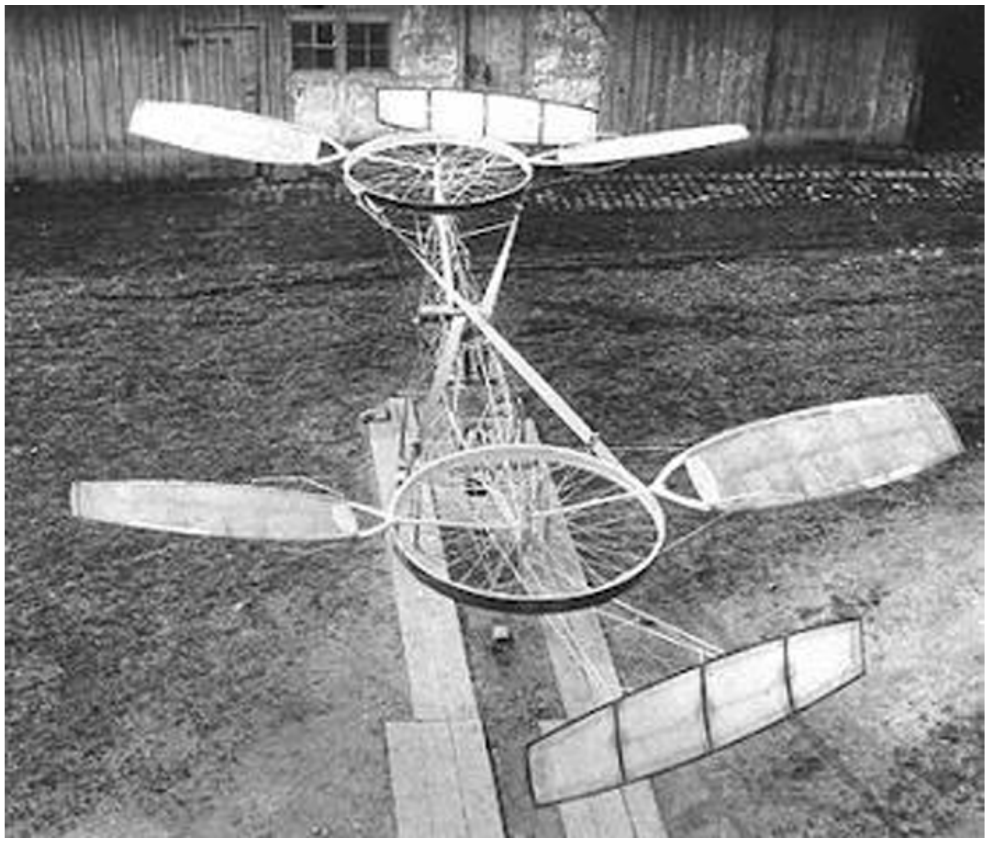

Figure 1.3: Full scale helicopter designed and built by Paul Cornu in 1907.

As the field of vertical lift matured, aerial screws were largely set aside in favor of more practical rotor designs. Conventional helicopters, characterized by low solidity rotors with high aspect ratio blades based on aerodynamic airfoils, demonstrated far superior efficiency and controllability. The figure of merit (FM) of conventional rotors have reach values of over 0.7 today, significantly higher than preliminary aerial screw designs. The figure of merit is defined below.

$$FM = \frac{Power_{ideal}}{Power_{actual}} = \frac{C_T^{3/2}}{\sqrt{2}C_P} \tag{1.1}$$

These rotors became the standard for vertical flight, and as a result, aerial screw concepts faded from serious consideration for several decades.

1.2 The Aerial Screw in the 21st Century

In recent years, aerial screws began reappearing across the field of vertical lift. In 2014, Dorrington *et al*. performed preliminary thrust testing through experiment and numerical simulations on a 0.5 m helical screw based on the sketch of da Vinci's rotor [3]. The rotor tested was a one bladed aerial screw with 1.5 turns of the blade around the axis of rotation. Experiment showed issue with balancing the mass of the rotor on the axis of rotation given the one bladed configuration. Numerical simulation revealed complex flow phenomena similar to marine propellers.

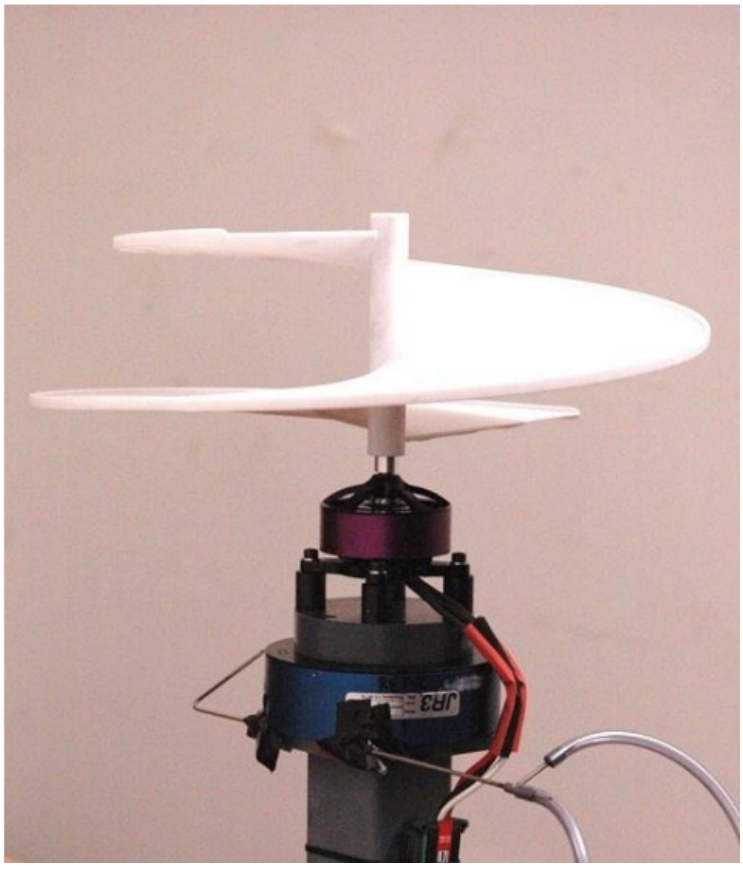

Figure 1.4: Aerial screw 3D printed test rig used by RMIT in 2014.

In 2020, the Vertical Flight Society's (VFS) Annual Design Competition hosted by Leonardo revisited the aerial screw [4], which encouraged innovative approaches to vertical flight vehicles.

At Maryland, a fundamental understanding of the aerial screw began with the work of James Sutherland and his graduate design team. The team fabricated many aerial screw geometries and tested them. Some of the geometries, not all, generated thrust, and it was a mystery as to why. After all likely sources of experimental error were discarded, it was conjectured that a screw with a sharp leading edge created a shape-conforming helical vortex at the edge of the screw, similar to a delta wing. Additionally, it was found that screws with progressively widening spirals kept the vortex on the top surface of the blade. This vortex would provide suction, hence lift. It also explained why past efforts failed. For structures that did not widen, the vortex would flow out from the screw surface. In deference to the master, this hypothetical vortex, if it existed, was called the da Vinci vortex.

1.2.1 The da Vinci Vortex

At the time of these investigations, flow visualization was available. The task fell on Koushik Marepally, the CFD member of the team modeled the screw and demonstrated the da Vinci vortex did indeed exist. It was found that the strength of this vortex determines the pressure distribution on the screw's surface and, consequently, the rotor's efficiency. Leveraging the use of modern modeling and simulation tools, the current study aims to unravel the effects of different design variables on the "da Vinci" vortex and the overall efficiency of the aerial screw.

A detailed understanding of the thrusting mechanism within aerial screws is achieved through Computational Fluid Dynamics (CFD)-driven discovery of the flow physics. Illustrated in Figure 1.5, the vorticity iso-surface in the flow field show a shape-conforming helical vortical structure on the top surface of a hovering aerial screw. This vortex induces suction, generating

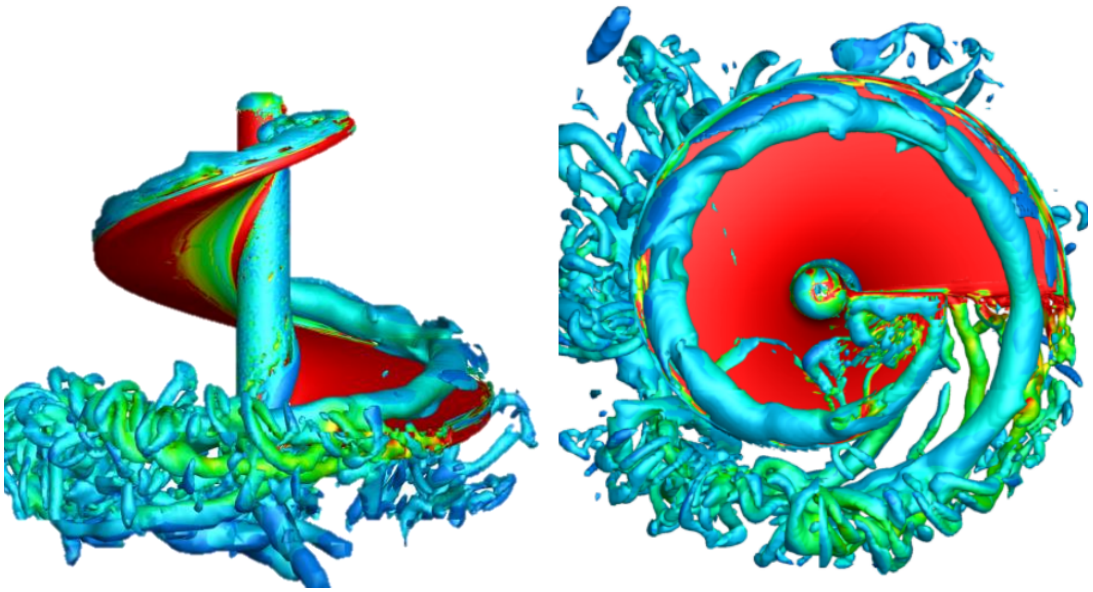

Figure 1.5: Iso-surfaces of vorticity Q-criterion around a notional hovering aerial screw (left: side view, right: top view)

a substantial pressure disparity across the screw surface and consequently contributing to an effective thrust component.

The initiation of the vortical structure's development occurs due to a circulation along the leading edge, where the screw edge meets the freestream. Subsequently, the span-wise vortex moves downstream and rolls up along the screw surface, resulting in the formation of a tip vortex. Further, the presence of taper on the screw surface creates a delta wing-like aerodynamic environment, continuously adding to the strength of the vortex along the blade tip, resulting in a shape conforming helical vortical structure viz. the da Vinci vortex. This increases the proportion of the screw surface active in thrust generation. However, it must be noted that the inboard sections of the screw surface exhibit a comparatively insignificant contribution to the overall thrust generation.

1.2.2 Modern Designs

Responding to this challenge, a series of contemporary designs were meticulously developed, directly inspired by the classical aerial screw concept [5]. These modern interpretations focused primarily on simple hovering missions, leveraging advanced computational tools and experimental methods to explore the fundamental aerodynamics of aerial screws with greater rigor and precision. This renewed exploration marked a significant leap forward, bridging the historical legacy of da Vinci's vision with state-of-the-art engineering practices. Shown below are final design configurations from the University of Maryland, College Park and the Technical University of Delft graduate and undergraduate teams, respectively, in Figures 1.6 and 1.7.

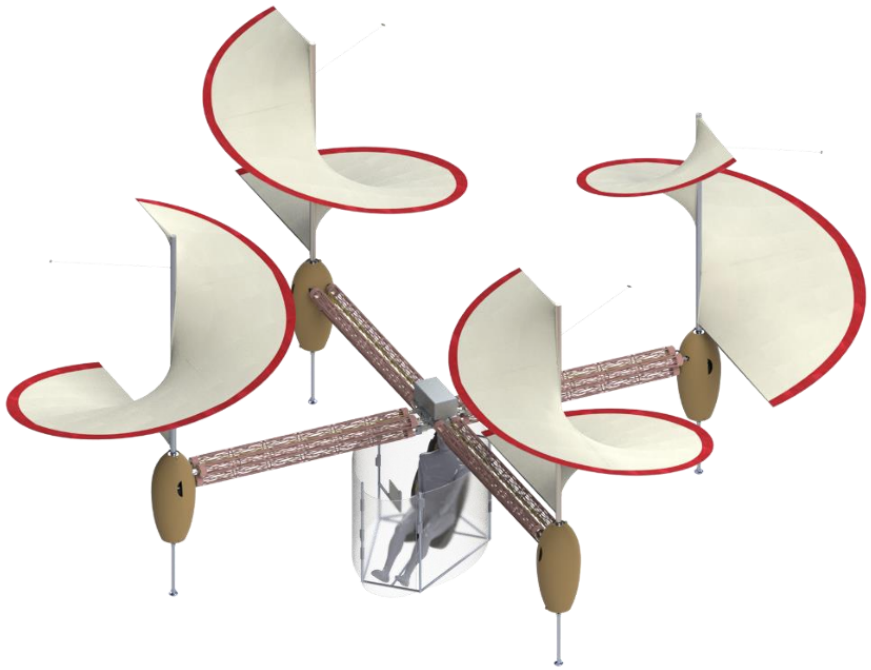

Figure 1.6: University of Maryland graduate team's aerial screw manned quadrotor.



Figure 1.7: Technical University of Delft undergraduate team's ducted aerial screw manned vehicle.

1.2.3 Recent Developments

The only remaining task was to stabilize the screw. This was accomplished with a vibration mass. The quadrotor configuration also helped with this. The culmination of these efforts was the creation of functional small-scale UAV prototypes employing aerial screw rotors [6,7]. These prototypes served as compelling proof-of-concept demonstrations, validating the aerial screw's ability to generate meaningful thrust. Preliminary studies reported figures of merit up to 0.52 [5], revealing the surprising efficiency potential of these unconventional rotors, particularly for applications requiring vertical take-off and landing (VTOL) or sustained hovering. Figure 1.8 shows the quadrotor build by Austin Prete at UMD with Figure 1.9 captures the quadrotor in flight during an indoor test. Prete's work was one of the first designs implementing aerial screw rotors which flew with up to date technology on board the aircraft to track thrust and power outputs. He used the aerial screw geometry which produced maximum lift. There was no vibration mass

included, but the precision control of the speeds with electric motors, balanced the rotors to a satisfactory degree and prodcued free flight. The aerial screw quadrotor has opened the door for continued exploration into the aerodynamics and performance of aerial screws, suggesting potential future applications in the field of vertical flight.



Figure 1.8: UMD Aerial Screw Quadrotor by Prete.

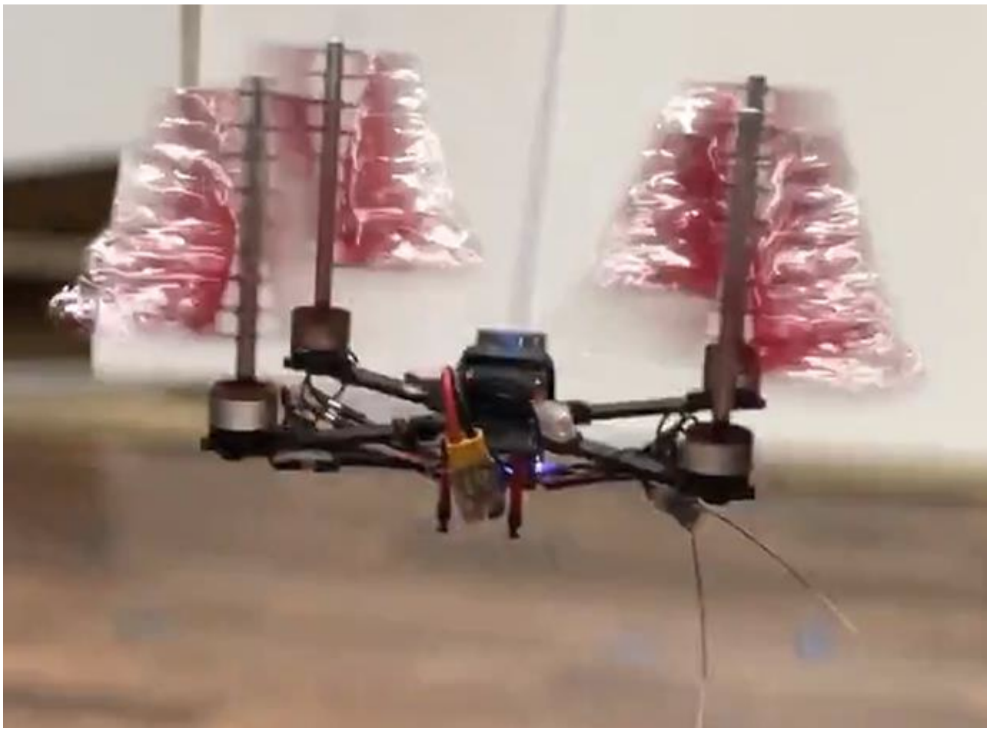

Figure 1.9: UMD Aerial Screw Quadrotor in Flight by Prete.

More recently, further computational investigations have been completed on da Vinci's aerial screws aerodynamics and acoustics at John's Hopkins University [8]. It was found that aerial screws require lower rotational speeds to achieve similar thrust values compared to a canonical two-bladed flat plate rotor. The single bladed aerial screw was found to mitigate blade-vortex interaction (BVI) noise which is a key contributor to rotor aeroacoustics. It is important to note a two-bladed flat plate rotor is to be expected to perform poorly compared to conventional rotor with a linear twist distribution with a well designed airfoil for rotorcraft applications.

1.3 Motivation and Objectives

Early designs inspired by the da Vinci aerial screw have paved the way for modern variations of da Vinci's vision from the late 1500s. Recent works have shown that there is promise for applications in the field of rotorcraft today using aerial screws, specifically in low-scale UAV applications.

Thus, after 500 years, precise model testing, imagination, modern CFD, and electric motor driven multi-rotors gave da Vinci perhaps what he was looking for.

The UMD design report was only the beginning. Much needed to be learned about the flow – exactly how is the vortex formed, where does it lie on the screw, for how long before it dissipates, and what makes it strong. This thesis is dedicated to finding the answer to these questions.

A one-at-a-time approach using high fidelity 3D Computational Fluid Dynamics assesses the effect of varying design parameters of aerial screws on the performance, aerodynamics, and acoustic signatures. Parameter sweeps are applied in determining the effects on the figure of

merit and climb efficiency, as well as off-axis climb performance. An in depth investigation of the resulting aerodynamics from these parameter sweeps yields insights into the lifting phenomena of aerial screw rotors, identifying key features necessary in improving performance. Additionally, the acoustic signatures of various aerial screw rotors are compared to conventional rotors in order to assess the potential benefits of high solidity aerial screws.

1.4 Outline of the Thesis

The organization of this thesis follows the introduction with Chapter 2, describing the geometry of the aerial screw, defining key design parameters. Chapter 3 gives the methodology of the study, describing the model generation, meshing techniques, and the Computational Fluid Dynamics (CFD) framework. A comparison of different mathematical models and a grid convergence study is included. Chapter 4 describes the aerodynamics and performance of aerial screw rotors. Each design variable which heavily effects the aerodynamics is explored in depth. Comparisons are drawn between aerial screws and conventional rotors in multiple flight conditions. Chapter 5 explores the aeroacoustics of aerial screw rotors, drawing comparisons to several conventional rotors. Chapter 6 concludes this work with the discussion of results and future considerations.

Chapter 2: Geometric Definition of the Aerial Screw

This chapter describes the geometry of the aerial screw, which is defined by its radius, pitch, and number of turns. The pitch rate of the screw is the axial length the screw surface advances in one full rotation. The radius is the distance from the screw centerline to the projected edge of the screw surface perpendicular to the axial direction. The number of turns refers to the total number of full rotations of the screw surface in the azimuthal direction. To avoid the impracticality of long, towering screws, the number of turns is set to 1 throughout this research.

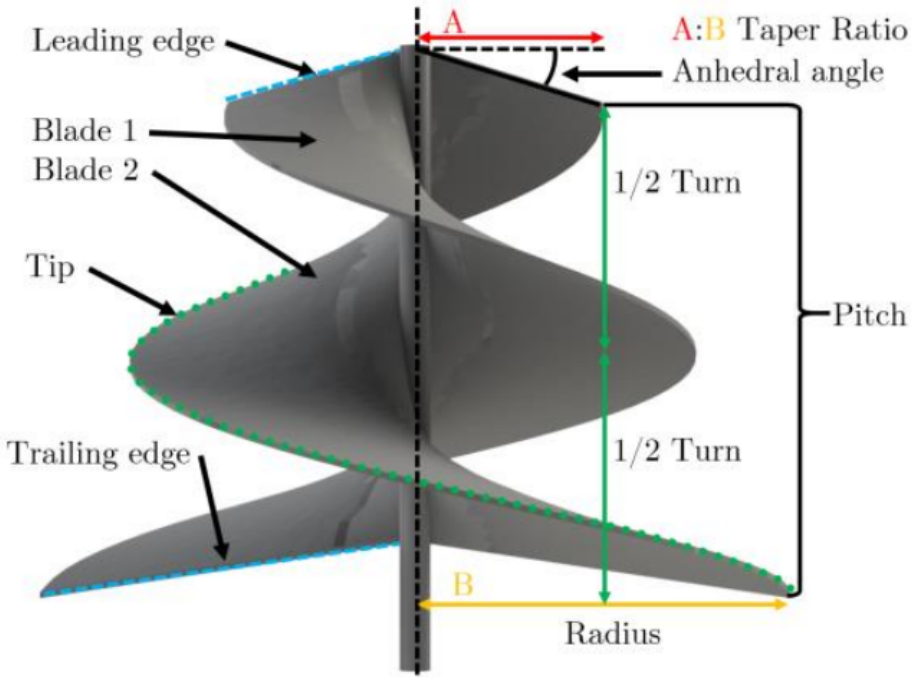

Figure 2.1: Design Variables Defining the Geometry of an Aerial Screw

Modern variations aerial screws involve a taper rate and dihedral angle between the screw and the axial plane. The taper rate is defined as the ratio between the local screw radii across one full turn. The taper represents the widening local radius crucial for sustaining lift. Figure 2.1 shows the different design variables that define an aerial screw geometry. This study excludes the effects of the dihedral angle on screw aerodynamics.

2.1 Rotor Radius

The radius of the screw is defined based on its projection perpendicular to the screw axial direction. Since the local radius may vary due to taper, the radius is defined at the maximum radius location, denoted as $R_{\max}$, corresponding to the trailing edge. This value is used as the primary length scale for non-dimensionalization of other quantities, and the corresponding disc area is used as the reference surface area for aerodynamic coefficients.

A local non-dimensionalization of the radial coordinate is also employed based on R_{local}, the maximum local radius at a given azimuthal station:

$$r' = \frac{r}{R_{\text{local}}} \tag{2.1}$$

2.2 Number of Blades

The number of blades impacts both aerodynamic performance and structural dynamics. Increasing the number of blades improves thrust uniformity and reduces aerodynamic loading fluctuations. A single-bladed screw minimizes aerodynamic interaction but suffers from severe imbalance issues, as the center of mass shifts away from the rotation axis, inducing hub vibrations

and large in-plane moments. A two-bladed configuration restores balance by counterweighting the masses, albeit at the expense of poor drag characteristics while three-bladed screws further reduce in-plane inertial moments.

This study compares the aerodynamic characteristics of single-, two-, and three-bladed aerial screws.

2.3 Pitch Rate

The screw pitch rate defines the axial advancement of the screw surface per full rotation. For a screw with linear pitch, the advancement per unit azimuthal angle is constant. However, non-uniform pitch rates, where the advancement varies with azimuthal orientation, are also possible. This study considers two variations: uniform (linear pitch) and bilinear pitch. In the bilinear case, the screw maintains two different constant pitch rates over the first and second halves of its turn.

The pitch rate is non-dimensionalized using the maximum radius, $R_{\max}$. If a screw has a pitch rate ζ, then the axial advancement over a ΔN rotation is $R_{\max}\zeta\Delta N$. The relationship is expressed as:

$$\zeta = \frac{1}{R_{\max}}\frac{\Delta Z}{\Delta N} = \frac{2\pi}{R_{\max}}\frac{\Delta Z}{\Delta \theta} \tag{2.2}$$

Because the pitch rate is constant, both inboard and outboard sections advance the same axial distance per unit azimuth. However, due to variation in local radius, especially with taper, the inboard sections have a steeper surface gradient compared to the outboard sections, affecting the local contributions to axial thrust. Increasing the pitch rate overall results in a steeper surface inclination, decreasing the component of normal force contributing to axial thrust and increasing

the component aligned with rotational torque. That is, even a stronger pressure gradient across the screw surface will not produce larger thrusts due to the orientation of the surface normal vectors.

Figure 2.2 shows the axial component of the surface normal vector for screws with different pitch rates, illustrating the reduction in axial contribution for a higher pitch rate ($\zeta = 1.3$) compared to a lower pitch rate ($\zeta = 1$). These figures are projected onto the $r' - \theta$ plane, where r' is the locally non-dimensionalized radius, and θ corresponds to the clockwise azimuthal orientation (since the screw rotates counter-clockwise). The azimuth $\theta = 0$ corresponds to the leading edge of the screw surface, reaching the trailing edge after a full clockwise rotation.

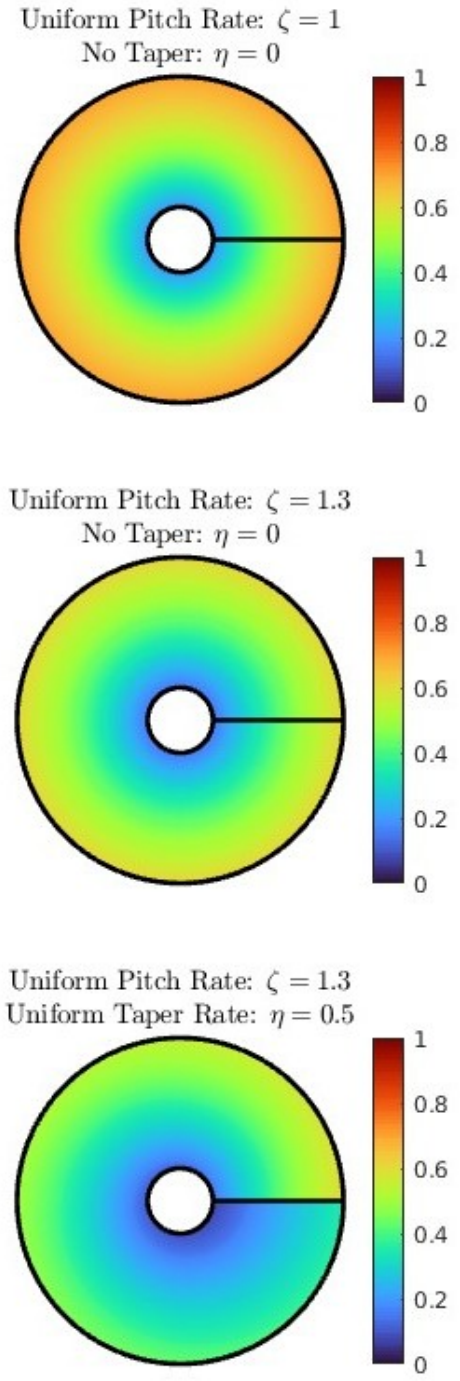

Figure 2.2: Axial Component of the Local Surface Unit Normal Vector for Screws with Different Pitch and Taper Rates, Illustrating Contributions of Pressure to Thrust Generation

2.4 Taper Rate

The screw taper rate is defined as the reduction in the local tip radius, R_{local}, over one full rotation. For a linearly tapered screw, the reduction in radius per unit azimuthal angle is constant. Similar to pitch, non-uniform taper rates are possible; this study considers both uniform (linear taper) and bilinear taper variations.

The taper rate is non-dimensionalized using the maximum radius:

$$\eta = \frac{1}{R_{\text{max}}} \frac{\Delta R_{\text{local}}}{\Delta N} = \frac{2\pi}{R_{\text{max}}} \frac{\Delta R_{\text{local}}}{\Delta \theta} \tag{2.3}$$

For a uniformly tapered screw, the upstream sections (near the leading edge) have a smaller local radius compared to downstream sections (near the trailing edge). Maintaining the same pitch rate, the surface gradient is steeper upstream, influencing how much local blade-normal forces contribute to the axial thrust.

Figure 2.2 also compares the axial component of the surface normal vector for screws with and without taper, at constant pitch rate, highlighting the reduced contribution from the upstream sections.

2.5 Anhedral and Dihedral

Anhedral and dihedral define the orientation of the leading edge perpendicular to the direction of rotation of the blades. Anhedral and dihedral effects remain to be thoroughly investigated, although some experimental work has already been done through the University of Maryland through the VFS Student Design competition as previously mentioned [5].

2.6 Chapter Summary

This chapter introduced the geometry of the aerial screw, defining variables such as pitch (ζ) and taper (η) rates, along with the number of blades (N_b) and maximum radius of the screw (R_{max}). This chapter provides an introduction to the pitch and taper rates by discussing the effects of each variable on the surface normal vectors of the aerial screw. The aerodynamic and performance implications are discussed in depth in Chapter 4.

Chapter 3: Methodology of Study

This chapter describes the methodology of study applied in this work. First, the method of model generation is explained, which then transitions into the meshing techniques used for these aerial screws. The solution methodology is described in detail. Multiple solution methods are assessed in this study in order to rationalize the use of computationally expensive mathematical models in comparison to less expensive approaches. Finally, a grid convergence study is conducted to ensure the validity of the results.

3.1 Model Generation

Model generation involved parametric sweeping of key design variables such as pitch rates and taper rates in SolidWorks, a computer aided software (CAD) program. Aerial screw CAD models were cleaned from a 3D print ready model to a CFD surface mesh ready model. The majority of aerial screws investigated in this work are of $R_{max} = 1$ ft. Figure 3.1 presents an example of a linearly pitched, linearly tapered, one bladed aerial screw in SolidWorks.

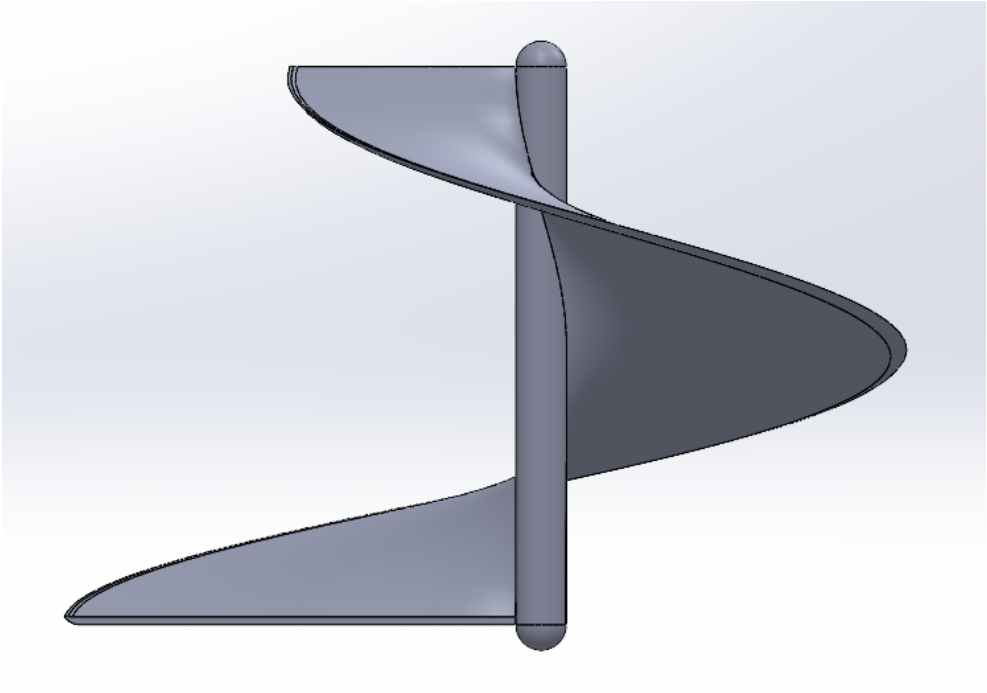

Figure 3.1: SolidWorks CAD Model of Linearly Pitched ($\zeta = 1.2$) and Linearly Tapered ($\eta = 0.5$) Aerial Screw

3.2 Meshing

Due to the naturally complex surface geometry of the aerial screw, surface meshes of all aerial screw rotors are fully unstructured and created in Cadence Pointwise, a meshing software program. Due to varying number of blades, maximum radii, and heights of aerial screws, caused by altering the pitch rate, the cell count of surface meshes vary. The surface mesh for the linearly pitched, linearly tapered, one bladed aerial screw is shown in Figure 3.2.

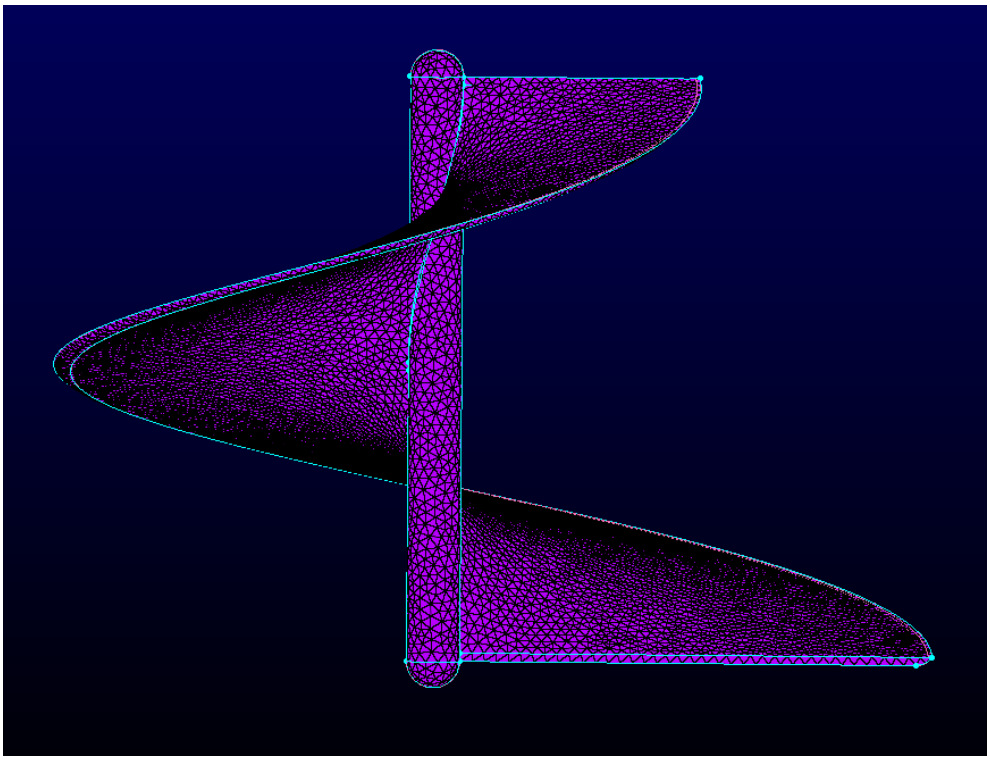

Figure 3.2: Pointwise Unstructured Surface Mesh of Linearly Pitched ($\zeta = 1.2$) and Linearly Tapered ($\eta = 0.5$) Aerial Screw

Table 3.1 shows the variation in cell counts between small and large geometries assessed in this study. The small case represents a small cell count case, a coarsened mesh used for grid convergence study purposes. This case had a linear pitch rate of $\zeta = 1.2$ and a bilinear taper rate of $\eta_1 = 0.8$ and $\eta_2 = 0.0$. The large case represents a large cell count case, a $\zeta = 1.3$ linearly pitched, $\eta = 0.5$ linearly tapered, aerial screw with $N_b = 3$, used for a number of blades study. Table 3.1 provides scope for the various cases investigated in this work, with largely varying mesh sizes and hence computational resources required.

Case Type	Surface Mesh Cells	Nearbody Mesh Cells
Small	16,000	500,000
Large	64,000	1.6 million

Table 3.1: Cell Count Variation of Aerial Screw Cases

3.3 Solution Methodology

3.3.1 CFD Framework

Computational Fluid Dynamics (CFD) is used for the aerodynamic analysis of the flow around these hovering screws using HAMSTR [9], an in-house CFD solution framework. A Delauney algorithm is used for generating cells in the surface and nearbody meshes in Pointwise. HAMSTR employs Hamiltonian paths and strand grids based solution methodology, coupled with overset meshes for farfield computations. DDES (Delayed Detached Eddy Simulation) is the mathematical model used to describe the flow, with SA (Spalart-Allmaras) turbulence closure model, and fully turbulent flow assumptions.

3.3.2 Performance Analysis

In hover, there are three key performance parameters assessed for varying aerial screw designs. These are the thrust coefficient, C_T, power coefficient, C_P, and figure of merit, FM. The rotor area, A, is defined by the screw's maximum radius:

$$A = \pi(R_{max})^2 \tag{3.1}$$

$$C_T = \frac{T}{\rho A(\Omega R_{max})^2} \tag{3.2}$$

$$\lambda_i = \sqrt{\frac{C_T}{2}} \tag{3.3}$$

$$C_P = \frac{P}{\rho A(\Omega R_{max})^3} \tag{3.4}$$

$$FM = \frac{\lambda_i C_T}{C_P} \tag{3.5}$$

To introduce the effect of the climb inflow into the efficiency, the figure of merit is modified as FM^* below where λ_c represents the inflow introduced by the climb velocity:

$$FM^* = \frac{(\lambda_i + \lambda_c)C_T}{C_P} = \frac{(\frac{\lambda_c}{2} + \sqrt{(\frac{\lambda_c}{2})^2 + \frac{C_T}{2}})C_T}{C_P} \tag{3.6}$$

By doing so, FM^* accurately represents the true figure of merit of the rotor in hover when $\lambda_c = 0$, and represents the propulsive efficiency when the climb inflow, λ_c, dominates over the induced inflow in hover.

3.3.3 Delayed Detached Eddy vs Euler Comparison

A one bladed, linearly pitched ($\zeta = 1.2$) and linearly tapered ($\eta = 0.5$) aerial screw case was examined for a potential speed up of the high-fidelity 3D simulations required for the da Vinci Aerial Screw. To rationalize using DDES, this work assessed looking at the Euler mathematical model to describe the flow, hence removing viscous effects and compared the results. Additionally, this study assessed the number of subiterations used for each case. The baseline was chosen to be 20 subiterations, with 10 subiterations investigated for speeding up simulation times. Hence, four case types were developed for this work shown in Table 3.2.

Case	Mathematical Model	No. of Subiterations
A	DDES	10
B	DDES	20
C	Euler	10
D	Euler	20

Table 3.2: Subiterations and Mathematical Model Study

Figure 3.3 displays the thrust coefficient variation with increasing subiterations for both DDES and Euler mathematical model. Figure 3.4 shows the power coefficient variation with increasing subiterations for both DDES and Euler mathematical model and Figure 3.5 shows the figure of merit variation. It is evident that the Euler model under predicts the power requirements of the aerial screw in hover due to no account of viscous effects. Due to this, there is a 6.0% over-prediction in FM between the Euler model and DDES with 20 subiterations. There is enough numerical / artificial viscosity to generate the vortex using Euler, although no mechanism to capture the core or growth. This difference was too significant to use the Euler model and ignore viscous effects for aerial screw CFD simulations.

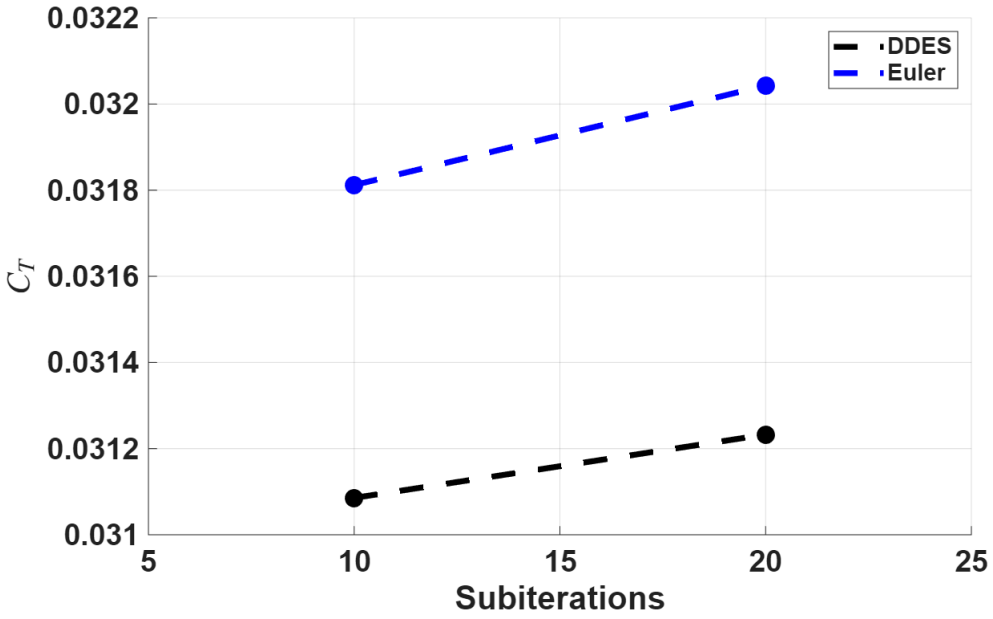

Figure 3.3: Thrust coefficient variation with subiterations for DDES and Euler models

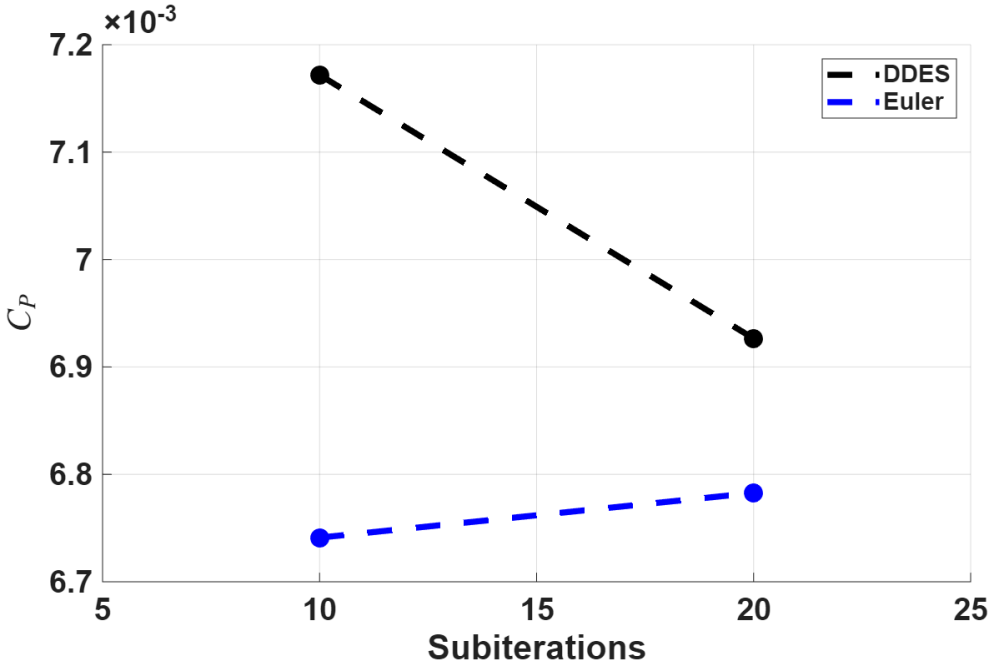

Figure 3.4: Power coefficient variation with subiterations for DDES and Euler models

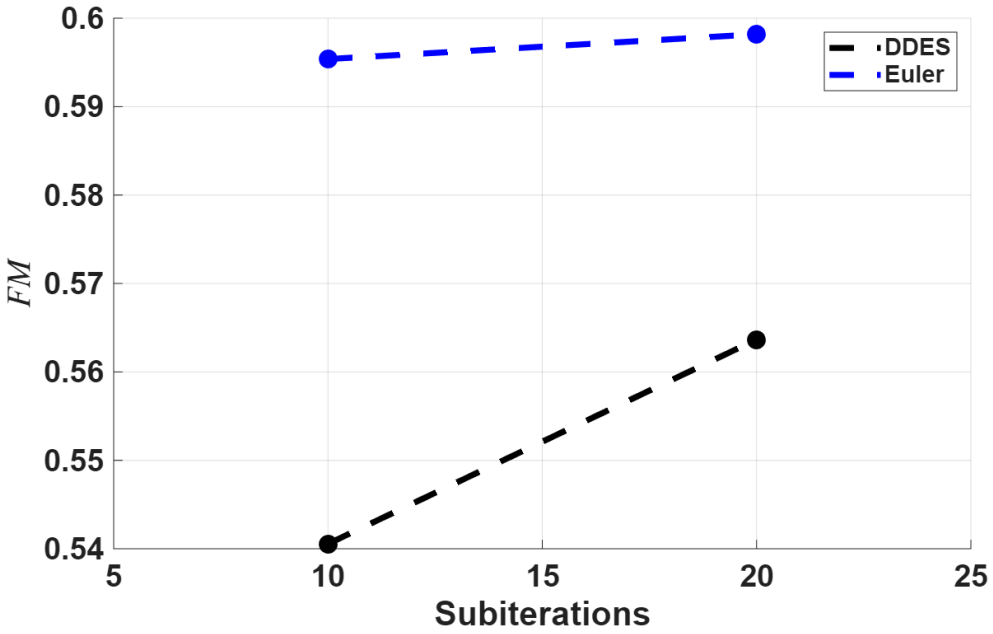

Figure 3.5: Figure of merit variation with subiterations for DDES and Euler models

With the use of the delayed detached eddy simulation (DDES) model rationalized, the use of 20 subiterations is justified with Figures 3.6, 3.7, and 3.8. The L2 norm of residual vs iterations in the nearbody is an acceptable drop of 1.5 orders of magnitude due to unsteadiness in the flow. Because the magnitude of unsteadiness decreases further from the blade's surface, there is 3.5 order of magnitude drop in the L2 norm of residual in the nested mesh. This further increases to approximately a 6 order drop in the farfield mesh. With appropriate drops in the residual values and steady, periodic force and moment behaviors in converged solutions, 20 subiterations was determined reasonable for the DDES mathematical model. Each aerial screw was run to at least 12 revolutions, with most cases reaching 16 revolutions and decrease timestep sizes to ensure convergence.

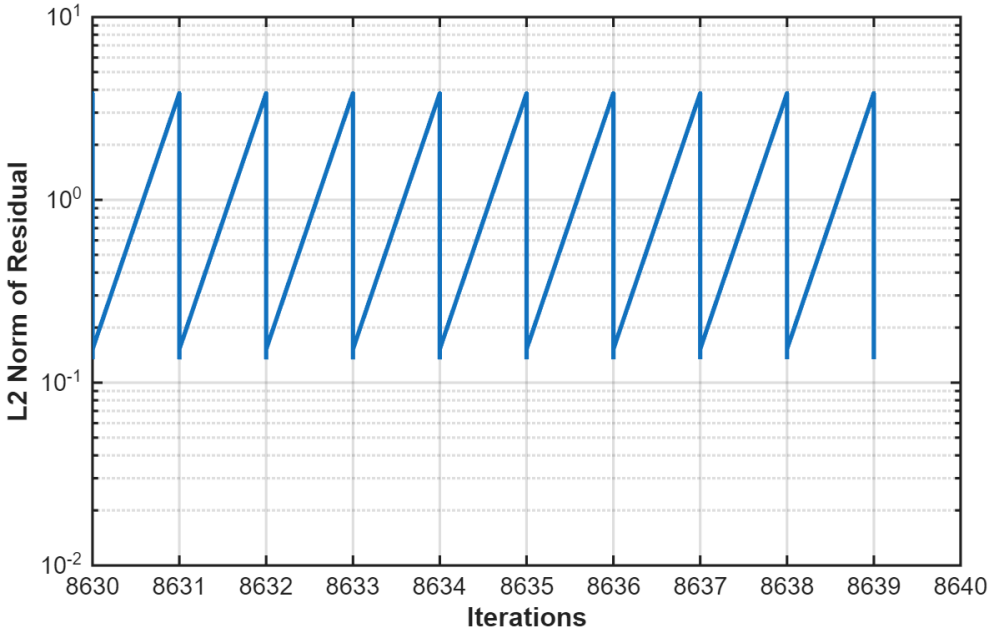

Figure 3.6: L2 Norm of Residual vs Iteration for Nearbody Mesh

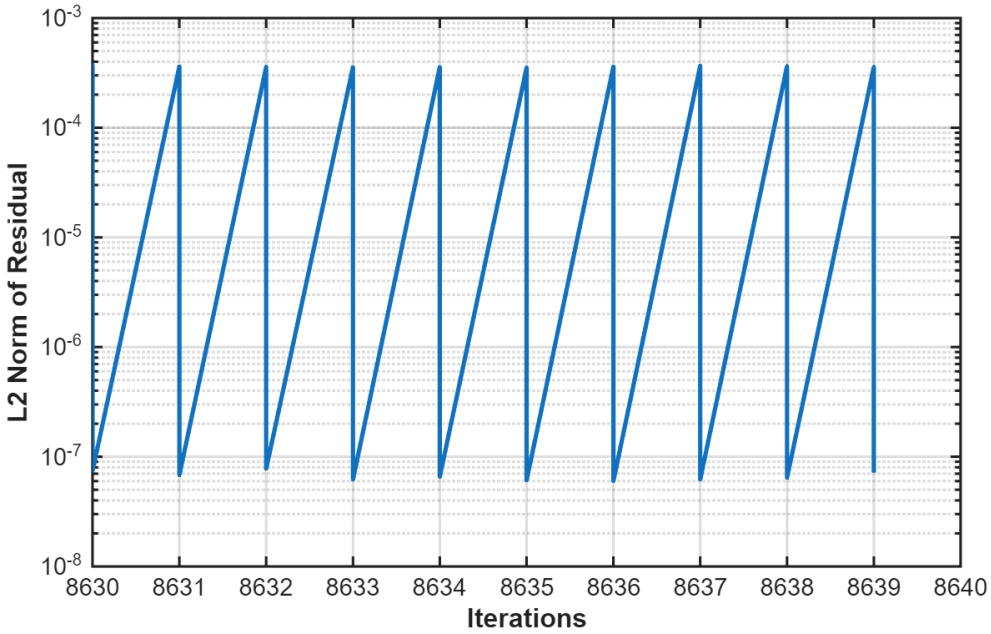

Figure 3.7: L2 Norm of Residual vs Iteration for Nested Mesh

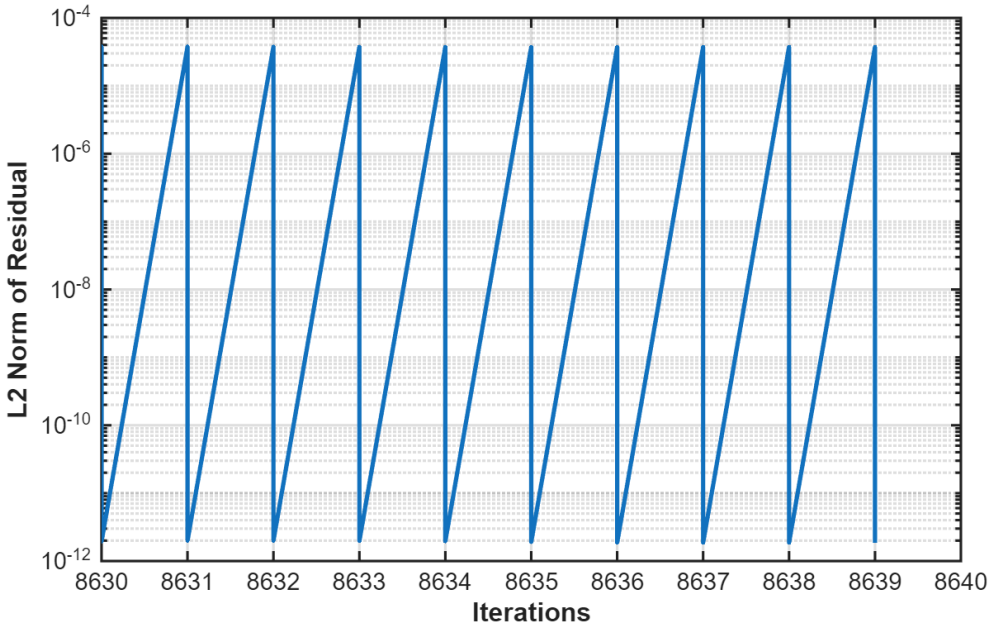

Figure 3.8: L2 Norm of Residual vs Iteration for Farfield Mesh

3.3.4 Grid Convergence Study

A grid convergence study was conducted to confirm the validity of the resolution of the CFD simulation results. The case, as mentioned above, a one bladed, $R_{max} = 1$ ft aerial screw with a linear pitch rate of $\zeta = 1.2$ and a bilinear taper rate of $\eta_1 = 0.8$ and $\eta_2 = 0.0$ was used for this study. The wall spacing (Δs) is fixed constant throughout all cases, corresponding to $y^+ = 1$ to ensure resolution and appropriate capturing of the boundary layer. All meshes have a constant 30 layers grown out from the surface mesh to the outer boundaries of the nearbody. The nearbody mesh boundaries are held constant across the cases as well. Table 3.3 shows the surface and nearbody mesh cell counts for the 4 mesh refinements used for the study. The coarsest mesh corresponds to Case 1 with 16,000 surface cells and 500,000 nearbody cells. Second coarsest case is labeled Case 2, with 29,000 surface mesh cells and 950,000 cells. The refined Case 3 is made up of 38,000 surface cells and 1.2 million nearbody cells. The most refined Case 4 consists

of 50,000 surface mesh cells with 1.6 million cells in the nearbody.

Figure 3.9 shows the variation in C_T with a refining nearbody mesh. Figure 3.10 shows the variation in C_P with a refining nearbody mesh and Figure 3.11 shows the variation in FM. Case 1, the coarsest mesh, is found to give a significantly higher thrust coefficient of $C_T = 0.044$ while the average of the thrust coefficients found in all other meshes is $C_{T_{avg}} = 0.035$ with a 1.1% maximum difference between Cases 2, 3 and 4. Similarly, Case 1 has a higher power coefficient compared to Cases 2, 3, 4 at $C_P = 0.009$. Cases 2, 3, and 4 had an average $C_{T_{avg}} = 0.008$ with a 0.6% maximum difference. This results in the figure of merit being heavily over-predicted as shown in Figure 3.11. Artificially high pressure differentials are produced on the surface of the aerial screw blade as cell areas increase and pressure gradients become unresolved. With the results of this study, surface meshes are kept above 32,000 cells and nearbody meshes used are kept above 1 million cells (as denoted by the blue line in all figures pertaining to this subsection) with a minimum of 30 layers to ensure proper resolution of the physics, aerodynamics, and performance.

Case	Surface Mesh Cells	Nearbody Mesh Cells
1	16,000	500,000
2	29,000	950,000
3	38,000	1.2 million
4	50,000	1.6 million

Table 3.3: Grid Convergence Study

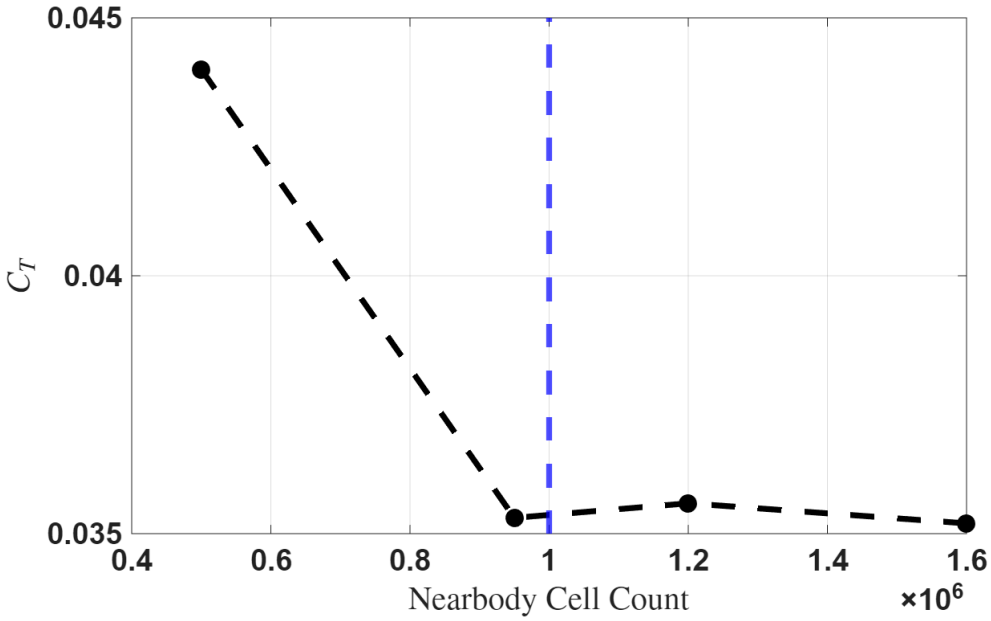

Figure 3.9: Thrust coefficient variation with nearbody mesh cell count in hover for best bilinearly tapered aerial screw

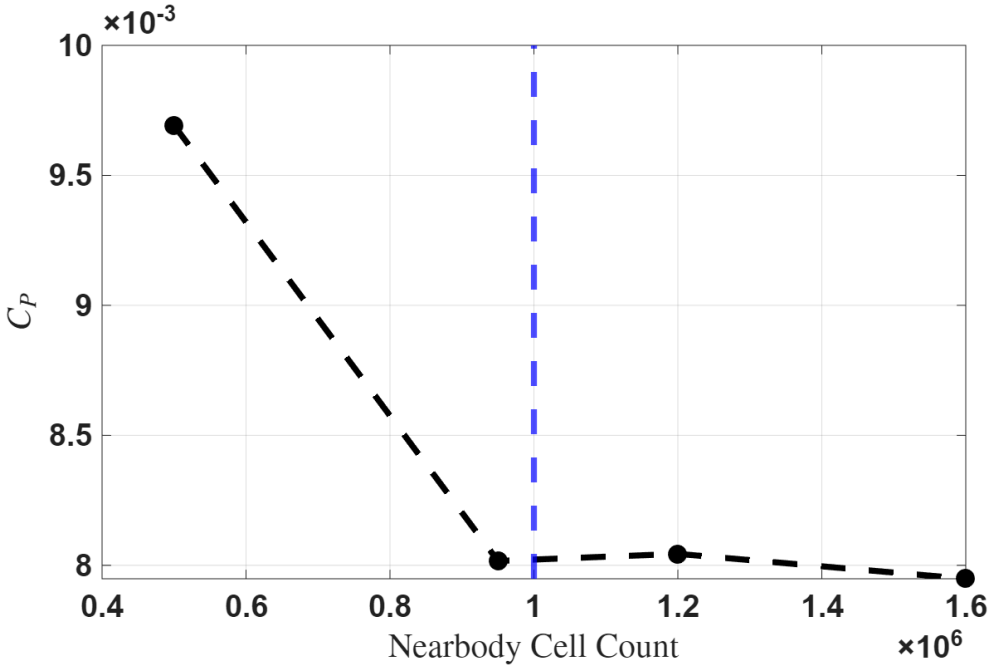

Figure 3.10: Power coefficient variation with nearbody mesh cell count in hover for best bilinearly tapered aerial screw

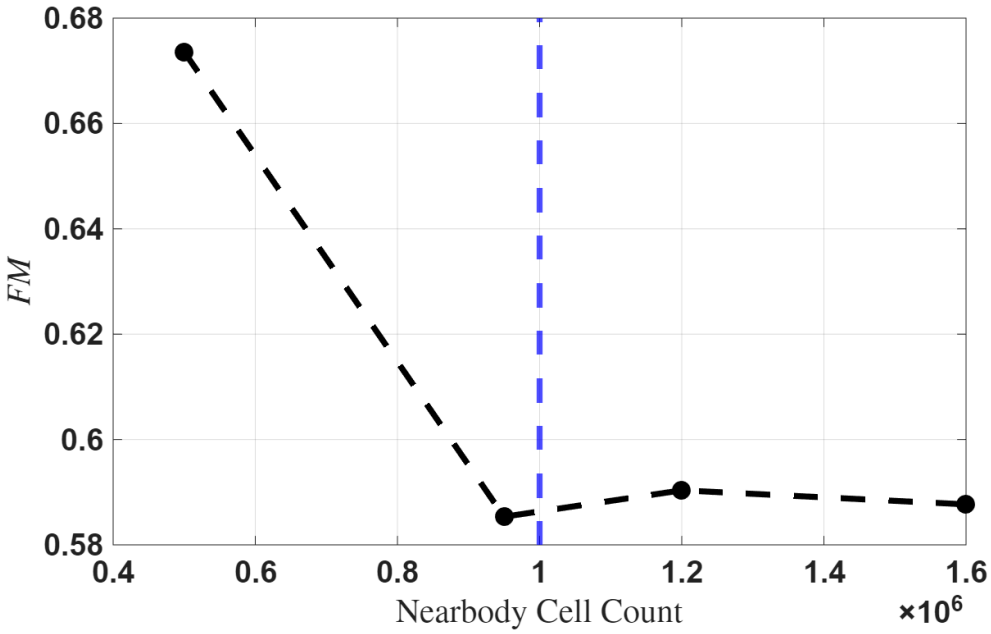

Figure 3.11: Figure of merit variation with nearbody mesh cell count in hover for best bilinearly tapered aerial screw

3.4 Chapter Summary

This chapter dives into the methodology of study applied to this collection of works. The model generation and meshing techniques are discussed first. SolidWorks is used in generating CAD models to prepare the model for meshing. Meshing is done in Cadence Pointwise. The surface and nearbody meshes are fully unstructured. A $y^+ = 1$ is used in the nearbody mesh for all models in this study. All nearbody meshes have at least 30 layers. A grid convergence study determined that all surface meshes must contain at least 32,000 cells with over 1 million cells in the nearbody.

Two various mathematical models, Delayed Detached Eddy Simulation (DDES) and Euler equation, are assessed to determine the potential for speed up of the high-fidelity 3D simulations. It was found that viscous effects are highly important to appropriately capture the correct physics

pertaining to aerial screw flight. This resulted in DDES chosen as the mathematical model with 20 subiterations showing sufficient convergence of the L2 norm of residual.

Chapter 4: Aerodynamics and Performance Impacts

This chapter dives into the effect of varying defining aerial screw parameters on the aerodynamics of the rotors and the impact on performance metrics. Linear pitch and linear taper varying geometries are investigated in hover, axial climb, and off-axis climb. Bilinear pitch and bilinear taper geometries are investigated solely in hover. The combination of the best performing bilinear pitch and bilinear taper geometry is assessed in hover, axial climb, and off-axis climb. A comparison of the best linear pitch - linear taper, bilinear pitch - linear taper, linear pitch - bilinear taper , and bilinear pitch - bilinear taper geometries is conducted at the end of the chapter.

The setup of the axial flow conditions is shown in further detail in Figure 4.1. The da Vinci vortex is visualized along with a developed hub vortex. The total additional inflow is maintained at $\lambda_c = 0.08$ corresponding to the highest axial climb speed assessed in this study. An intermediate slow climb speed of $\lambda_c = 0.04$ is assessed as well. The streamlines above the leading edge plane show the flow aligning in the axial direction.

Additional to axial climb, one off-axis climb condition is investigated in this work, corresponding to a climb inflow of $\lambda_c = 0.08$, with a 5 degree off-axis tilt from axial flow. The setup of the flow conditions is shown in further detail in Figure 4.2. Additionally, the da Vinci vortex, described in the following section, is visualized along with a developed hub vortex. The force and moment coefficients corresponding to off-axis flight are compared among varying linear pitch and linear

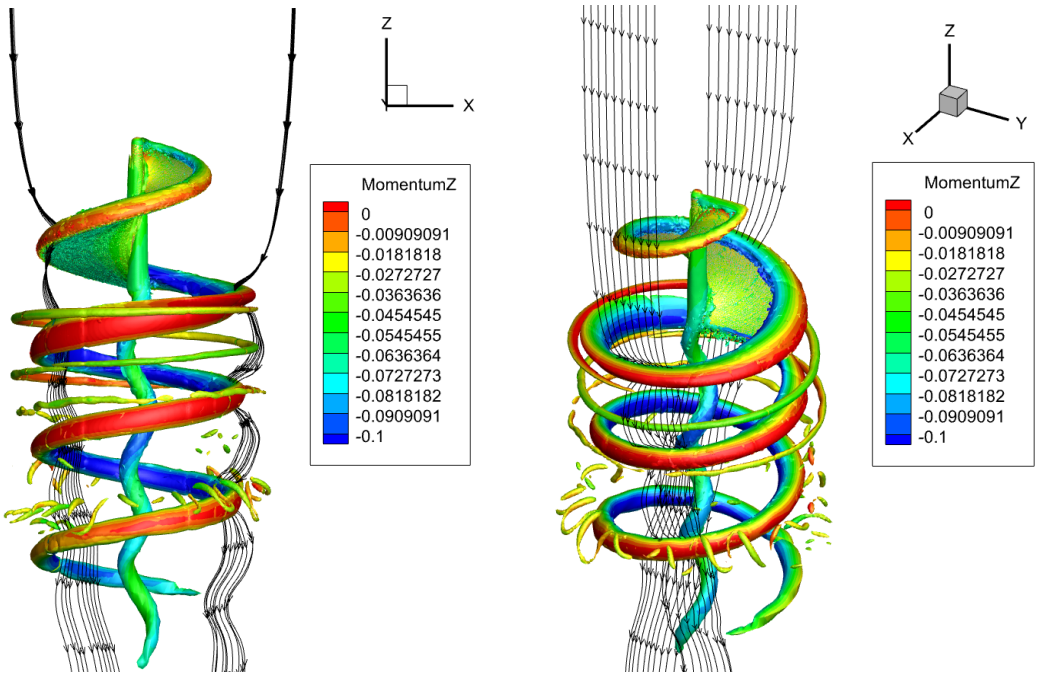

Figure 4.1: Axial flow iso-surfaces of vorticity Q-criterion ($\zeta = 1.4$ linear pitch case)

taper rate cases. All moments are taken at the center of the hub, in-plane with the trailing edge of all aerial screw rotors. The results are compared to that of a one bladed bilinearly pitched and bilinearly tapered aerial screw, found to be the most efficient design in hover at $FM = 0.65$ when $M_{tip} = 0.37$.

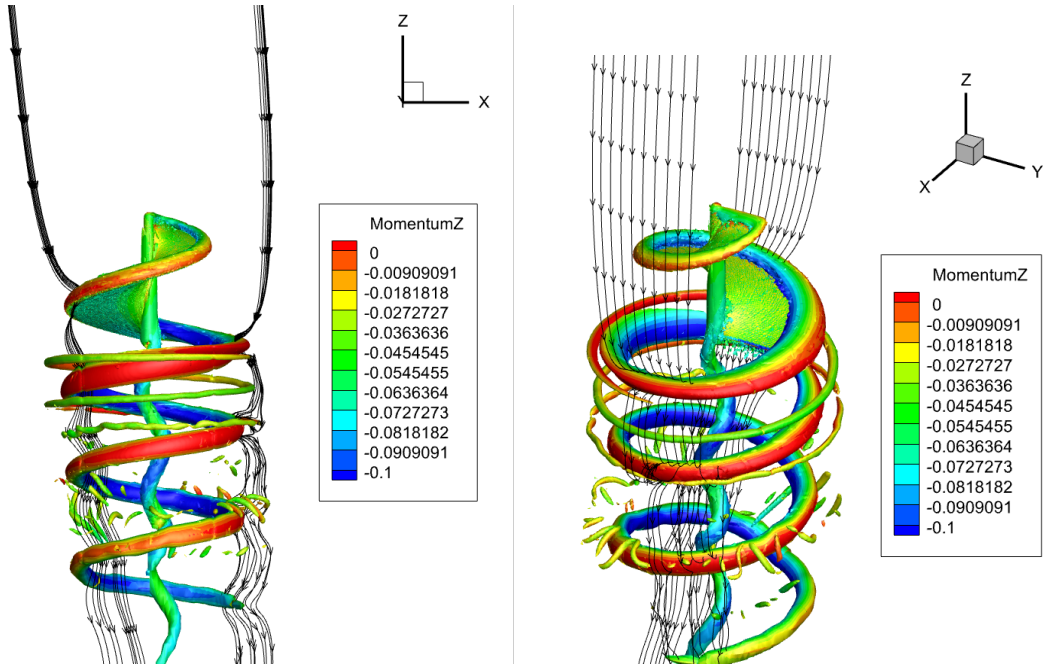

Figure 4.2: Off-axis iso-surfaces of vorticity Q-criterion ($\zeta = 1.4$) (Left: Side view, Right: Isometric view)

For comparison, two notional conventional rotors are designed, one with 2 blades and the other with 4 blades. Both rotors have rectangular planforms, with a uniform twist rate of 20° from root to tip, and Clark-Y airfoil throughout the cross section. The choice of the airfoil is made based on the operating Reynolds number. The collective of the blade is adjusted to achieve an optimal figure of merit. The solidity of each of the rotors is maintained at $\sigma = 0.16$.

Since the aerial screws are of extremely high solidity, conventional rotors can not achieve the same thrust at same size and tip speed. Two versions of the conventional rotors are investigated, namely, one with same rotor size but trimmed with RPM and the other with same tip speed but of a larger size.

It is important to note that for the results shown below, there is no experimental validation. This is purely an extensive computational study into the aerodynamics, performance, and acoustics of aerial screws.

4.1 Effect of Radius (R_{max})

To investigate the effect of screw size ($R_{\max}$) on the performance, five different screws are modeled with a uniform pitch rate ($\zeta = 1$) and uniform taper rate ($\eta = 0.5$), viz., $R_{\max} \in \{0.25 \text{ ft}, 0.5 \text{ ft}, 1 \text{ ft}, 5 \text{ ft}, 10 \text{ ft}\}$. The RPM of the screws is chosen to attain a tip Mach number of 0.25 at the tip of the trailing edge of the blade. Due to the variation in size, the tip Reynolds number varies from 0.5×10^6 to 17×10^6.

Figure 4.3 shows the variation of figure of merit across for different screw sizes. It is observed that as the screw size increases, the figure of merit of the screw increases with a larger variation at lower sizes and smaller variations at larger sizes. The da Vinci vortex development is similar across all the sizes and shows similar pressure differences ΔC_P across the blade surface.

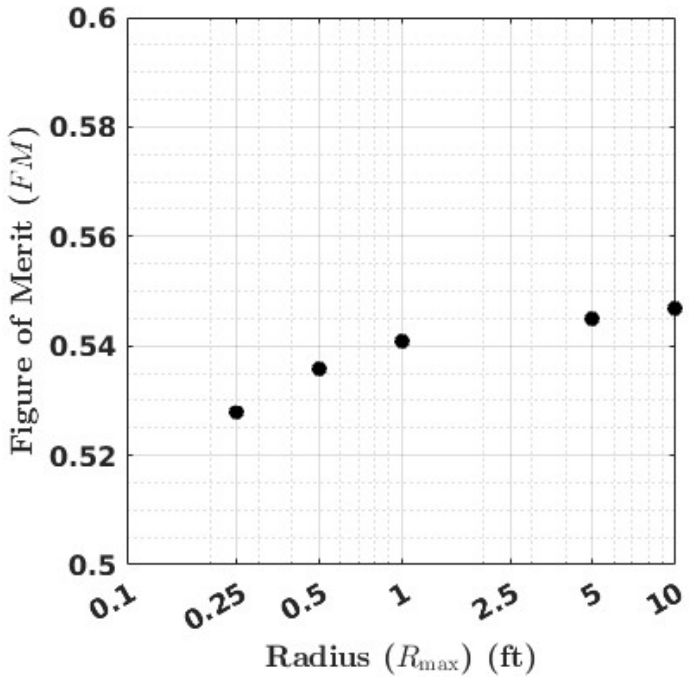

Figure 4.3: Variation of Figure of Merit for Screws of different sizes

Minor variations in the figure of merit can be attributed to the viscous effects contributing

to higher power requirements and resulting in lower efficiency as the radius decreases (and the Reynolds number decreases).

4.2 Number of Blades (N_b)

This section investigates the effects of varying the number of blades on the aerodynamics and performance of aerial screws. The screws considered in this study consist of a uniform taper rate $\eta = 0.5$, uniform pitch rate $\zeta = 1.3$ and radius of 1 ft. Figure 4.4 shows the variation of figure of merit for these screws, indicating a continuous and significant decrease in the performance with increasing number of blades. This is consistent with the conventional low solidity helicopter rotors, and is due to the interactional aerodynamics between multiple blades increasing the losses.

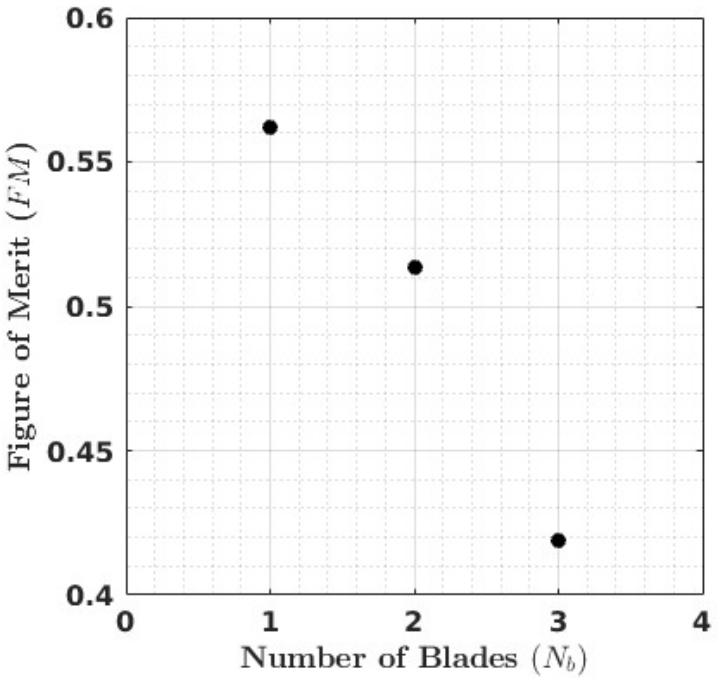

Figure 4.4: Variation of figure of merit with number of blades

Figure 4.5 shows the vorticity iso-contours for these screws, indicating the reduction in

da Vinci vortex strength with increasing number of blades. Furthermore, it is observed that the vortex moves inboard with increasing number of blade, due to the interactions between other helical vortical structures.

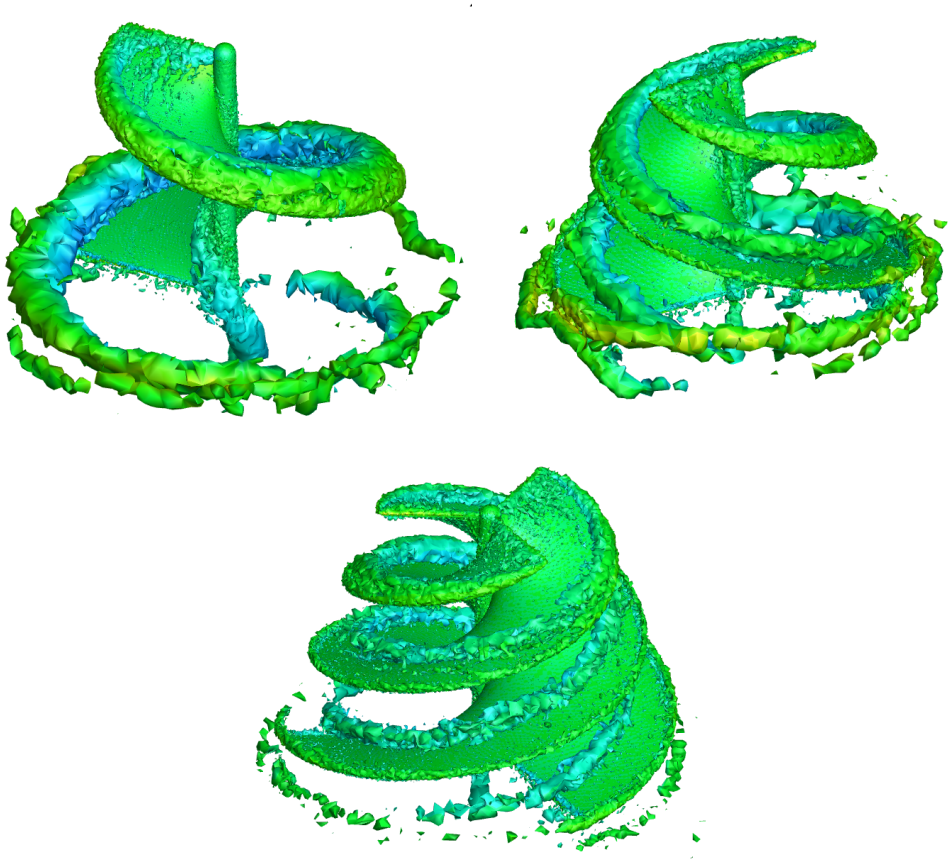

Figure 4.5: Vorticity contours showing the decreased strength of daVinci vortex with increasing number of blades in the screw ($N_b = 1$ - top left, $N_b = 2$ - top right, $N_b = 3$ - bottom middle)

While the performance is worsened with increasing number of blades, all these screws have the same taper and pitch characteristics. While these values correspond to a better performance for a single bladed screw, it is not necessary that the same geometric variation is suitable for multiple blades. Hence, a combination of the design variable variations such as increase in pitch with increasing umber of blades may improve the performance substantially.

4.3 Pitch Rate (ζ)

This section investigates the effects of linear and bilinear variations of pitch rate on the aerodynamics and performance of aerial screws with constant taper rates.

4.3.1 Linear Pitch Rate

The effect of a varying linear pitch rate is investigated for aerial screws predominantly in hover, with preliminary investigations in axial climb and off-axis climb states.

4.3.1.1 Hover

To understand the effect of pitch rate in hover, several screws with a constant taper rate $\eta = 0.5$ and $R_{\max} = 1$ ft are studied, with each screw having a different uniform pitch rate. The tip Mach number at the trailing edge is maintained at 0.25 for all these screw designs, which corresponds to a tip Reynolds number of 1.7×10^6.

Figure 4.6 shows the variation of figure of merit for these screws with the pitch rate. It can be seen that the performance of the screw improves initially when the pitch rate ζ increases from 1 to 1.2, and then decreases continuously with increasing pitch.

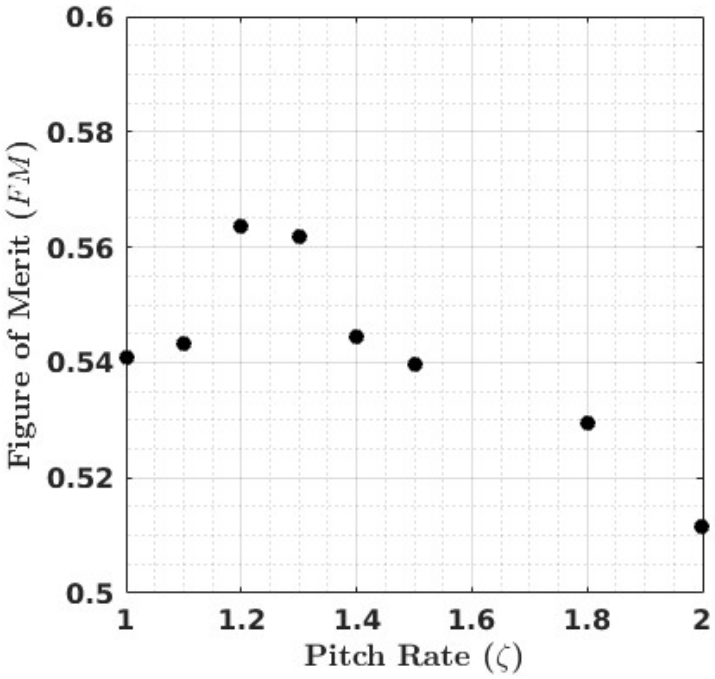

Figure 4.6: Variation of figure of merit of aerial screws with varying pitch rate

The aerodynamic behavior of the high pitched screw results in a large shed vorticity at the leading edge due to flow separation, resulting in a stronger tip vortex formation. Figure 4.7 shows the pressure difference across the blade surface for three different screws with low ($\zeta = 1$), moderate ($\zeta = 1.2$) and aggressive ($\zeta = 1.5$) pitch rates. It can be seen that the leading edge shed vorticity and the corresponding pressure difference can be seen as continuously increasing with increasing pitch rate.

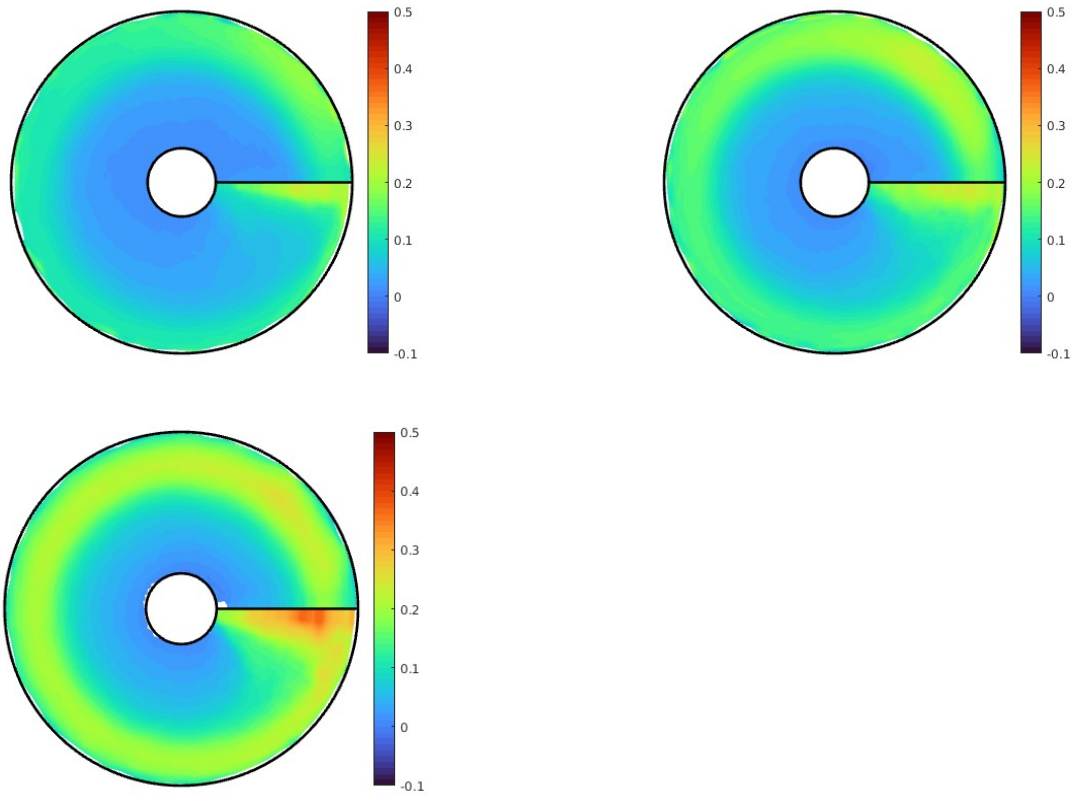

Figure 4.7: ΔC_P contours for aerial screws with different pitch rates: Top left: $\zeta = 1$, Top right $\zeta = 1.2$ and Bottom left: $\zeta = 1.5$

However, the normal force (ΔC_P) due to the vortex contributes to both thrust and torque. Figures 4.8, 4.9 show the axial and torque-wise components of the pressure loads projected onto $r' - \theta$ plane. As the pitch rate increases from 1 to 1.2, the axial contribution of the normal force increases significantly. This is due to a significant increase in ΔC_P accompanied by a moderate decrease in axial component, resulting in effectively larger increase in the resultant axial loads. As the pitch rate is further increased aggressively to 1.5, the axial projection component decreases significantly compared to the increase in ΔC_P. As a resultant, the axial contribution of the normal force increases slightly.

The change in axial loads corresponding to the variation from low to moderate pitch rate is

observed to be $\sim 36\%$, while that corresponding to moderate to aggressive pitch rate is $\sim 15\%$. The ideal power change corresponding to this increase in axial load is given by the percentage change of $C_T^{3/2}$. This amounts for approximately 58% for the low to moderate pitch rate and 23% for the moderate to aggressive pitch rate variation.

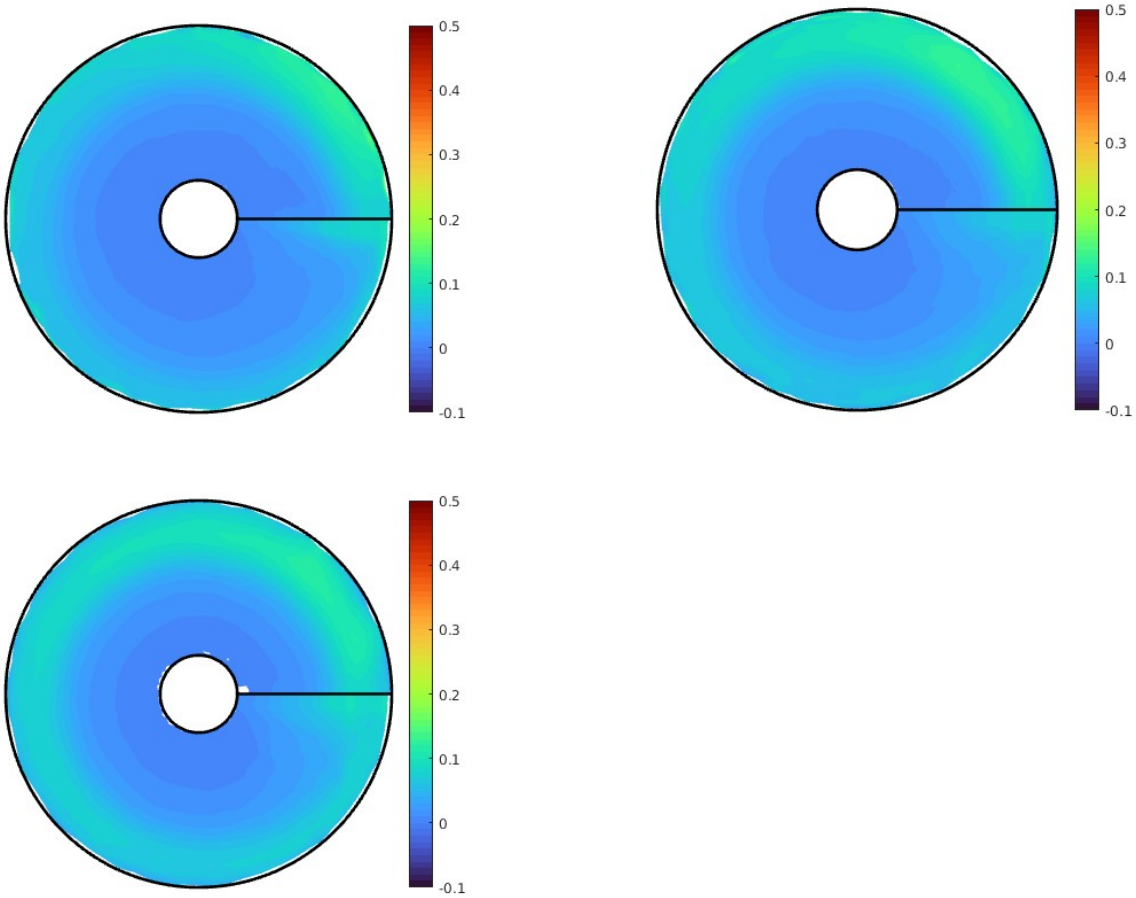

Figure 4.8: Axial component of ΔC_P contours for aerial screws with different pitch rates: Top left: $\zeta = 1$, Top right $\zeta = 1.2$ and Bottom left: $\zeta = 1.5$

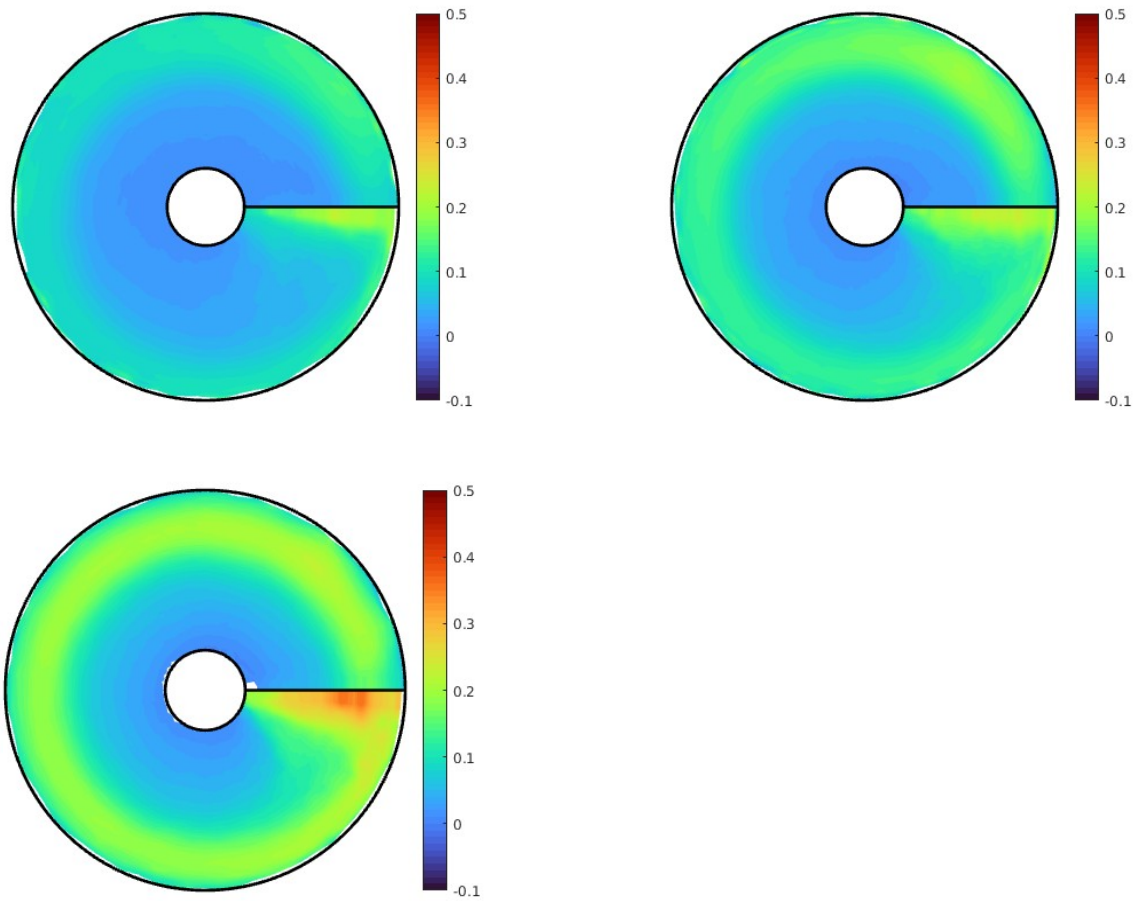

Figure 4.9: Torque-wise component of ΔC_P contours for aerial screws with different pitch rates: Top left: $\zeta = 1$, Top right $\zeta = 1.2$ and Bottom left: $\zeta = 1.5$

When the torque-wise components for these scenarios are compared, the torque contribution increases moderately from low to moderate pitch variation, but increases significantly for the high pitch screw. The torque-wise load, i.e., actual power variation is observed to be $\sim 52\%$ for the low to moderate pitch variation. This is less than the ideal power variation computed, indicating that the increase in pitch rate to moderate values has better power characteristics than low pitch rate screw. On the other hand, the power is observed to increase by $\sim 30\%$ for the moderate to aggressive pitch variation, which is higher than the ideal power variation, indicating a poor performance characteristic of the aggressively pitched screw.

A comparison of the most efficient design ($\zeta = 1.2$) and the most aggressively pitched design ($\zeta = 2.0$) is discussed to assess the effects of increasing the pitch rate of the rotor.

Figure 4.10 shows the vorticity iso-contour of the $\zeta = 1.2$ linearly pitched design. The visualization depicts an attached da Vinci vortex along the blade which remains relatively undisturbed after leaving the trailing edge of the rotor.

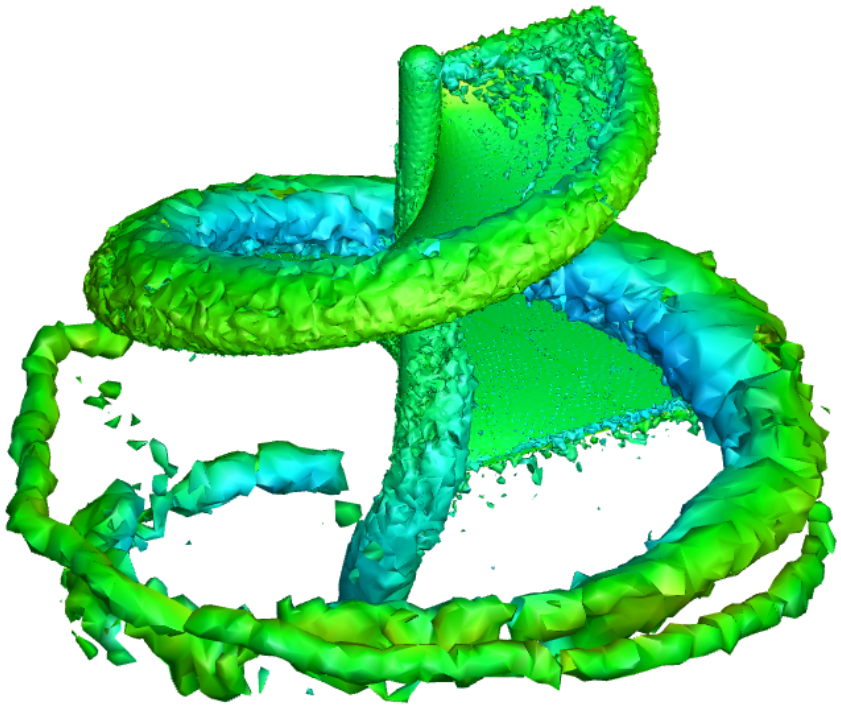

Figure 4.10: Vorticity contour of the $\zeta = 1.2$ linearly pitched design

Figure 4.11 shows the vorticity iso-contour of the $\zeta = 2.0$ linearly pitched design. A stronger da Vinci vortex is developed, attributed by the aggressive pitch rate. However, as pitch rate increases, the normal vector orientation of the blade points further torque-wise. This results

in more power being required to achieve the same amount of thrust, decreasing the figure of merit.

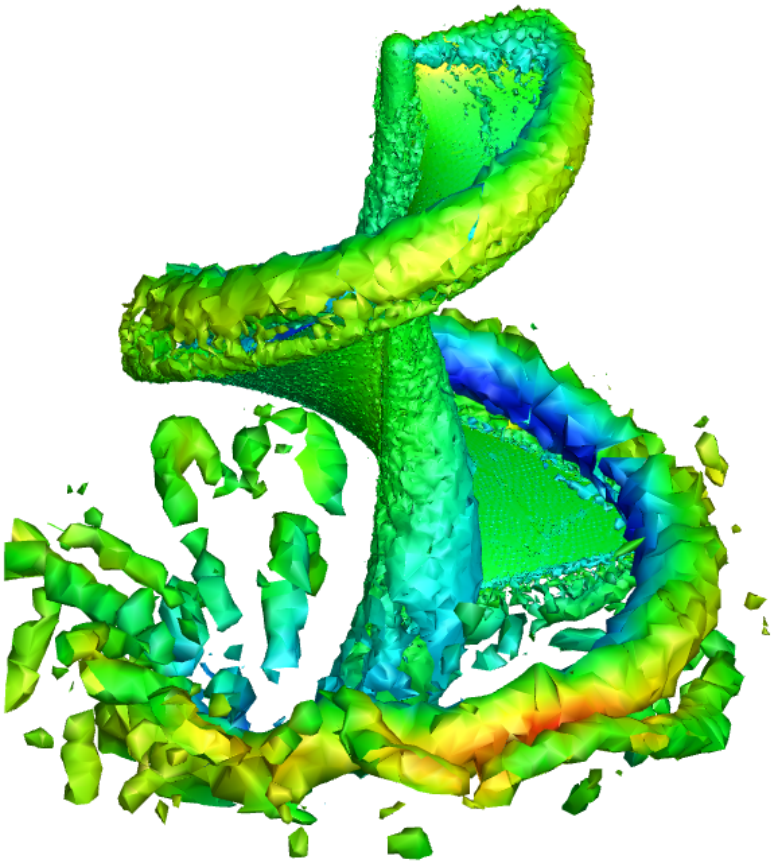

Figure 4.11: Vorticity contour of the $\zeta = 2.0$ linearly pitched design

Pressure distributions along four azimuthal locations along the blade ($\psi = 0°$ being defined at the leading edge) were extracted to determine the primary locations of lift along the rotor.

Figure 4.12 shows the pressure distribution of the $\zeta = 1.2$ linearly pitched design.

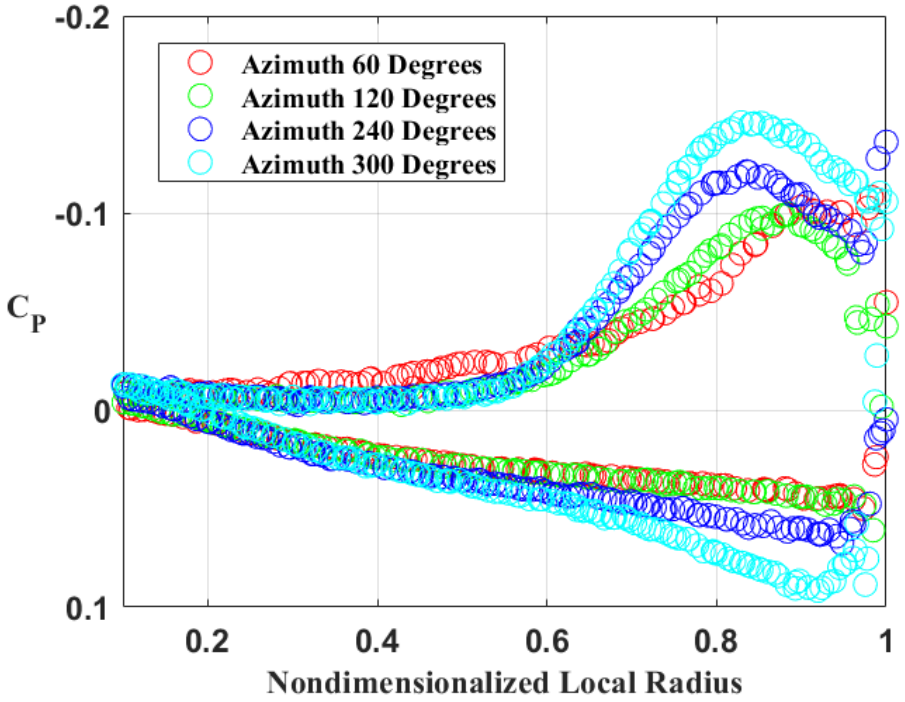

Figure 4.12: Pressure distribution of the $\zeta = 1.2$ linear pitch design

From this figure, it is seen that the majority of the lift generated by the screw is near the tip of the blade, increasing in strength as the angle of azimuth increases. This lift can be attributed to the da Vinci vortex which was visualized in Figure 4.10. As the vortex advances down the blade, its strength increases and more lift is being generated.

Figure 4.13 shows the pressure distribution of the $\zeta = 2.0$ linearly pitched design.

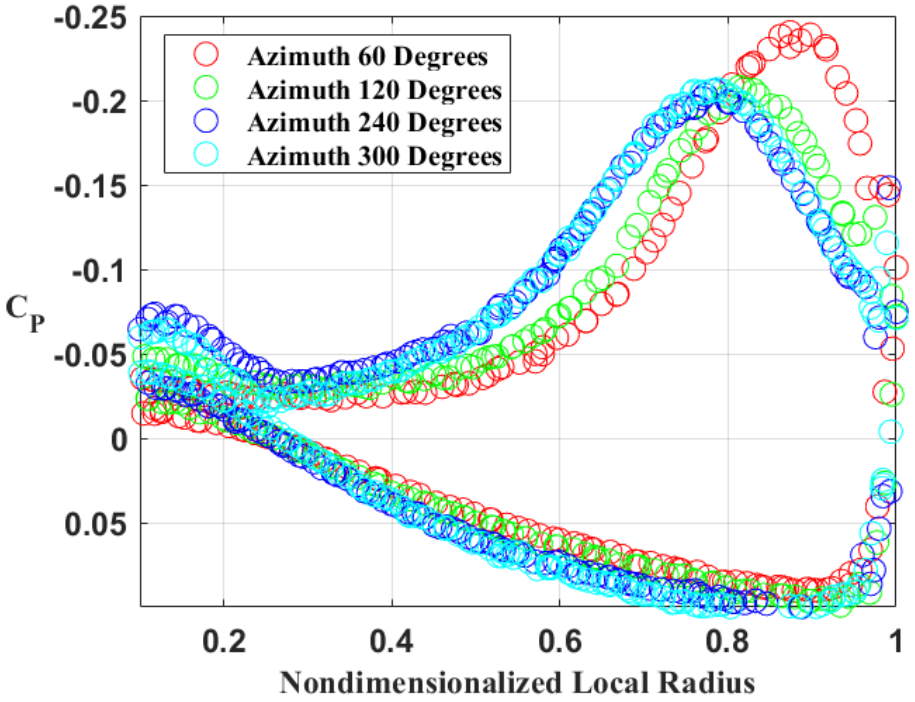

Figure 4.13: Pressure distribution of the $\zeta = 2.0$ linear pitch design

The pressure distributions change significantly between the $\zeta = 1.2$ and $\zeta = 2.0$ designs. The pressure differences between the top and bottom surface of the blade increase for all azimuthal angles for the $\zeta = 2.0$ design. Along with this, the rotor's vortex appears to be strongest near $\psi = 60°$ for the $\zeta = 2.0$ design. This differs from the $\zeta = 1.2$ design where the vortex continued to grow in strength as angle of azimuth increased. This is contributed to the vortex detaching from the blade surface as it advances, building on the concept of an optimal pitch rate having an upper limit. The increase in pressure differential towards the tip of the blade is visible in Figure 4.11 as the vortex is visibly stronger than that of the $\zeta = 1.2$ design.

Despite a stronger vortex, the natural shape of an aggressively pitched design results in a significantly larger power requirement. An optimal pitch rate value for a linearly pitched design is found by achieving a balance of vortex strength and a minimal torque component of the blade's

surface normal vectors.

4.3.1.2 Axial Climb

To understand the effect of pitch rate in axial climb, several one bladed screws with a constant taper rate $\eta = 0.5$ and $R_{\max} = 1$ ft are studied, with each screw having a different linear pitch rate. The tip Mach number at the trailing edge is maintained at 0.37 with a tip Reynolds number of 2.63×10^6 for all screw designs. This deviates from the hover section where all aerial screws maintained a tip Mach number of $M_{tip} = 0.25$. Figure 4.14 shows the efficiency of aerial screws with different linear pitch rates in hover. The figure of merit rises from low pitch rate values up to the optimal linear pitch rate of $\zeta = 1.2$, then continues to decrease as the pitch rate increases further. The $\zeta = 1.2$ case is again optimal, with a figure of merit nearing 0.57.

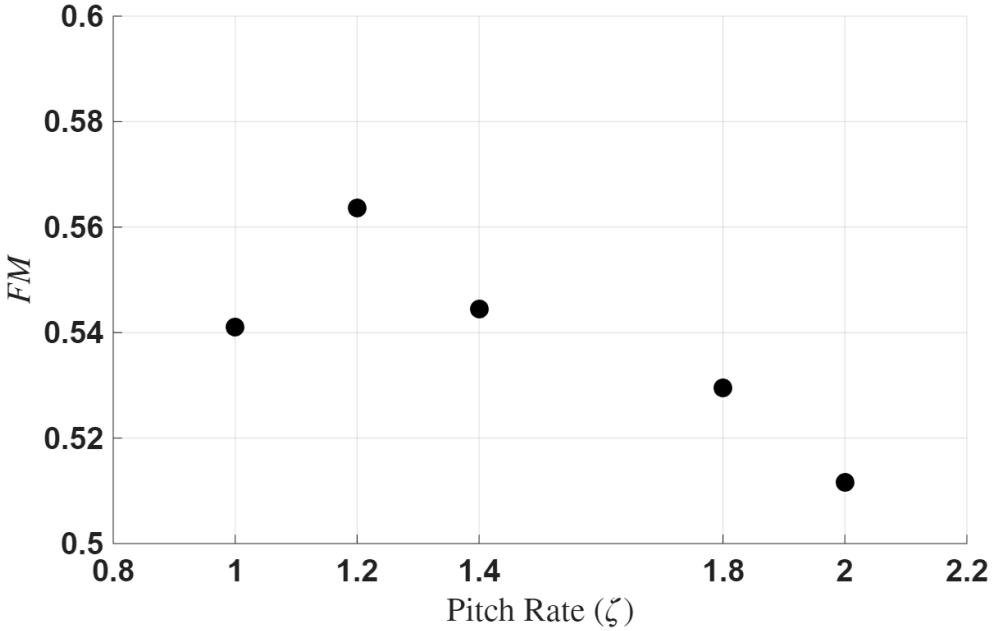

Figure 4.14: Variation of figure of merit of aerial screws with varying pitch rate in hover

The optimal linear pitch rate case of $\zeta = 1.2$ is used to assess the effect of varying the climb speed. Figures 4.15, 4.16, and 4.17 show the thrust and power coefficients as well as FM^* as a

function of the axial climb speed. The thrust coefficient drops linearly from hover ($\lambda_c = 0.0$) to a climb speed corresponding to $\lambda_c = 0.20$. The effective angle of attack seen by the leading edge of the aerial screw decreases as the climb inflow increases. At $\lambda_c = 0.20$, the thrust coefficient drops to $C_T = 0.0$ due to this phenomenon. Similarly, the power coefficient drops with an increase in climb speed as well, ranging from $C_P = 0.007$ in hover to $C_P = 1.7e-4$ at the maximum $\lambda_c = 0.20$. Additionally, FM^* is plotted against the varying climb inflow as well. It is seen that in hover, FM^* matches that from Figure 4.14. FM^* drops nonlinearly as the climb inflow increases, dropping significantly as the λ_c nears 0.20. From this distribution, it is seen that the optimal linearly pitched design in hover decreases in performance as the climb inflow increases. This is caused by the shallow angle of attack of the leading edge for the $\zeta = 1.2$ pitch case.

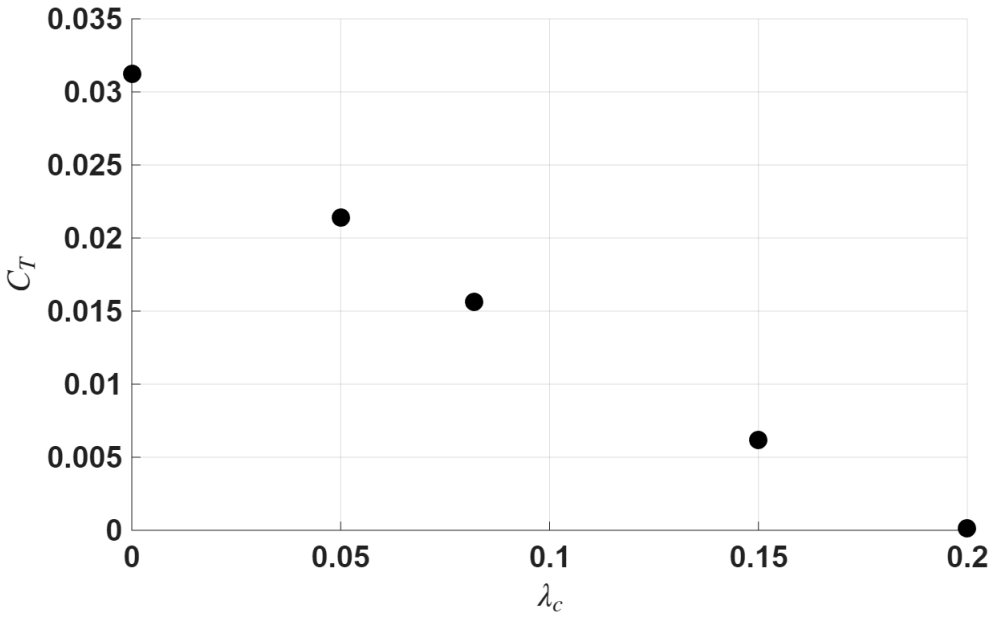

Figure 4.15: C_T of optimal linear pitch screw ($\zeta = 1.2$) for varying axial climb speeds

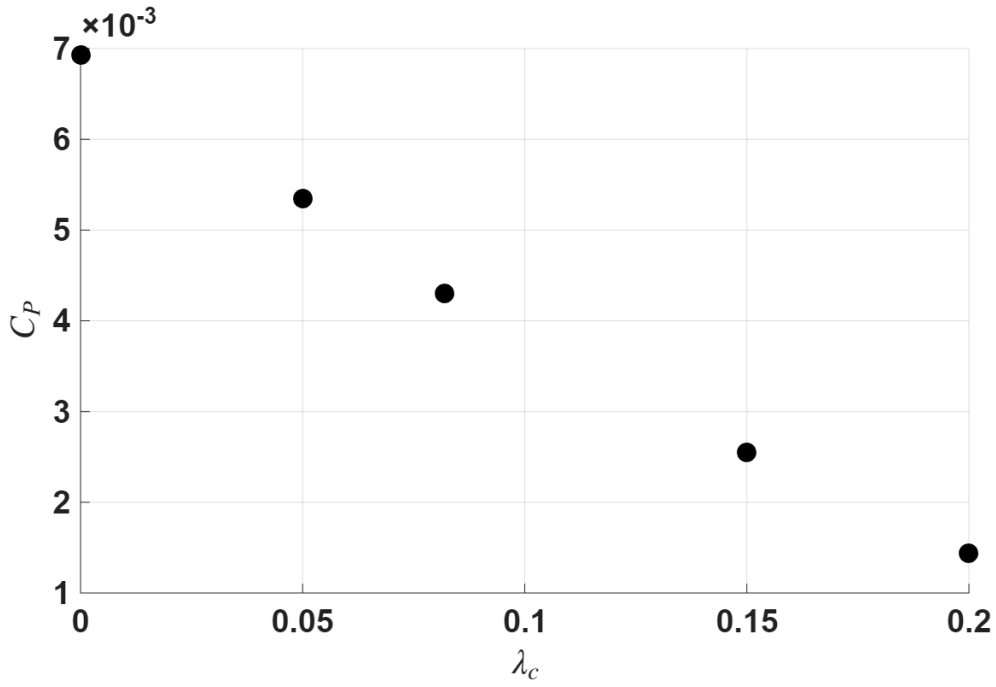

Figure 4.16: C_P of optimal linear pitch screw ($\zeta = 1.2$) for varying axial climb speeds

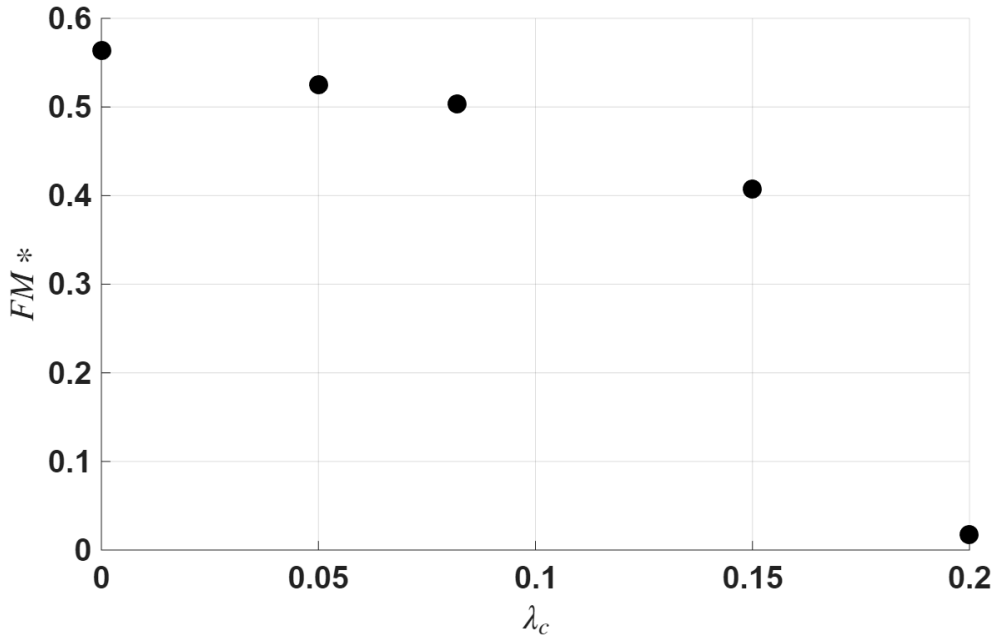

Figure 4.17: FM^* of optimal linear pitch screw ($\zeta = 1.2$) for varying axial climb speeds

The various linearly pitched cases as shown from Figure 4.14 are investigated at two different climb inflows ($\lambda_c = 0.04, \lambda_c = 0.08$) to assess the effect of the pitch rate on the

efficiency of the rotors as λ_c increases in Figure 4.18.

The data points in black show the same as Figure 4.14, the figure of merit of each linearly pitched aerial screw in hover. The blue data points represent the same designs in a slow axial climb, corresponding to $\lambda_c = 0.04$. The red data points show the behavior in a faster axial climb, corresponding to $\lambda_c = 0.08$.

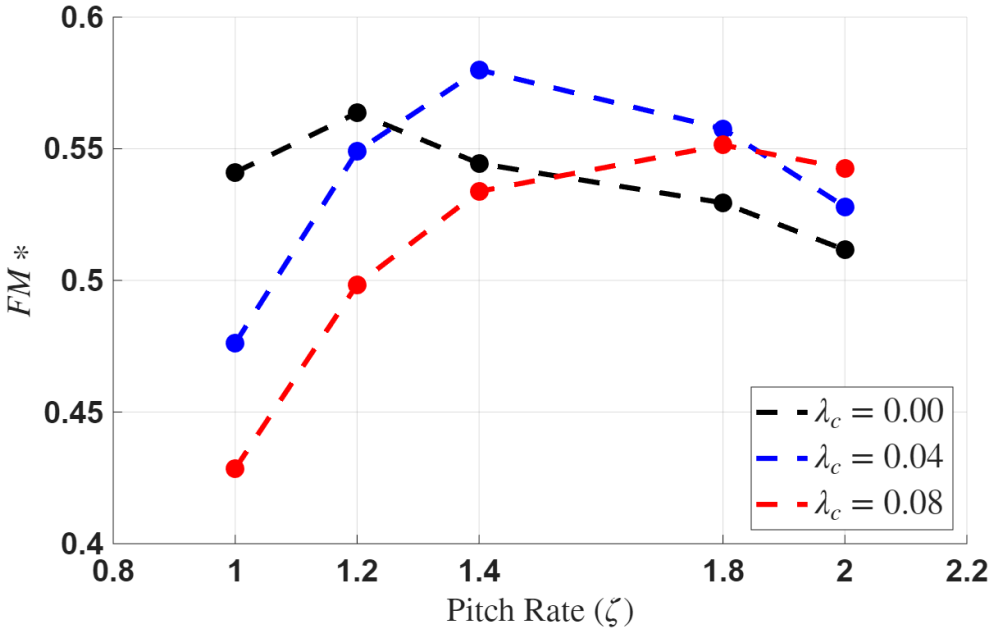

Figure 4.18: Variation of FM^* for varying linear pitch rates at different axial climb speeds

By design, an increasing pitch rate on the aerial screw results in an increase in the localized angle of attack seen by the leading edge. As in the climb inflow increases, the aerial screw with the highest FM^* changes accordingly. Isolating the $\zeta = 1.2$ linear pitch case, this design is seen most efficient in hover.

As the climb inflow increases, FM^* begins to decreases along with the effective angle of attack. When the aerial screws are in a low speed axial climb state, corresponding to $\lambda_c = 0.04$, the most efficient linearly pitched aerial screw becomes the $\zeta = 1.4$ design with $FM^* = 0.58$. It is important to note that the $\zeta = 1.4$ design in a slow axial climb outperforms the $\zeta = 1.2$

design in hover by 2.9%. Despite the $\zeta = 1.4$ design not being optimal in hover among all of the linear pitch cases, it performs better in hover and slow axial climb over a faster axial climb at $\lambda_c = 0.08$.

As the the climb inflow continues to increase to $\lambda_c = 0.08$, the $\zeta = 1.8$ design proves to be most efficient among all linearly pitched aerial screws with $FM^* = 0.55$. An important characteristic to note is the same design in a slower axial climb ($\lambda_c = 0.04$) performs better than at the faster axial climb state. This identifies that a maximum efficiency exists among these linearly pitched aerial screws in between hover and an axial climb state corresponding to $\lambda_c = 0.08$. It is only at a high pitch rate of $\zeta = 2.0$ when FM^* at the higher axial climb state of $\lambda_c = 0.08$ performs better over the slower axial climb ($\lambda_c = 0.04$) and hover states.

4.3.1.3 Off-Axis Climb

The effect of the pitch rate in the off-axis climb state is discussed in this subsection. An azimuthal angle of $\psi = 0$ degrees corresponds to the leading edge of the screw aligned with the positive x-axis. This results in the highest M_{tip} value at an angle of azimuth of $\psi = 90$ degrees. Figures 4.19, 4.20, and 4.21 show the behavior of CF_X, CF_Y, and CF_Z as a function of azimuth. Figures 4.22, 4.23, and 4.24 show the behavior of CM_X, CM_Y, and CM_Z as a function of azimuth. All six force and moment coefficient curves exhibit 1/rev frequencies, consistent with the 1 bladed design of the aerial screws. The peaks in CF_X and CF_Y are offset by 90 degrees, with the side force coefficient (CF_Y) curve leading the propulsive force coefficient (CF_X) curve. Similar behavior is seen between the pitching moment coefficient and the rolling moment coefficient. The peaks of CF_X and CF_Y for the $\zeta = 2.0$ design occur earlier than that of

the $\zeta = 1.0$ design by 15 degrees, though CM_X and CM_Y peaks align across all linearly pitched cases. The variation in the forces and moments in the x and y directions increases as the pitch rate increases. With an increase in pitch rate, the aerial screw becomes taller, stretching the location of the center of gravity further from the leading and trailing edges. This effect causes the loads along the surface of the screw to vary more significantly as the azimuthal station of the screw advances. Higher frequency oscillations also become prevalent as the pitch rate increases near the peaks and troughs of the coefficient plots. The lift coefficient, CF_Z along with the torque coefficient, CM_Z, show a direct correlation between increasing lift and torque generation and and increasing pitch rate. As seen in Figure 4.18, higher pitch rates results in higher efficiency as the climb inflow increases. There is a significant 115% difference between CF_Z for the $\zeta = 2.0$ design and the $\zeta = 1.0$ design. Despite an increase in CF_Z with the pitch rate, there is a limit to where the benefit of efficiency tapers off. While towering screws of pitch rates $\zeta = 1.8$ and $\zeta = 2.0$ perform better in axial climb, they experience significantly larger oscillations in side forces and propulsive forces as well as pitching and rolling moments.

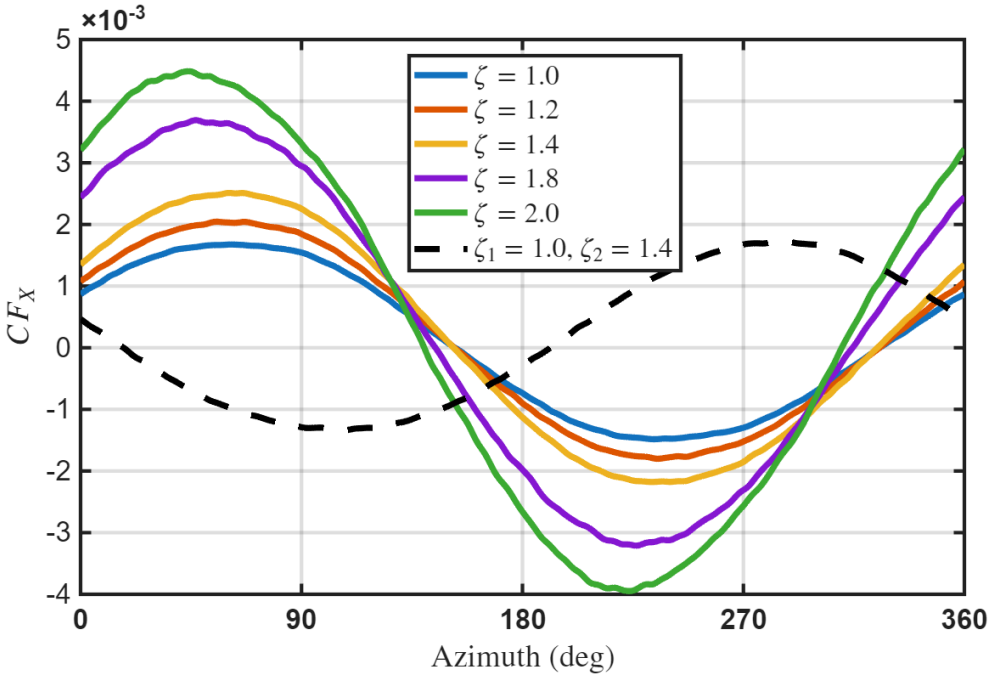

Figure 4.19: CF_X as a function of azimuth for varying pitch rates in off-axis flight

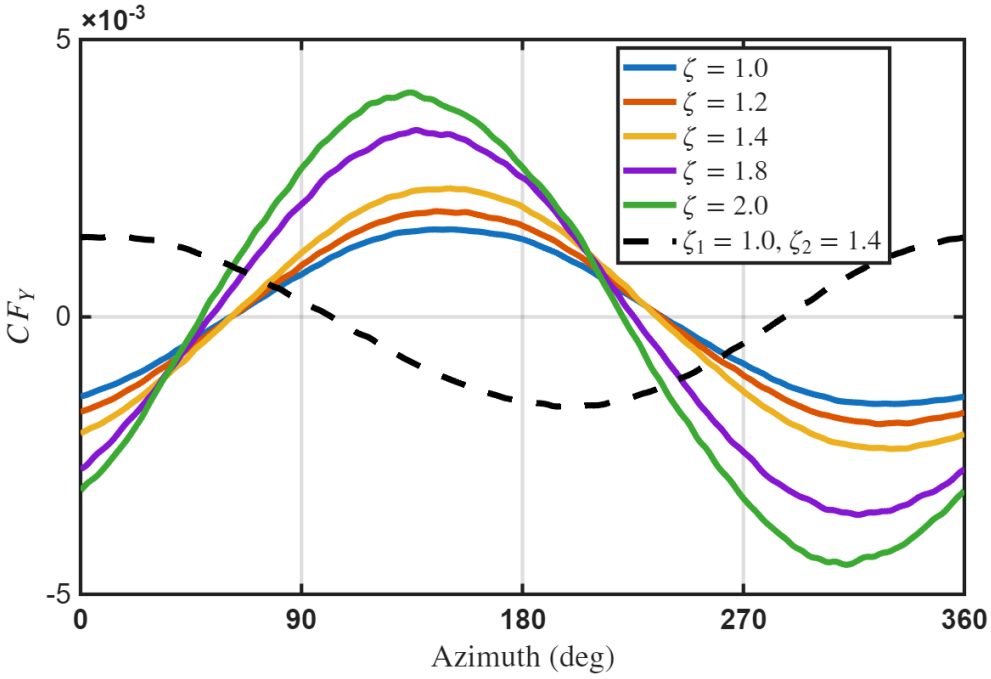

Figure 4.20: CF_Y as a function of azimuth for varying pitch rates in off-axis flight

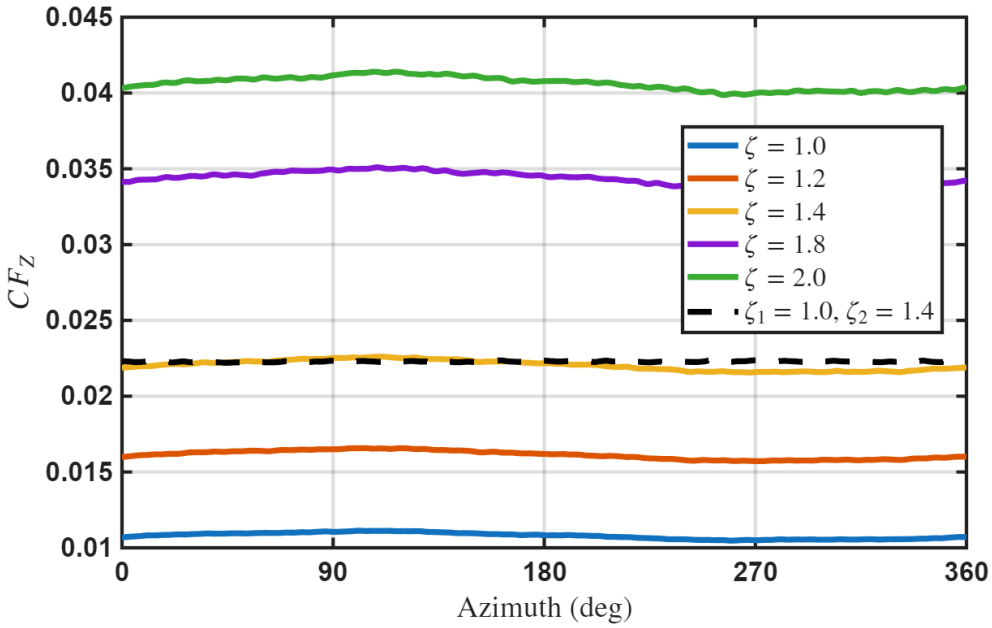

Figure 4.21: CF_Z as a function of azimuth for varying pitch rates in off-axis flight

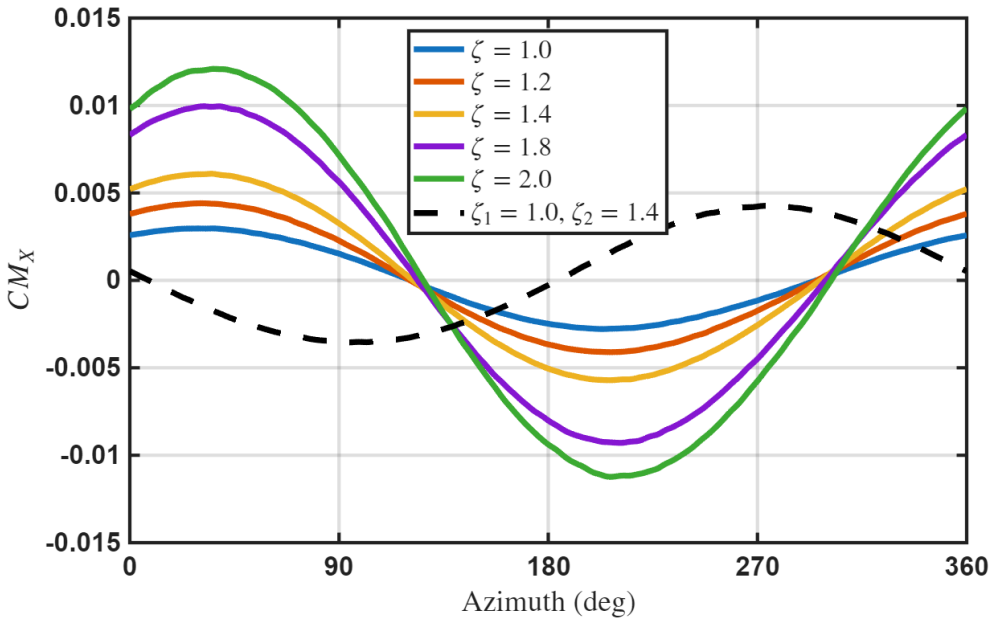

Figure 4.22: CM_X as a function of azimuth for varying pitch rates in off-axis flight

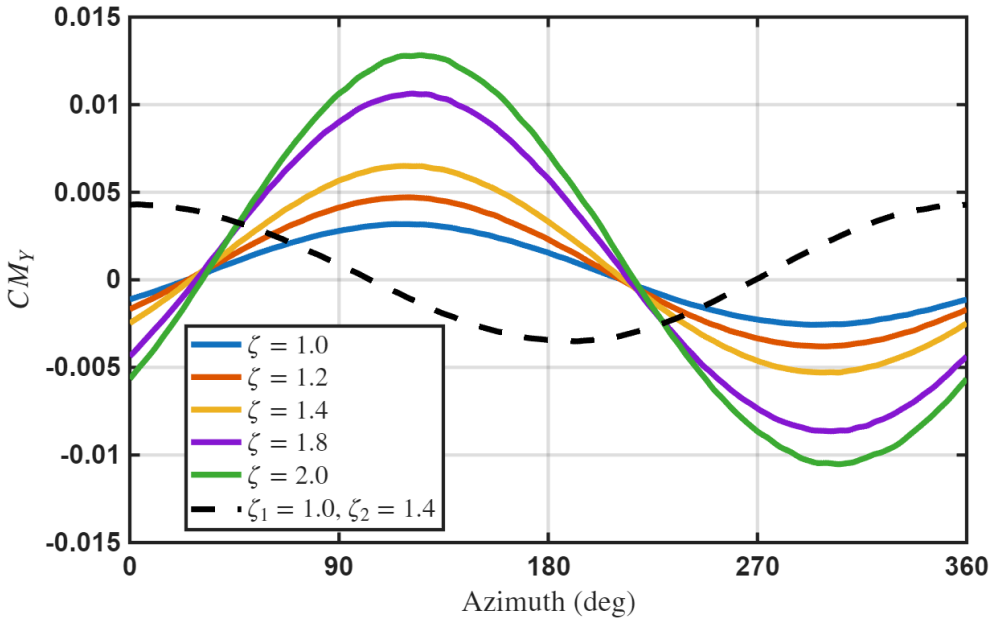

Figure 4.23: CM_Y as a function of azimuth for varying pitch rates in off-axis flight

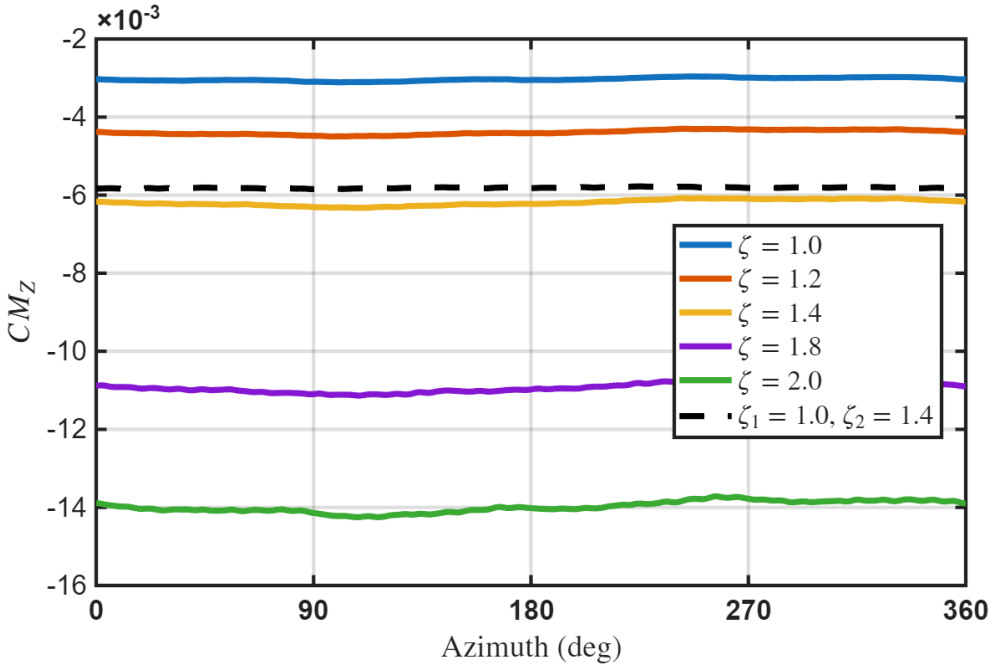

Figure 4.24: CM_Z as a function of azimuth for varying pitch rates in off-axis flight

The bilinearly pitched and tapered aerial screw similarly exhibits a 1/rev oscillation in the forces and moments as functions of azimuth. The magnitude of CF_X, CF_Y, and CF_Z are all similar to that of the linearly pitched, $\zeta = 1.4$ design. Due to the second half the bilinear

screw being pitched at $\zeta = 1.4$, this increase in pitch from the first half's $\zeta = 1.0$ dominates the behavior. Comparing CF_Z between the bilinear screw and the linear $\zeta = 1.4$ design, the behaviors are nearly identical with the bilinear design having a smaller amplitude 1/rev behavior.

4.3.2 Bilinear Pitch Rate

Understanding the variation of the surface aerodynamics indicate the effects of aggressive pitch to be detrimental to the performance of the screw. A uniform pitch rate essentially causes a larger slope at the tip for a tapered screw near the leading edge as compared to the trailing edge. This indicates a possibility of improvement through non-linear variation of pitch to low-moderate rates closer to the leading edge and increased pitch rates towards the trailing edge. This effect is investigated in hover, using a simple bilinear pitch distribution, given by uniform pitch rate for the first and second halves of the screw in this work.

4.3.2.1 Hover

Bilinear pitch rates combine to form an "effective pitch rate" of $\zeta = 1.2$, the optimal linear pitch rate. (A first half pitch rate of $\zeta = 0.8$ with a second half pitch rate of $\zeta = 1.6$ achieves the effective $\zeta = 1.2$) All cases have a linear taper rate of $\eta = 0.5$.

Figure 4.25 shows the figure of merit plotted against the pitch rate of the first half of each of these screws. The datapoint in blue shows the most efficient linear pitch design with $\zeta = 1.2$ for comparison. An initial pitch rate which is less than $\zeta = 1.0$ is results in slight under-performance compared to the linear pitch rate design. The design with an initial pitch rate of $\zeta = 1.1$ performs nearly identical to the linearly pitched design as the pitch rate change becomes close to negligible.

A design where the pitch rate transitions from $\zeta = 1.0$ to $\zeta = 1.4$ raises the figure of merit from .563 to .567, a 0.5% improvement.

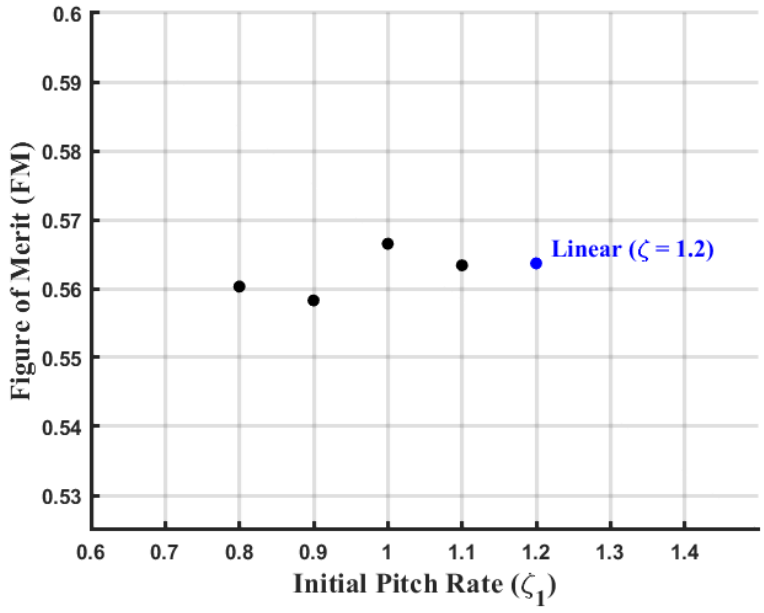

Figure 4.25: Variation of figure of merit of aerial screws with varying bilinear pitch rates

Figure 4.26 shows the normal force and the axial and torque-wise components for the best bilinearly pitched screw in hover ($\zeta_1 = 1.0$, $\zeta_1 = 1.4$). It can be observed that this variation of pitch results in a weaker da Vinci vortex in the first half of the screw followed by a stronger vortical structure in the second half. The axial contribution of the corresponding surface loads is similar to the aggressive pitch scenario in the second half and low pitch scenario in the first half. However, even with the aggressive pitch in the second half, the torque-wise component shows similarities to moderate pitch scenario in the second half and low pitch scenario in the first half. This improved the overall axial loads by $\sim 3\%$ corresponding to an ideal power increment of $\sim 6\%$. However, the actual power requirements increased by $\sim 5\%$, resulting in a slight increase in the figure of merit as seen above.

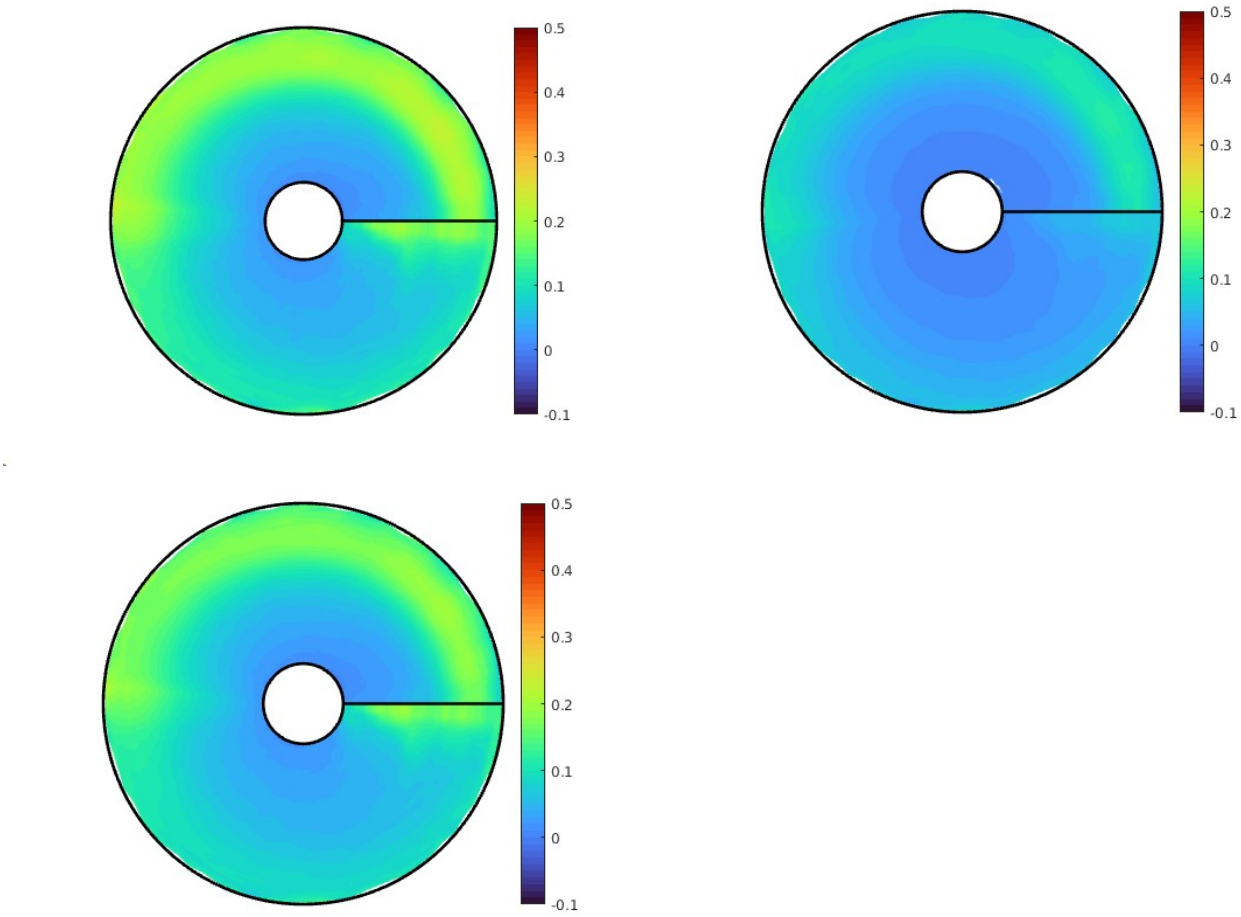

Figure 4.26: Surface load projections onto $r' - \theta$ plane for the bilinear pitch screw with $\zeta = 1$ for upstream half and $\zeta = 1.4$ for downstream half, Top left: ΔC_P, Top right: Axial component and Bottom left: Torque-wise component

The most efficient case with an initial pitch rate of $\zeta = 1.0$ is compared to the initial pitch rate $\zeta = 0.8$ design to further discuss the implications of the bilinear pitch rate.

Figure 4.27 shows the vorticity iso-contour of the $\zeta = 1.0$ initial pitch design. The vortex remains attached to the blade, similar to the linear pitch design.

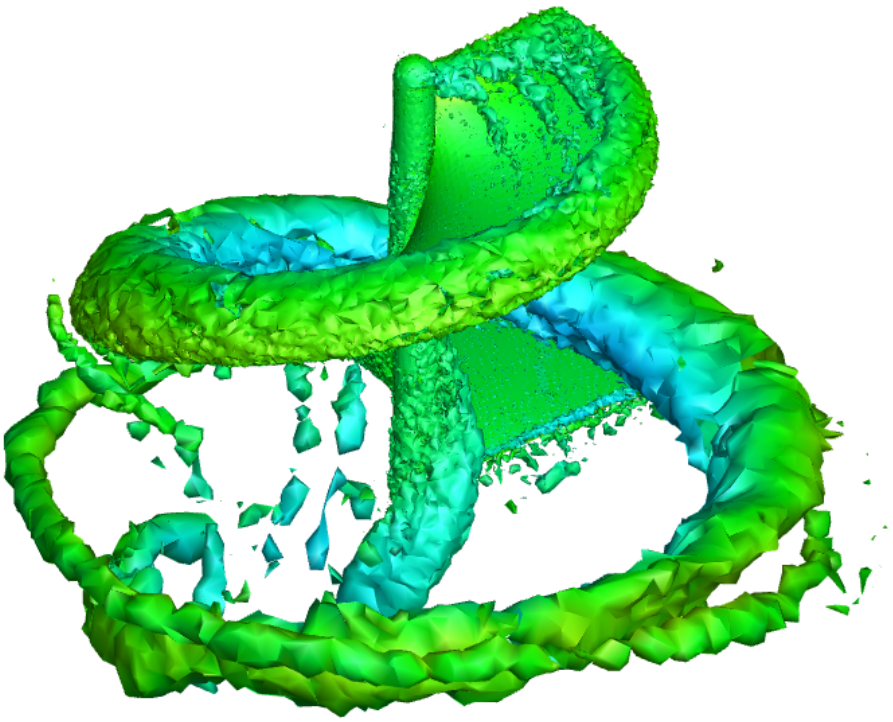

Figure 4.27: Vorticity contour of the $\zeta = 1.0$ to $\zeta = 1.4$ bilinear pitch design

Figure 4.28 shows the vorticity iso-contour of the $\zeta = 0.8$ initial pitch design. The "da Vinci" vortex is evidently weak in the first half of the screw. The sharp increase in pitch rate to $\zeta = 1.6$ significantly increases the vortex strength in the second half of the blade.

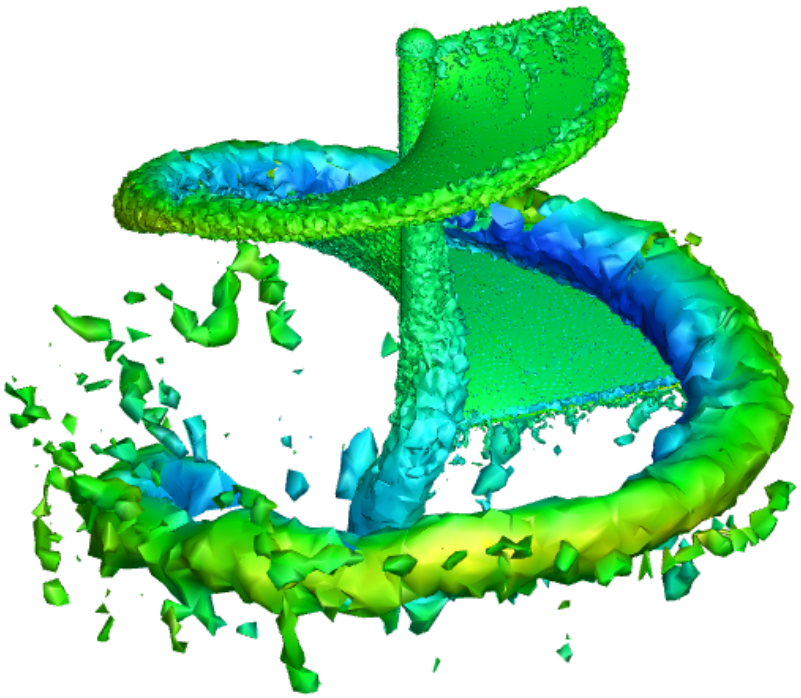

Figure 4.28: Vorticity contour of the $\zeta = 0.8$ to $\zeta = 1.6$ bilinear pitch design

Assessing the pressure distributions of both of these bilinearly pitched designs provides further insights on the effect of pitch on the aerodynamics and performance of aerial screw rotors.

Figure 4.29 shows the pressure distribution of the $\zeta = 1.0$ to $\zeta = 1.4$ bilinear pitch design. The pressure differential on the blade's surface continues to grow as the angle of azimuth increases, suggesting an attached vortex on the rotor blade's tip.

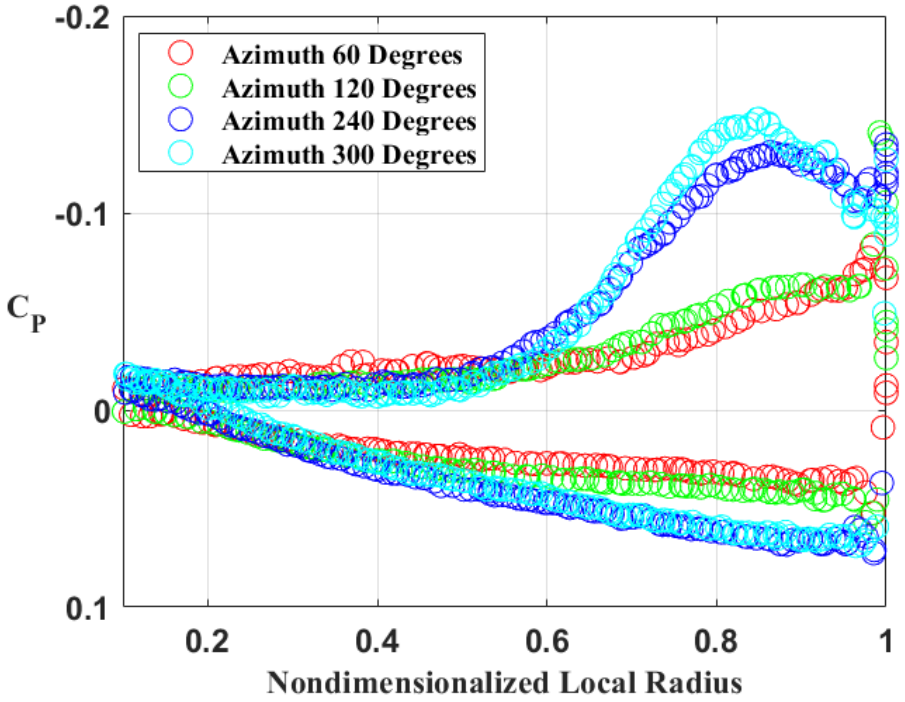

Figure 4.29: Pressure distribution of the $\zeta = 1.0$ to $\zeta = 1.4$ bilinear pitch design

Azimuthal angles of $\psi = 60°$ and $\psi = 120°$ produce nearly identical lift in the first half of the screw. Similarly, angles of $\psi = 240°$ and $\psi = 300°$ produce similar lift in the second half of the screw.

Figure 4.30 shows the pressure distribution of the $\zeta = 0.8$ to $\zeta = 1.6$ bilinear pitch design.

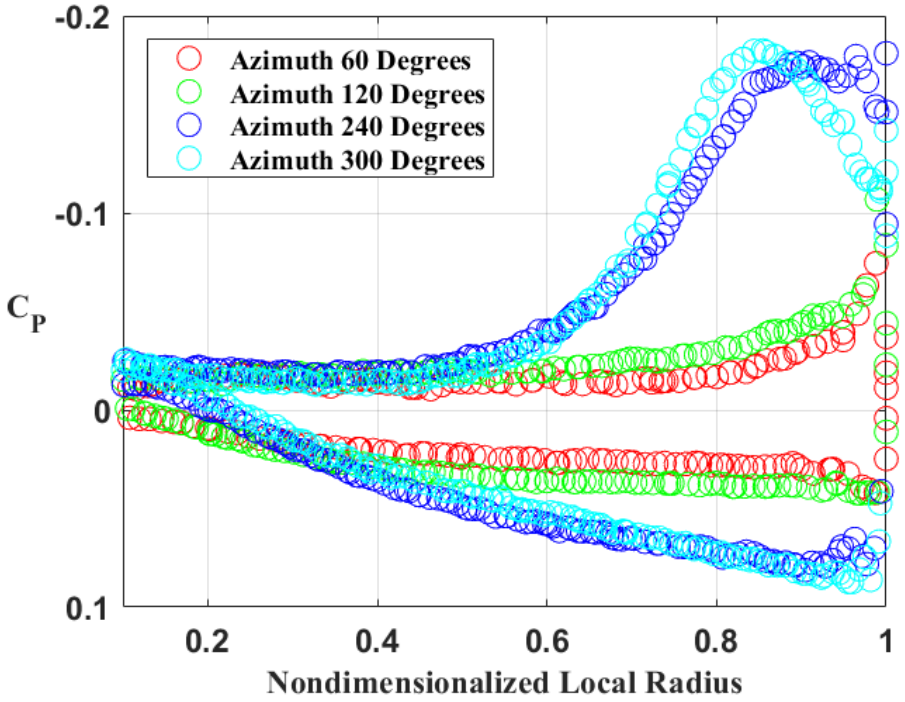

Figure 4.30: Pressure distribution of the $\zeta = 0.8$ to $\zeta = 1.6$ bilinear pitch design

Comparing the $\zeta = 0.8$ to $\zeta = 1.6$ bilinear pitch design to the most efficient, $\zeta = 1.0$ to $\zeta = 1.4$ bilinear pitch design provides some significant insights on the effect of pitch on aerial screw aerodynamics and performance.

As pitch rate decreases, the ”da Vinci” vortex becomes weaker, decreasing the effective lift of the rotor. This is supported by the visible pressure differential decrease near the tip of the blade as pitch rate decreases. This is specifically reflected in the red and green curves in Figures 4.29 and 4.30.

Similarly, it is seen that an increasing pitch rate increases the strength of the ”da Vinci” vortex. The pressure differential significantly increases in the second half of the blade of where the pitch rate is $\zeta = 1.6$ compared to the most efficient design where the pitch rate is $\zeta = 1.4$.

Despite this increase in lift with a higher pitch rate, the evident loss of lift in the first half of

the blade decreases the rotor's overall performance comparing to the $\zeta = 1.2$ linear pitch design. The normal vector orientation points further torque-wise as the pitch rate increases, hindering the rotor's performance as seen in the $\zeta = 0.8$ to $\zeta = 1.6$ bilinear pitch design.

Finding the ideal pitch rate variation requires identifying the optimal trade off between an aggressive pitch rate improving the vortex lift with a minimized power requirement of the rotor.

For a bilinearly pitched design, it is found that this pitch rate change from $\zeta = 1.0$ in the first half of the blade to $\zeta = 1.4$ in the second half of the blade provides the most efficient hover performance with a figure of merit of .567. Differing the location of where the pitch rate changes as well as including more than two pitch rates has potential to further improve aerial screw performance in hover. For this study, only a single pitch rate change at half the span was assessed.

4.4 Taper Rate (η)

This section investigates the effects of linear and bilinear variations of taper rate on the aerodynamics and performance of aerial screws with constant pitch rates.

4.4.1 Linear Taper Rate

Similar to the effect of pitch rate, the effect of linear taper rate on the performance of the screw is studied by comparing the screws with all other design variables unaltered. The majority of the investigation is performed in hover, with preliminary results in axial and off-axis climb states.

4.4.1.1 Hover

Several screws with a constant pitch rate $\zeta = 1.3$ and $R_{\max} = 1$ ft are studied, with each screw having a different uniform taper rate. The tip Mach number and the tip Reynolds number are maintained the same.

Figure 4.31 shows the variation of figure of merit for these screws with the taper rate. It can be seen that the performance of the screw continuously decreases as the taper rate is increased beyond 0.5.

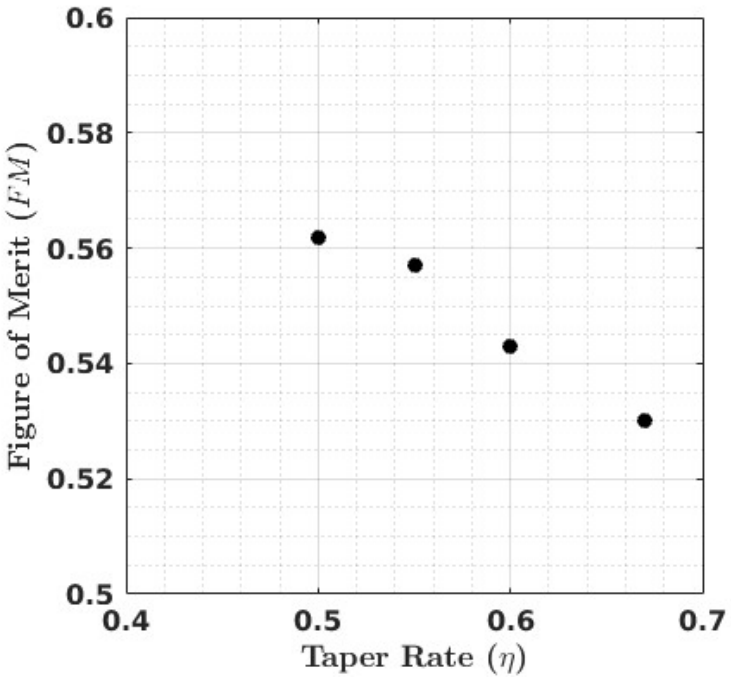

Figure 4.31: Variation of figure of merit of aerial screws with varying taper rate

Figure 4.32 shows the projected surface loads and components for the aerial screw with a taper rate of $\eta = 0.5$. Figure 4.33 shows similar projections for the aggressively tapered aerial screw with $\eta = 0.67$. It can be seen that the strength of the da Vinci vortex is similar for both the taper rates, with variations observed at the leading edge. The aggressively tapered screw shows

minimal separation due to the extremely small aspect ratio and subsequent tip relief effects at the leading edge. However, the vortex strength is continuously fed in due to a more aggressive taper rate, resulting in a similar downstream characteristics of the da Vinci vortex. The effective lifting area of the screw is reduced with increasing taper, resulting in reduction in both axial and torque-wise loads.

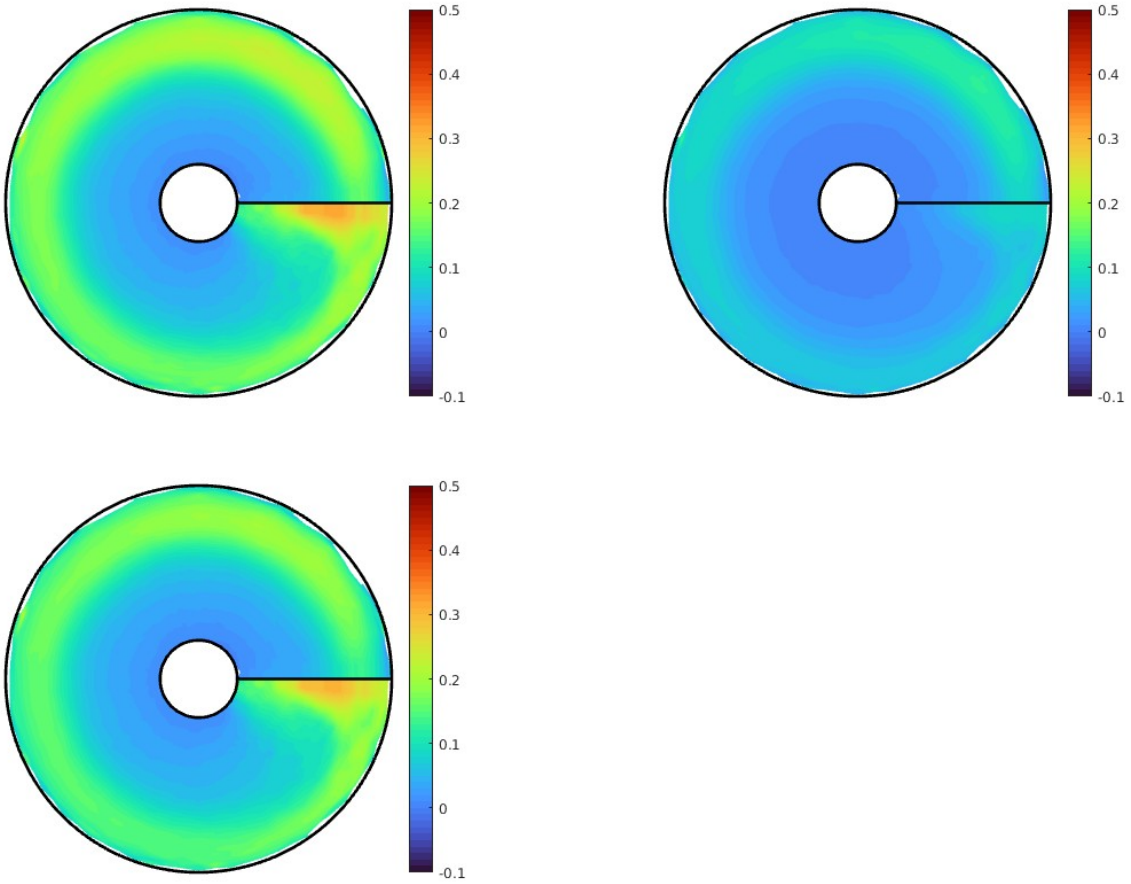

Figure 4.32: Surface load projections onto $r' - \theta$ plane for aerial screw with $\zeta = 1.3$ and $\eta = 0.5$, Top left: ΔC_P, Top right: Axial component and Bottom left: Torque-wise component

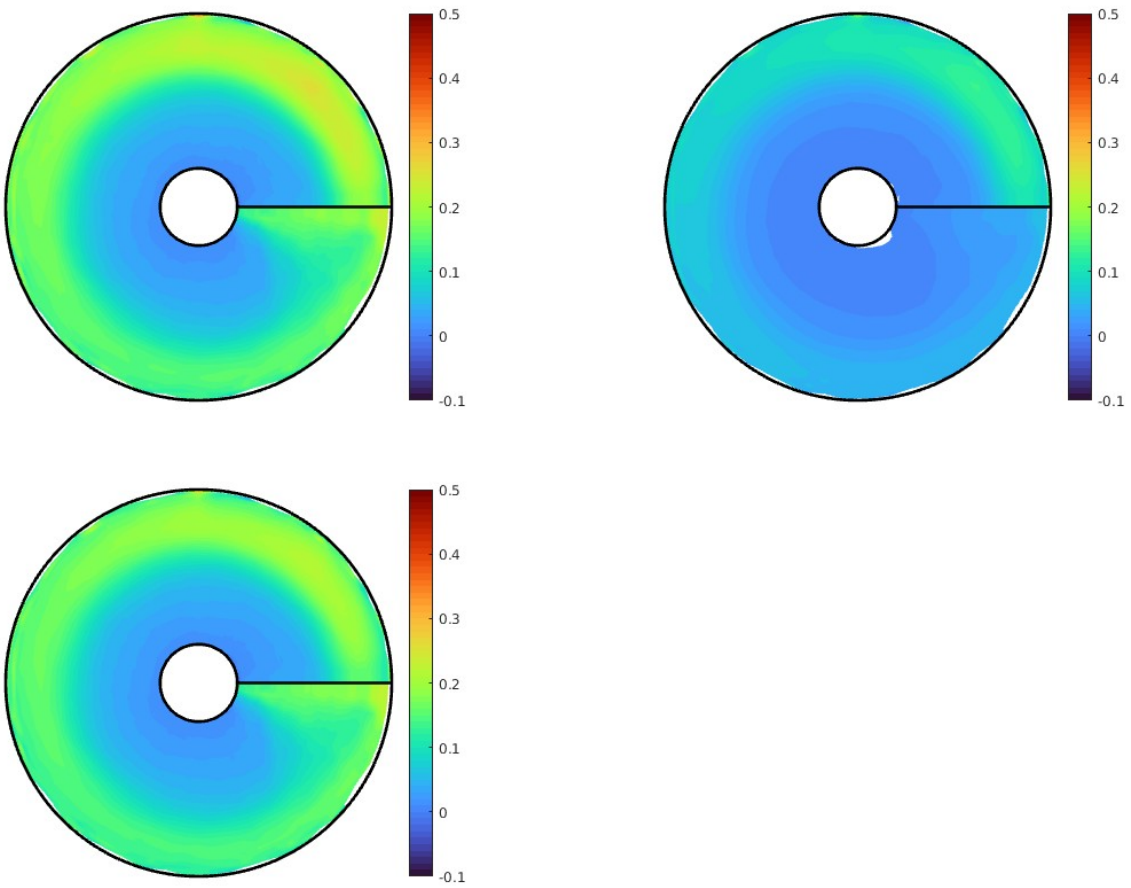

Figure 4.33: Surface load projections onto $r' - \theta$ plane for aerial screw with $\zeta = 1.3$ and $\eta = 0.67$, Top left: ΔC_P, Top right: Axial component and Bottom left: Torque-wise component

The reduction in axial loads from moderate to aggressive taper are observed to be $\sim 8.5\%$, which corresponds to an ideal power reduction of $\sim 13\%$. However, the actual power requirement is reduced by $\sim 7.5\%$, indicating poor performance of the aggressively tapered screw. The additional power requirements can be attributed to the effects of radial flow which are more prominent in the aggressively tapered screw.

A comparison of the best performing linear taper rate design ($\eta = 0.5$) and the most aggressive linear taper rate ($\eta = 0.66$) is discussed to assess the effects of an increasing taper rate on the physics and performance.

Figure 4.34 shows the vorticity iso-contour of the $\eta = 0.5$ linear taper rate design and Figure 4.35 shows the same for the $\eta = 0.66$ linear taper rate design. Both vorticity contours show an attached "da Vinci" vortex. The distinguishing feature between the differing designs with a linear taper rate is the radius of the leading edge. A larger taper rate corresponds to a smaller leading edge radius. This relationship means that as taper rate is increased, there is an expected loss of lifting area for the rotor.

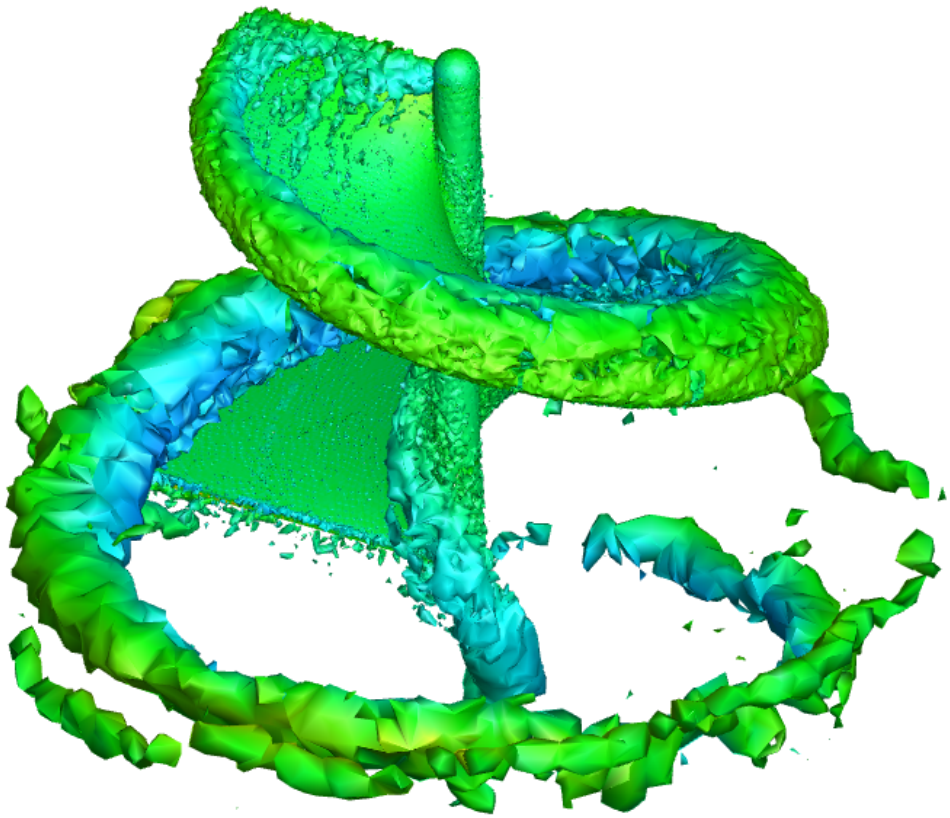

Figure 4.34: Vorticity contour of the $\eta = 0.5$ linear taper rate design

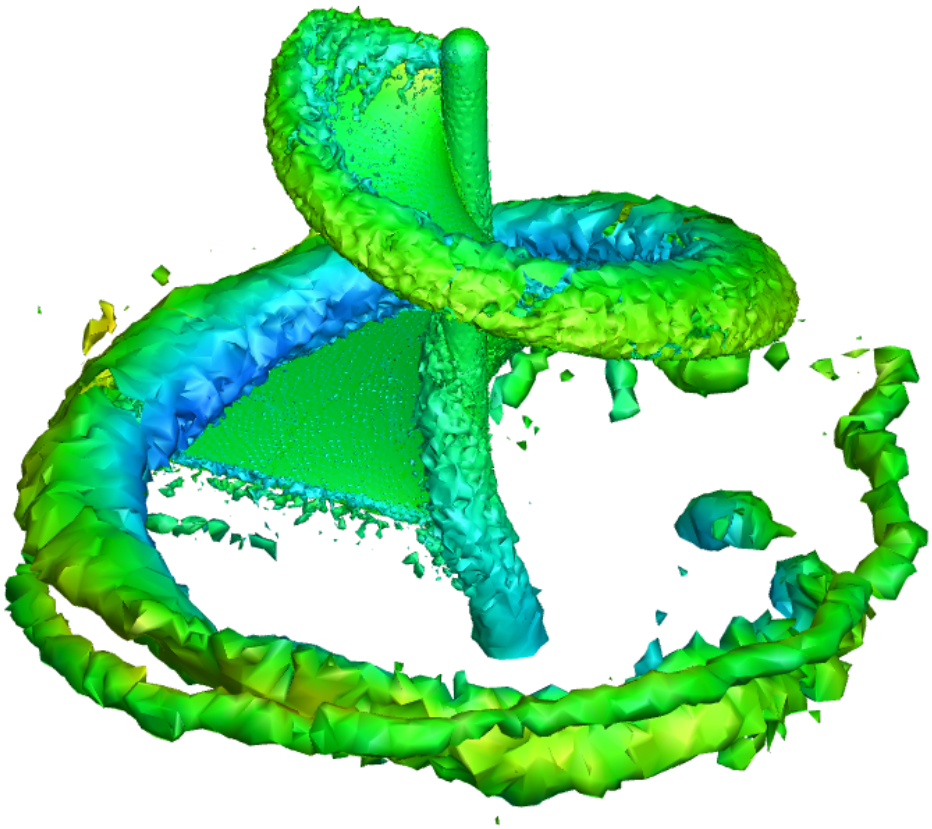

Figure 4.35: Vorticity contour of the $\eta = 0.66$ linear taper rate design

To understand the benefits of including a taper with an aerial screw rotor, pressure distributions were extracted for the $\eta = 0.5$ design and the $\eta = 0.66$ design. This data provides further insights on the physics of the ”da Vinci” vortex and how to further improve rotor performance.

Figure 4.36 shows the pressure distribution of the $\eta = 0.5$ linear taper design.

This pressure distribution shows that with a tapered rotor, the da Vinci vortex moves inboard as it continues to develop along the blade of the rotor. The peaks from the pressure distribution plot can be seen to move from $r = 0.9R$ to $r = 0.8R$ as angle of azimuth increases. Since this is a commonality between the linear pitch and bilinear pitch cases mentioned, this phenomenon can be attributed to the taper of the rotor.

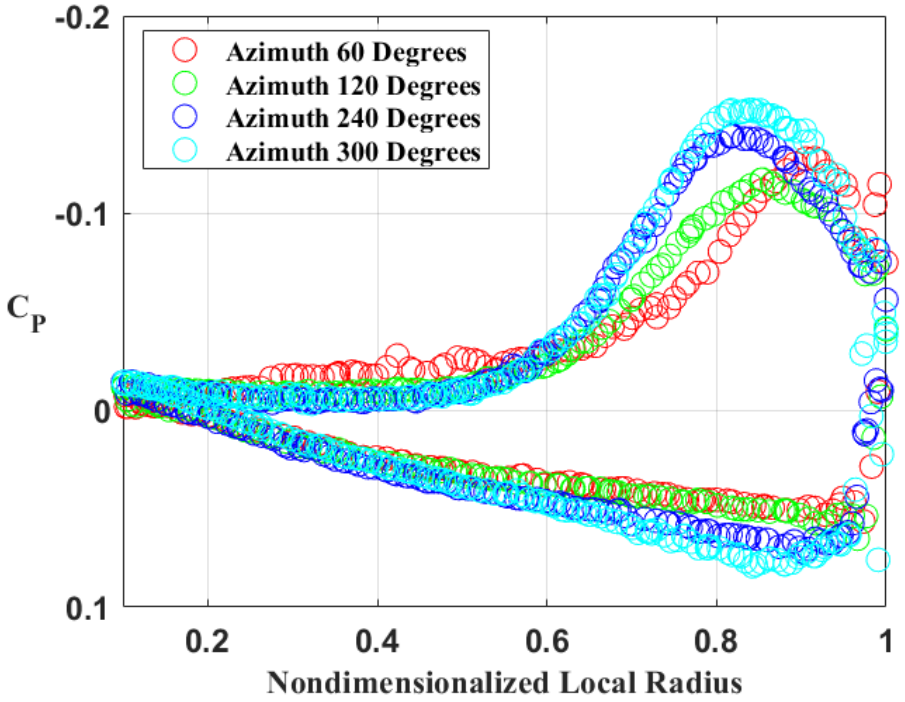

Figure 4.36: Pressure distribution of the $\eta = 0.5$ linear taper design

Figure 4.37 shows the pressure distribution of the $\eta = 0.66$ linear taper design.

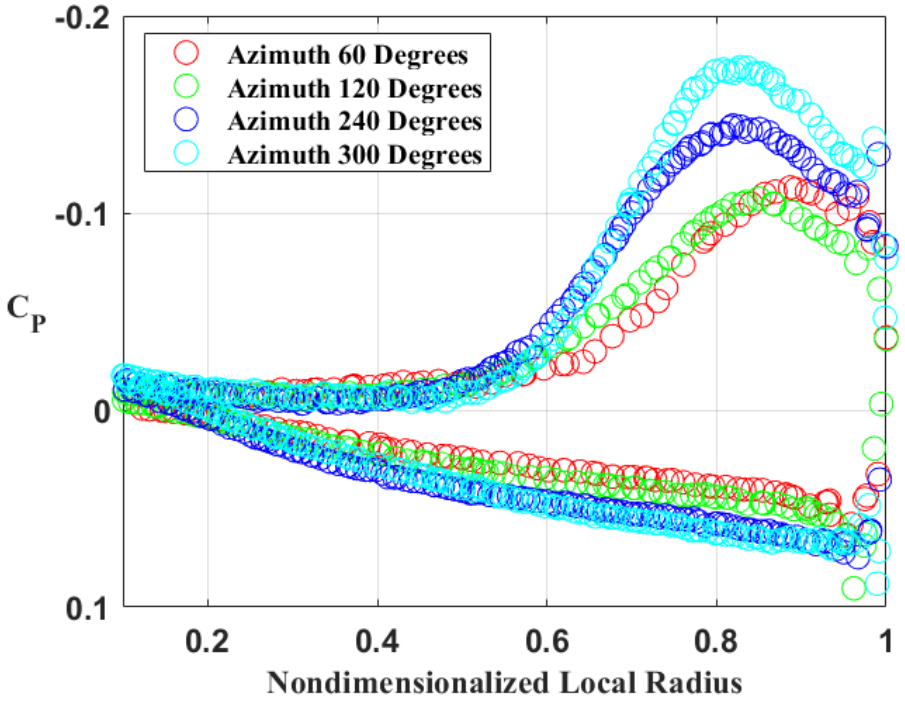

Figure 4.37: Pressure distribution of the $\eta = 0.66$ linear taper design

Comparing Figures 4.36 and 4.37, it is found that increasing the taper rate of the rotor from $\eta = 0.5$ to $\eta = 0.66$ increases the vortex strength as it moves down the span of the blade. The pressure differential increases as angle of azimuth increases in the $\eta = 0.66$ case, displaying the vortex's increase in strength.

Once again, comparing the location of the peaks with respect to azimuthal locations along the rotor blade, the vortex continues to moves inboard as it develops down the rotor blade.

Despite a stronger vortex developed when taper rate is increased, there is a maximum benefit to an aggressive taper rate. As taper rate increases, lifting surface is lost. This study identified that for a linearly tapered rotor at a fixed pitch rate of $\zeta = 1.3$, a taper rate of $\eta = 0.5$ provides the most efficient design with a figure of merit of 0.562.

4.4.1.2 Axial Climb

To understand the effect of taper rate in axial climb, several one bladed screws with a constant taper rate $\zeta = 1.3$ and $R_{\max} = 1$ ft are studied, with each screw having a different linear taper rate. The tip Mach number at the trailing edge is once again maintained at 0.37 with a tip Reynolds number of 2.63×10^6 for all screw designs. Figure 4.38 shows the efficiency of aerial screws with different linear taper rates in hover. The figure of merit steadily decreases from $\eta = 0.5$ to $\eta = 0.66$. The most efficient aerial screw in hover among linearly tapered designs is when $\eta = 0.5$, corresponding to $FM^* = 0.56$.

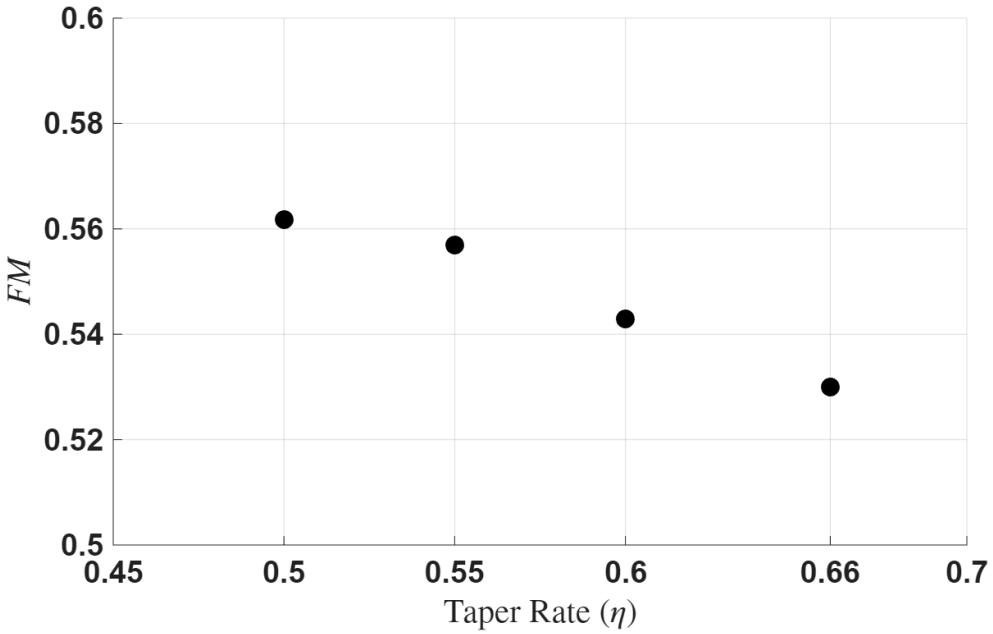

Figure 4.38: Variation of figure of merit of aerial screws with varying pitch rate in hover

The four designs with varying linear taper rates were investigated at axial climb states corresponding to $\lambda_c = 0.04$ and $\lambda_c = 0.08$, shown in Figure 4.39. Similarly to Figures 4.15 and 4.16, it is expected to see both thrust and power coefficients decreasing with an increase in the climb inflow. In hover ($\lambda_c = 0.0$), there is a 9.1% difference in the thrust coefficients between the

$\eta = 0.5$ design and the $\eta = 0.66$ design as well as a 7.8% difference in the power coefficients. As the climb speed increases, the difference in performance between the two taper rate extremes drops significantly. At $\lambda_c = 0.08$, the difference in thrust and power coefficients between the two taper rate extremes reduces to 0.22% and 0.44% respectively.

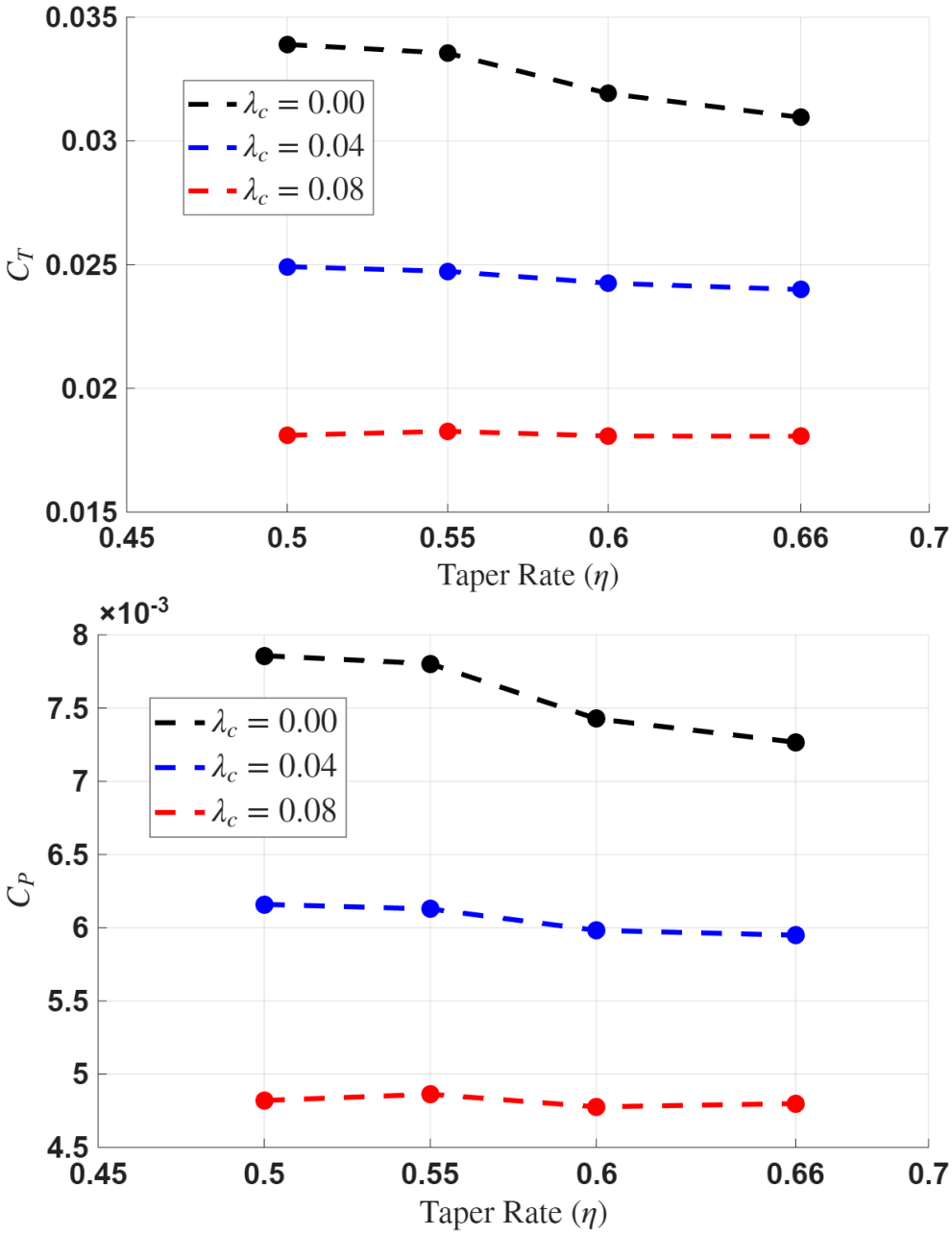

Figure 4.39: Variation of C_T and C_P for varying linear taper rates at different axial climb speeds

Figure 4.40 shows the variation of FM^* with differing taper rates at changing axial climb speeds. Again, the difference in FM^* between the $\eta = 0.5$ design and the $\eta = 0.66$ design drops as the climb inflow increases. It is revealed that the importance of the taper rate lessens as the axial climb velocity increases. In hover, the $\eta = 0.5$ design provides a balance between sufficient lifting area and the ability to strengthen the vortex. As the taper rate increases, the vortex strength further increases yet the loss in lifting area on the aerial screw surface results in a decrease in efficiency to $FM^* = 0.53$. In the case where $\lambda_c = 0.08$, the taper rate plays an insignificant role in the performance, the majority of the physics are dominated by the pitch rate, $\zeta = 1.3$. Between the $\eta = 0.5$ and $\eta = 0.66$ designs, there is a 0.15% difference in FM^*. It is important to note that despite effectively negligible change in the performance across all taper rates when $\lambda_c = 0.08$, the $\eta = 0.66$ design is more efficient in the high axial climb state than in hover and slow axial climb. A more aggressive taper ratio tends to decrease the efficiency of the rotor in hover and low speed axial climb. The angle of attack the aerial screw sees due to a higher total inflow decreases at $\lambda_c = 0.08$ to a point where the effect of taper becomes insignificant and the $\eta = 0.66$ design outperforms lower inflow cases.

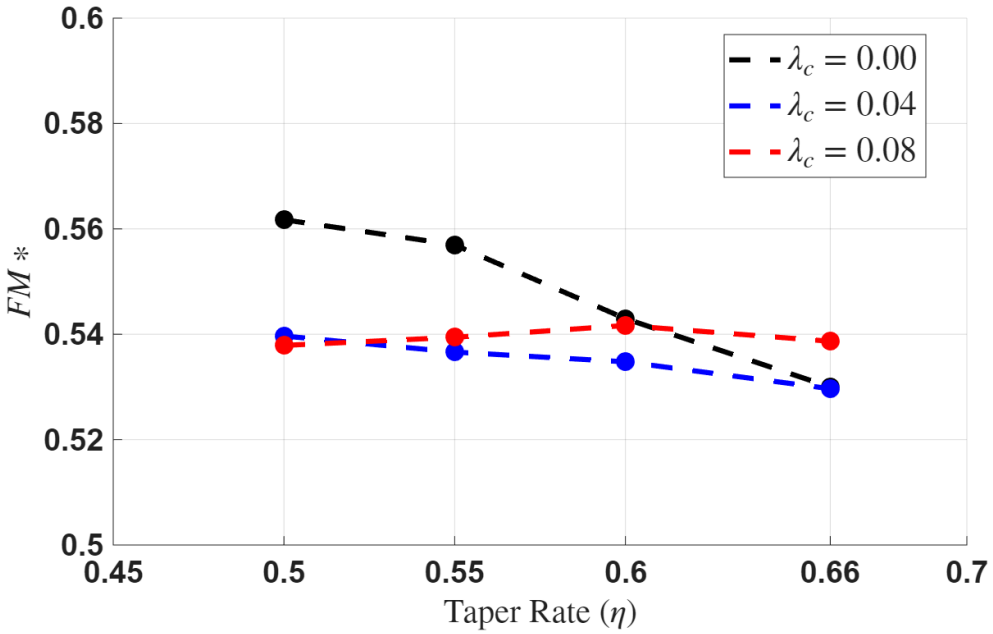

Figure 4.40: Variation of FM^* for varying linear taper rates at different axial climb speeds

4.4.1.3 Off-Axis Climb

The effect of the taper rate in the off-axis climb state is discussed in this subsection. All linear taper rate varying designs again have a fixed linear pitch of $\zeta = 1.3$. Figures 4.41, 4.42, and 4.43 show the behavior of CF_X, CF_Y, and CF_Z as a function of azimuth. Figures 4.44, 4.45, and 4.46 show the behavior of CM_X, CM_Y, and CM_Z as a function of azimuth. All six force and moment coefficient curves exhibit 1/rev frequencies, consistent with the 1 bladed design of the aerial screws. The peaks in CF_X and CF_Y are offset by 90 degrees, with the side force coefficient (CF_Y) curve leading the propulsive force coefficient (CF_X) curve. Similar behavior is seen between the pitching moment coefficient and the rolling moment coefficient. An increase in the taper rate results in higher amplitude oscillations in the force and moment frequencies. This is due to an increase in the imbalance of loads along the surface of the screw as the leading edge shortens compared to the trailing edge. Despite this, it is evident that the variation in force

and moment coefficients is significantly less than in the case of varying the linear pitch rate, specifically in the CF_Z and CM_Z plots. A phase offset of 30 degrees exists in the force and moment variations in the x and y directions where the $\eta = 0.66$ design leads the $\eta = 0.5$ design. Along the entire azimuthal variation of the loads in the axial force direction, there is a maximum difference of 1.2% between the $\eta = 0.5$ design and the $\eta = 0.66$ design. This further validates the finding of the pitch rate being a dominant parameter in the lifting force coefficient in climb states for one bladed aerial screws.

The bilinearly pitched and tapered aerial screw has a similar amplitude in the 1/rev behavior to all varying linear taper aerial screw designs in CF_X, CM_X, CF_Y, and CM_Y. All linearly tapered aerial screws have a linear pitch rate of $\zeta = 1.3$, similar to the bilinear case with the initial pitch rate of $\zeta = 1.0$, transitioning to $\zeta = 1.4$. Despite the similarities in the rolling and pitching directions, all linear taper rate cases have an average CF_Z near 0.018. The bilinear case has an average CF_Z slightly above 0.022. This difference is caused by the second half pitch rate, $\zeta = 1.4$, dominating the lift as seen in the previous section. A similar difference in trend is noticed in the torque coefficients between all cases.

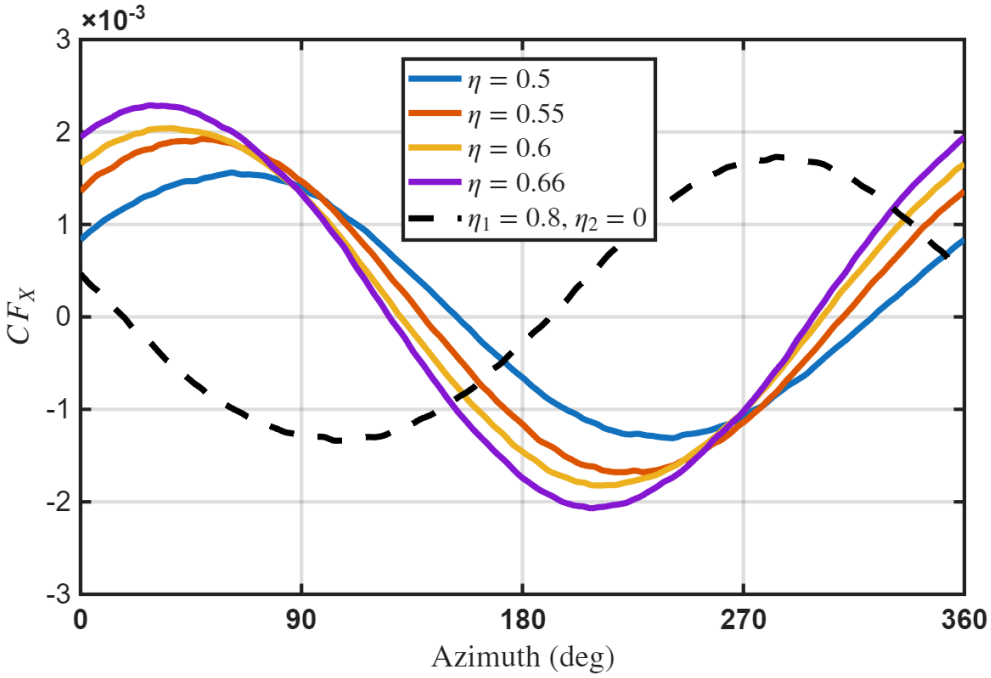

Figure 4.41: CF_X as a function of azimuth for varying taper rates in off-axis flight

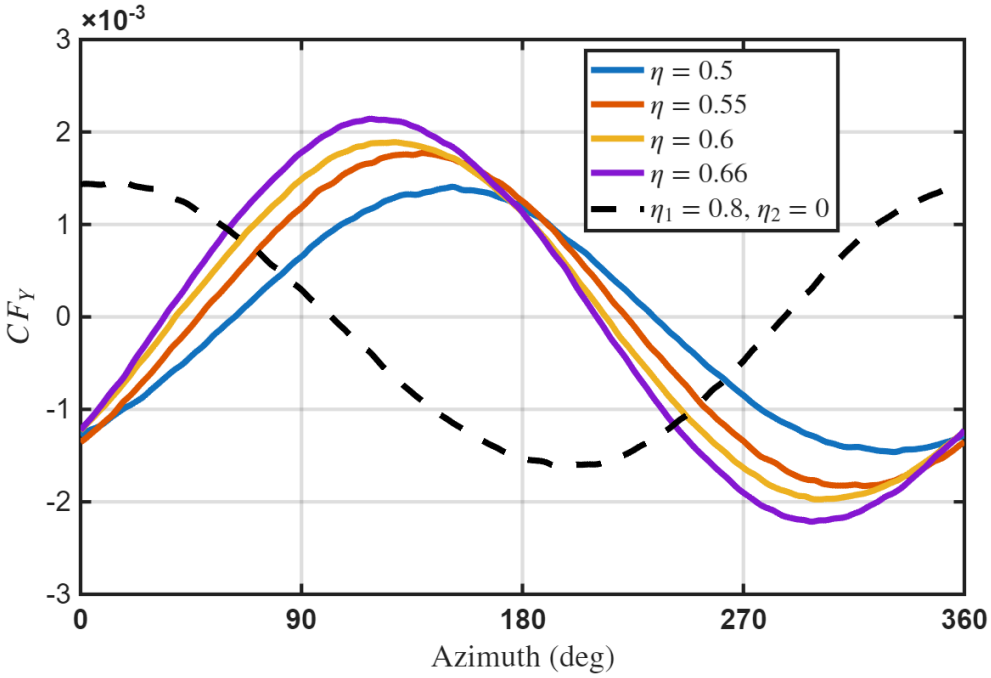

Figure 4.42: CF_Y as a function of azimuth for varying taper rates in off-axis flight

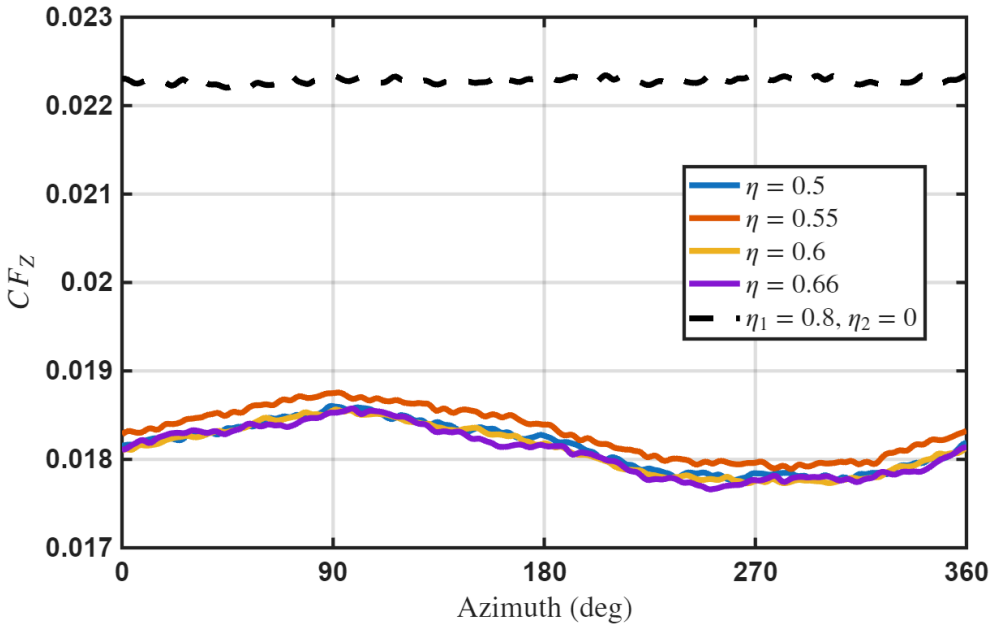

Figure 4.43: CF_Z as a function of azimuth for varying taper rates in off-axis flight

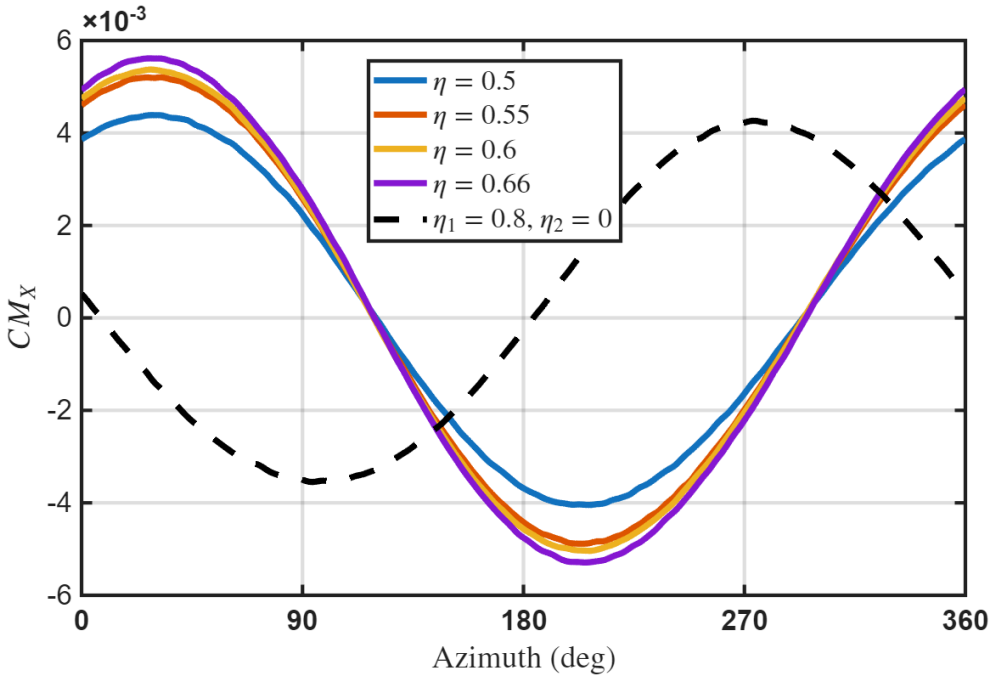

Figure 4.44: CM_X as a function of azimuth for varying taper rates in off-axis flight

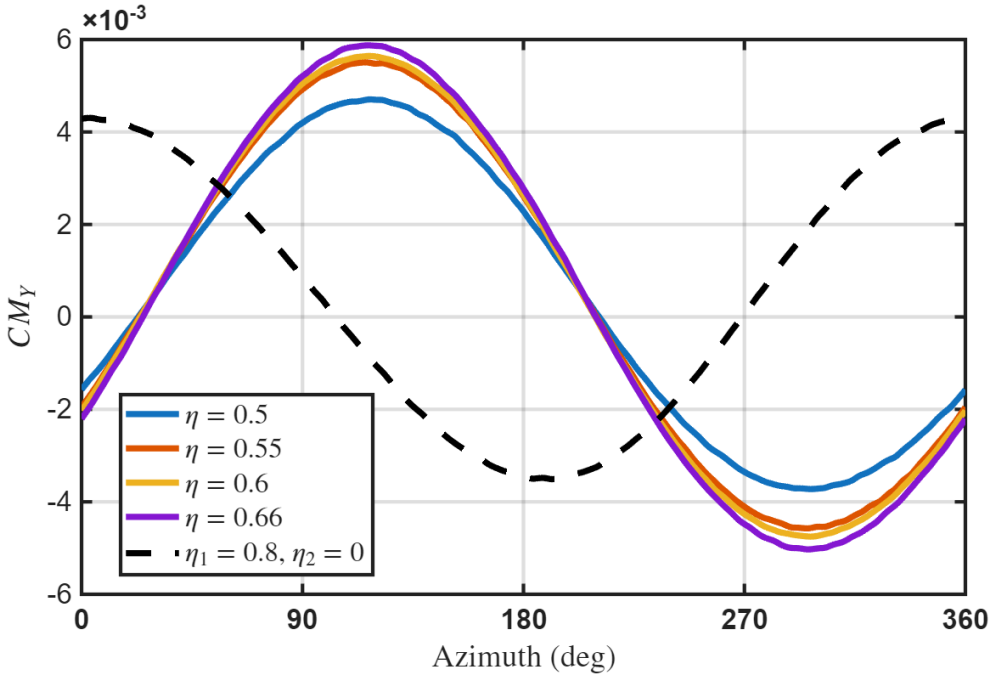

Figure 4.45: CM_Y as a function of azimuth for varying taper rates in off-axis flight

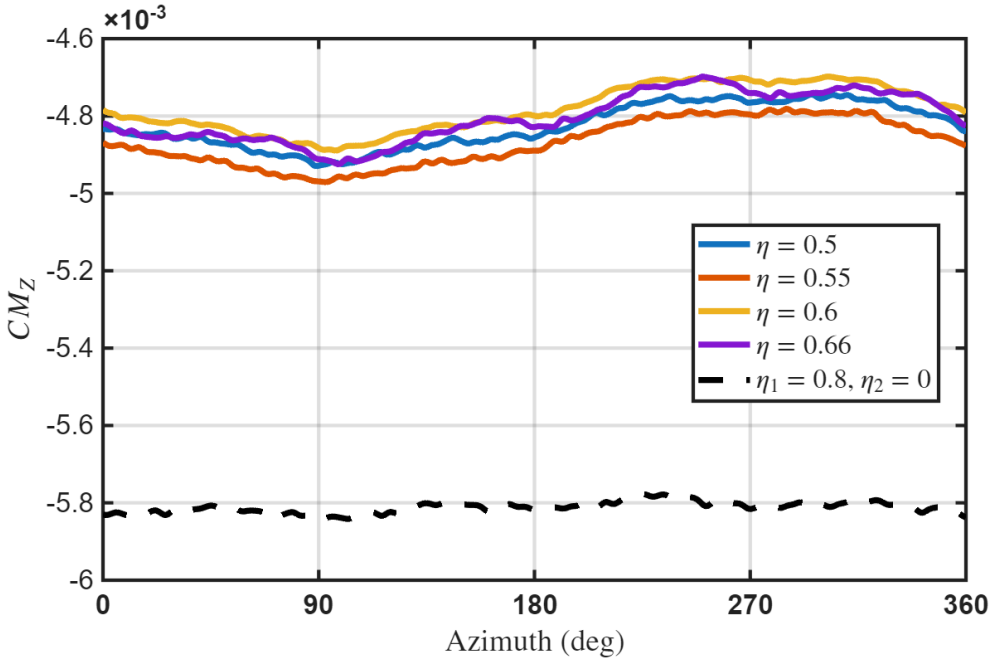

Figure 4.46: CM_Z as a function of azimuth for varying taper rates in off-axis flight

4.4.2 Bilinear Taper Rate

Similar to the investigation of bilinear pitch rates, bilinear taper rate variations are assessed with constant linear pitch rates. To understand the effect of nonlinear taper, a bilinear variation of taper is developed where the first half of the screw has a uniform taper rate and the second half is untapered. To achieve a similar leading edge size, the taper rate is required to be extremely aggressive, since the maximum radius for these screws is achieved within half rotation.

4.4.2.1 Hover

In the investigation of bilinear taper rates, the pitch rate is held constant at a linear $\zeta = 1.2$ to match the best linear pitch rate in hover. Figure 4.47 shows the variation of figure of merit for these rotors, indicating better hover performance when the second half is left untapered.

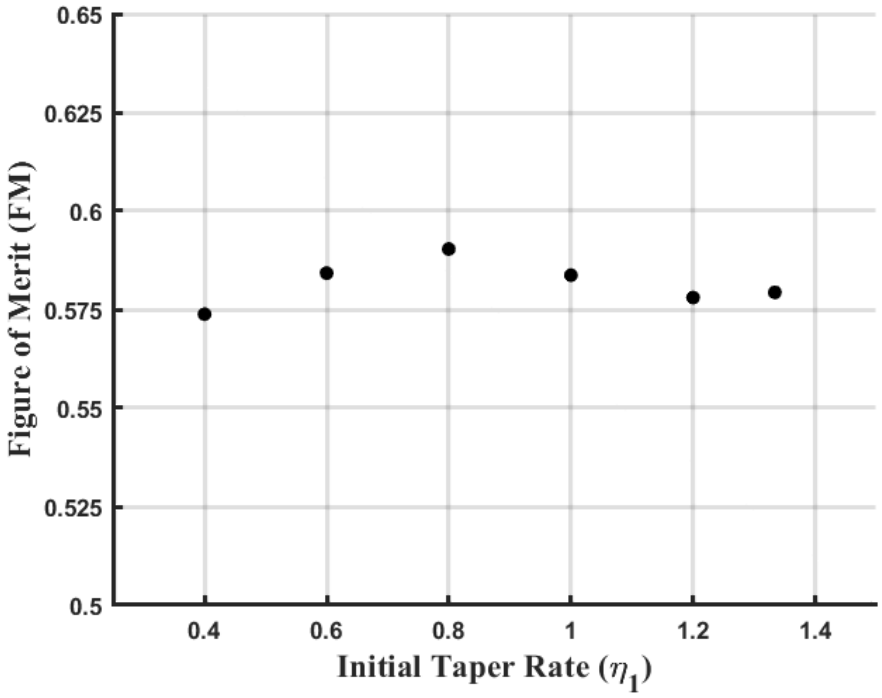

Figure 4.47: Variation of figure of merit of bilinearly tapered aerial screws with varying initial taper rate

Figure of merit increases as the initial taper rate increases from $\eta = .4$ to $\eta = .8$. The figure of merit then begins to decrease, showing there exists a maximum benefit to an aggressive taper in the first half of the blade.

The design with an initial taper rate of $\eta = 0.8$ proves to be the most efficient out of the dataset, achieving a figure of merit of .59. This design change provides a significant improvement of 5% between the linearly and bilinearly tapered rotors.

Figure 4.48 shows the surface normal loads and their axial and torque-wise components for the best performing screw with $\eta_1 = 0.8$. It can be seen that the strength of the da Vinci vortex is maintained along the first half screw surface where the screw is tapered. The strength of the vortex lowers along the downstream in the untapered region of the screw. This is because the vortex is no longer bound to the tip of the screw as the vortical structure is no longer strengthened

by the untapered blade. However, the strength of the vortex built in the first half blade region is sufficiently sustained through the next half rotation, rendering the surface active in thrust generation.

These results indicate that aggressive taper is not beneficial for the aerodynamic performance of the screw. Low to moderate taper is however required for the da Vinci vortex to be developed and confined to the tip of the screw surface.

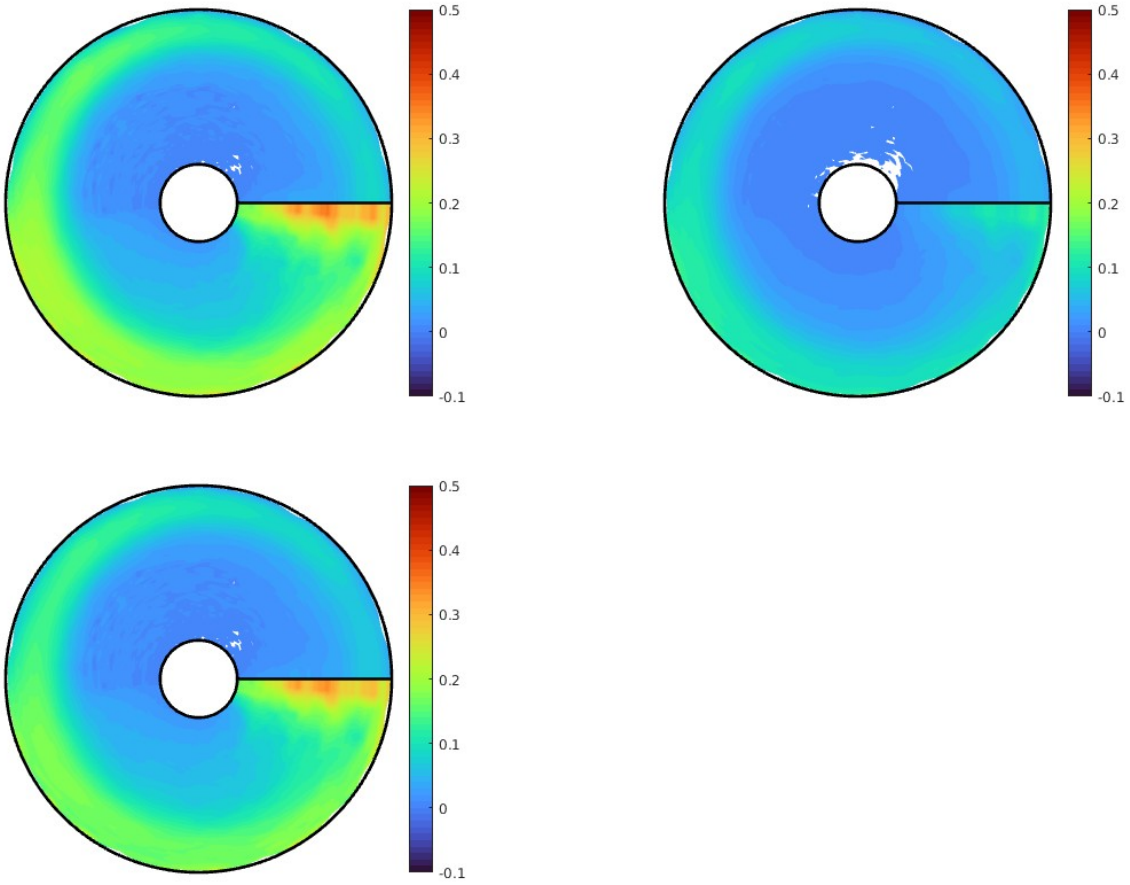

Figure 4.48: Surface load projections onto $r' - \theta$ plane for aerial screw with $\zeta = 1.3$ and bilinear taper with $\eta_1 = 0.8$, Top left: ΔC_P, Top right: Axial component and Bottom left: Torque-wise component

A comparison of the best performing rotor and the most aggressively tapered rotor was done to expand on the effects of taper rate on the aerial screw design. It also provides insights on

how the ”da Vinci” vortex is affected by an untapered rotor after the maximum radius is reached at half span.

Figure 4.49 shows the vorticity iso-contour of the $\eta = 0.8$ initial taper rate design and Figure 4.50 shows the vorticity iso-contour of the $\eta = 1.33$ initial taper rate design.

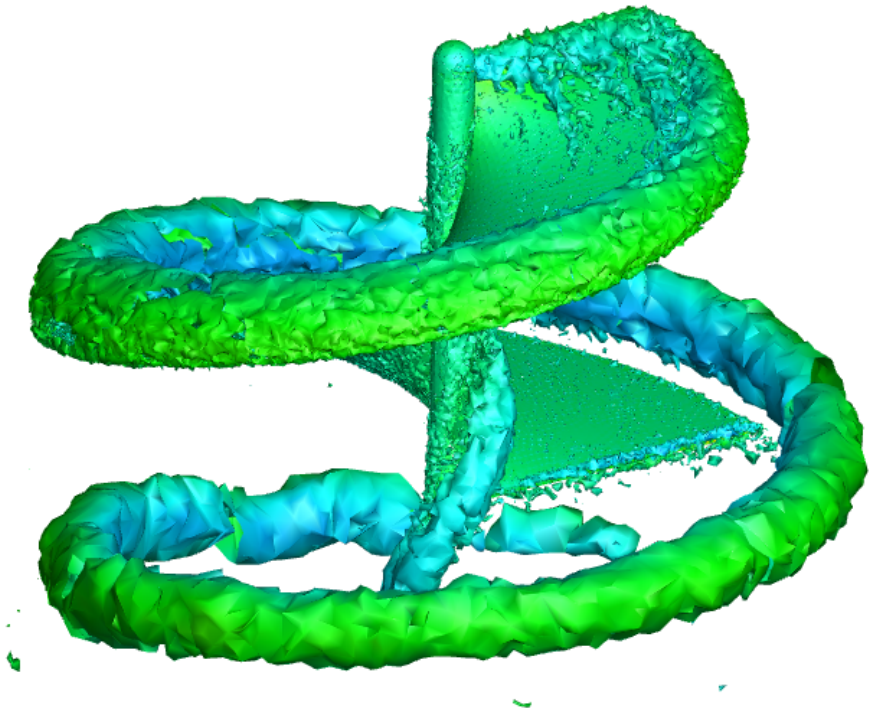

Figure 4.49: Vorticity contour of the $\eta = 0.8$ initial taper rate design

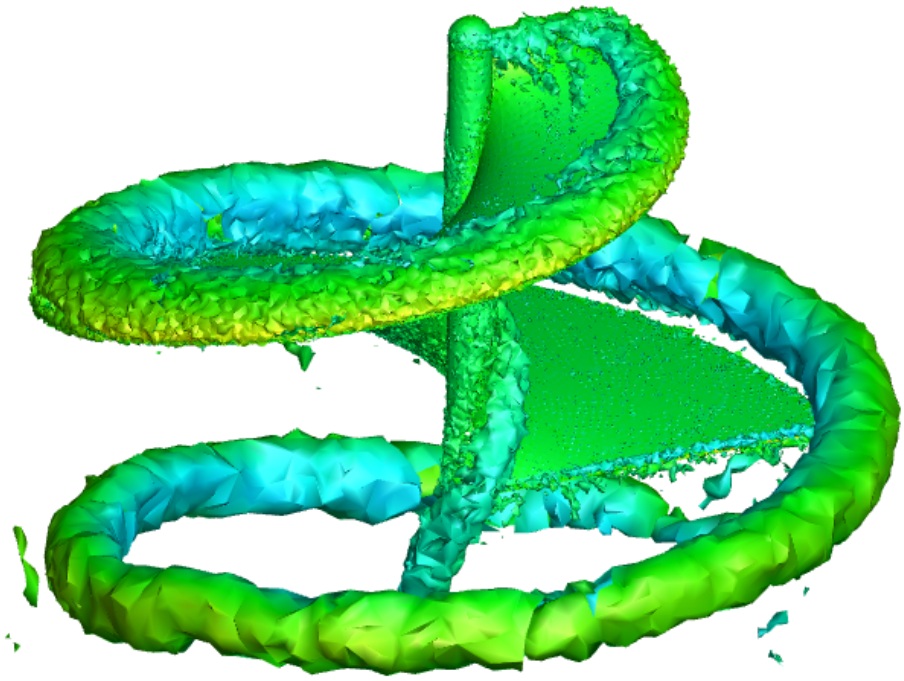

Figure 4.50: Vorticity contour of the $\eta = 1.33$ initial taper rate design

From these visualizations, it is evident that a taper rate is key in keeping the vortex attached. Once the vortex reaches half way down the rotor blade, it detaches for these designs due to the untapered geometry.

Despite this, the vortex is still able to effectively develop in the first half of the blade. All rotor designs with an untapered second half outperformed the best linearly tapered design. This suggests that using as much lifting surface area as possible for a given maximum radius design is crucial to improving rotor performance.

By assessing the pressure distributions of these two designs, the effects of aggressive tapers as well as untapered segments on the rotor's performance are further understood.

Figure 4.51 shows the pressure distribution of the $\eta = 0.8$ initial taper design.

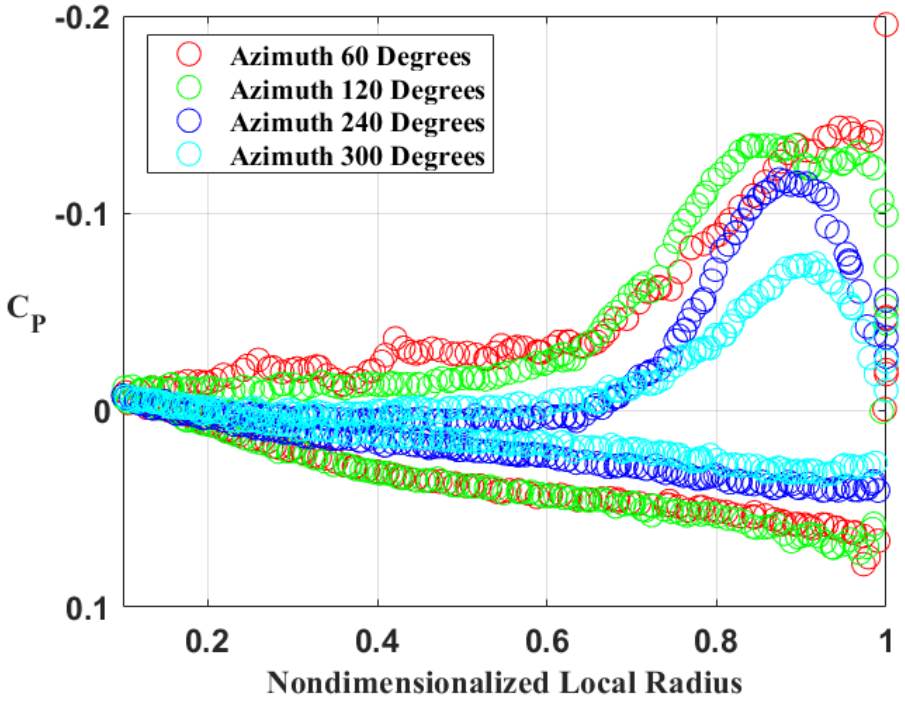

Figure 4.51: Pressure distribution of the $\eta = 0.8$ initial taper design

The aggressive taper in the first half of the blade generates a significantly larger pressure differential compared to the linearly tapered case in the first half of the blade. It is also confirmed that the ”da Vinci” vortex detaches as there is less lift being generated in the untapered section of the blade than the tapered section.

Figure 4.52 shows the pressure distribution of the $\eta = 1.33$ initial taper design.

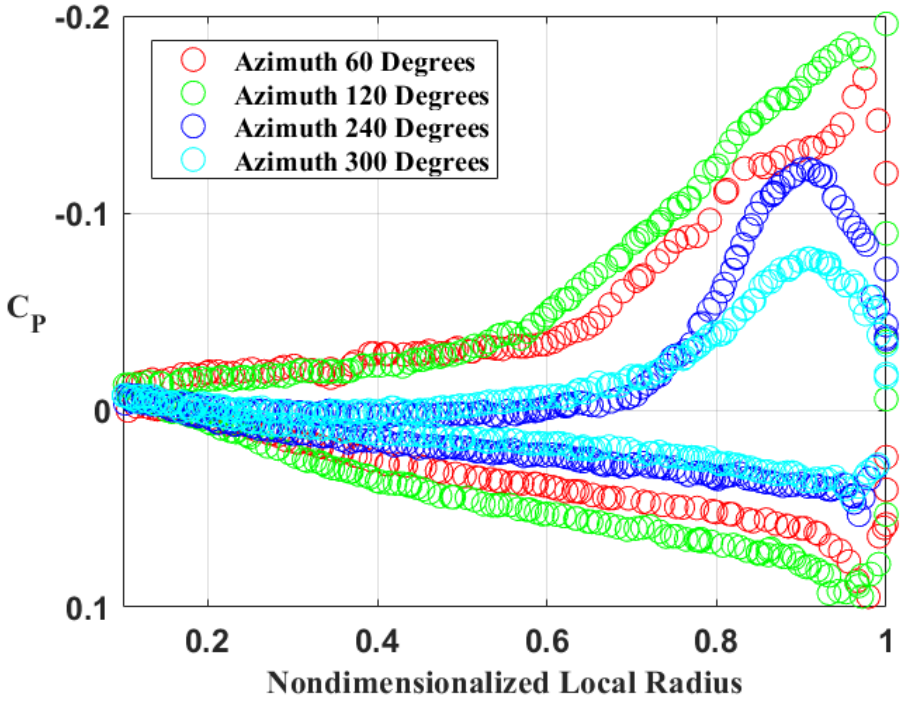

Figure 4.52: Pressure distribution of the $\eta = 1.33$ initial taper design

The pressure distribution from the aggressively tapered case furthers the idea that an increasing taper rate increases the strength of the "da Vinci" vortex.

Comparing Figures 4.51 and 4.52, there is a significant jump in the pressure differential in the first half of the blade for the aggressively tapered case. Regardless of the strength of the vortex in the first half of the blade, transitioning to an untapered design in the second half of the blade detaches the vortex, resulting in similar lift between both of these designs.

Although the pressure distribution seems to suggest more lift is produced for the aggressively tapered case, the loss in lifting area reduces the performance of the rotor. The aggressively tapered design with an initial taper rate of $\eta = 1.33$ achieves a figure of merit of .58, nearly a 2% decrease in performance from the most efficient design.

4.5 Bilinear Pitch Bilinear Taper

The bilinearly pitched design where $\zeta = 1.0$ transitioned to $\zeta = 1.4$ outperformed all linearly pitched designs as previously mentioned. Similarly, the bilinearly tapered design where the initial taper rate was $\eta = 0.8$ achieved a figure of merit of 0.59, the highest out of all datasets.

These results suggest that combining a bilinear pitch rate with a bilinear taper rate would have the potential to further improve the performance the current aerial screw design.

For this work, the most efficient bilinearly pitched and bilinearly tapered designs were combined in hopes to improve the rotor's overall hover performance. This design entails an initial pitch rate of $\zeta = 1.0$ and an initial taper rate of $\eta = 0.8$ in the first half of the screw. The second half of the screw has a pitch rate of $\zeta = 1.4$ and is untapered.

4.5.1 Hover

To understand the performance of the bilinear pitch rate, bilinear taper rate case in hover, the conditions are matched with previous sections parameters: $R_{\max} = 1\,\text{ft}$, $M_{tip} = 0.25$, corresponding to a tip Reynolds number of 1.7×10^6.

Figures 4.53 and 4.54 show that the bilinear design significantly outperforms previous test cases in hover. The red data point shows the bilinearly pitched and tapered design. The blue data point in Figure 4.53 refers to the $\zeta = 1.2$ linearly pitched design.

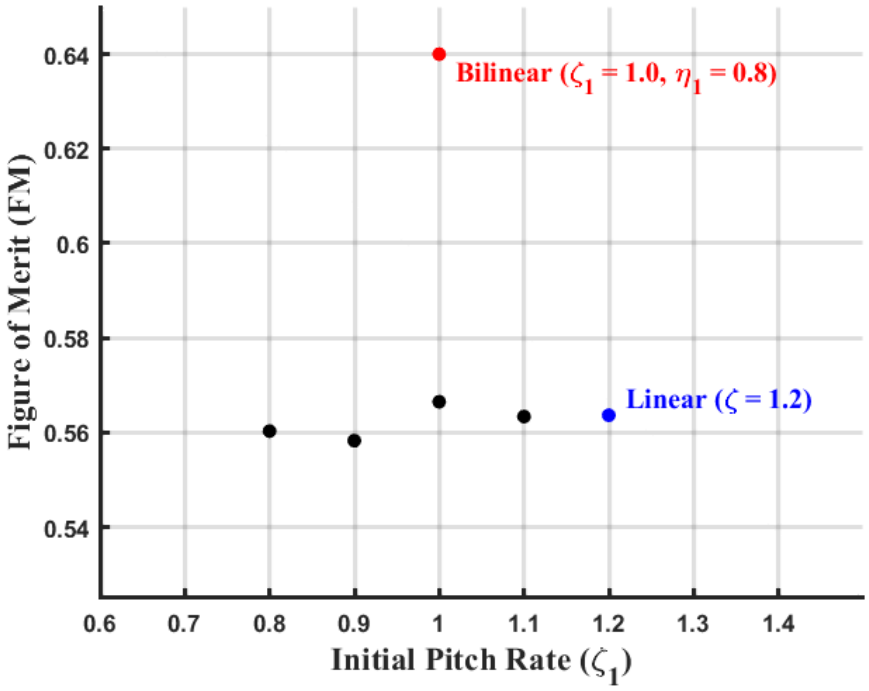

Figure 4.53: Variation of figure of merit of bilinearly tapered aerial screws with varying initial pitch rate

The bilinearly pitched and tapered design achieved a figure of merit of 0.64 at $M_{tip} = 0.25$.

Combining a bilinear pitch with a bilinear taper resulted in a 12.9% improvement compared to the best bilinearly pitched and linearly tapered design and a 13.7% improvement over the best linearly pitched design.

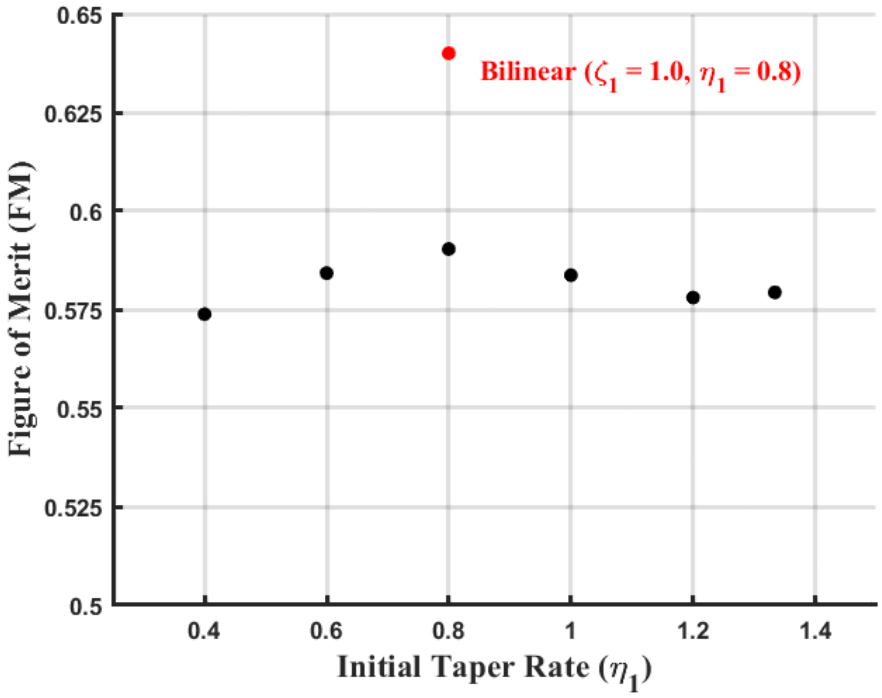

Figure 4.54: Variation of figure of merit of bilinearly tapered aerial screws with varying initial taper rate

Once again, a significant improvement is seen with the bilinearly pitched and tapered design when comparing to the solely bilinearly tapered rotors. There is an 8.5% improvement in figure of merit when comparing the bilinearly pitched and tapered rotor to the best bilinearly tapered rotor.

Figure 4.55 shows the vorticity iso-contour of the bilinearly pitched and tapered design.

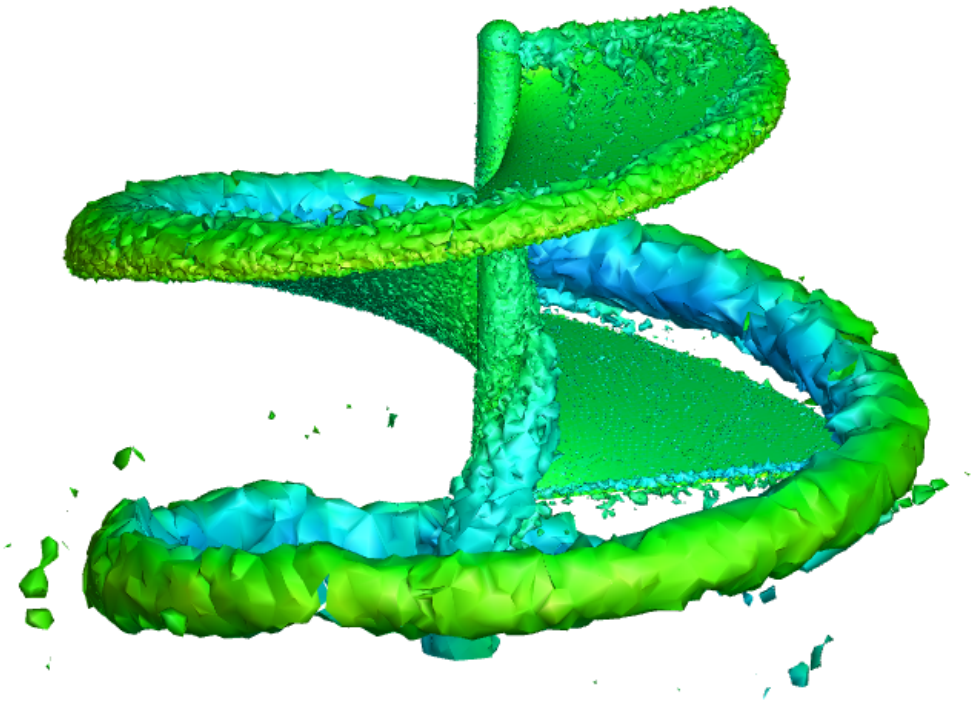

Figure 4.55: Vorticity contour of the bilinearly pitched and bilinearly tapered design

Figure 4.56 shows the pressure distribution of the bilinearly pitched and tapered design. A key feature to the improvement in performance of the rotor is the uniformity in the pressure distribution plot across different angles of azimuth. The locations of where the majority of the lift is being generated are more uniform in the bilinearly pitched and tapered design. Improving the lift generation across differing angles of azimuth while maintaining the uniform location of where the vortex lies is key to further improving these aerial screw rotors in the future.

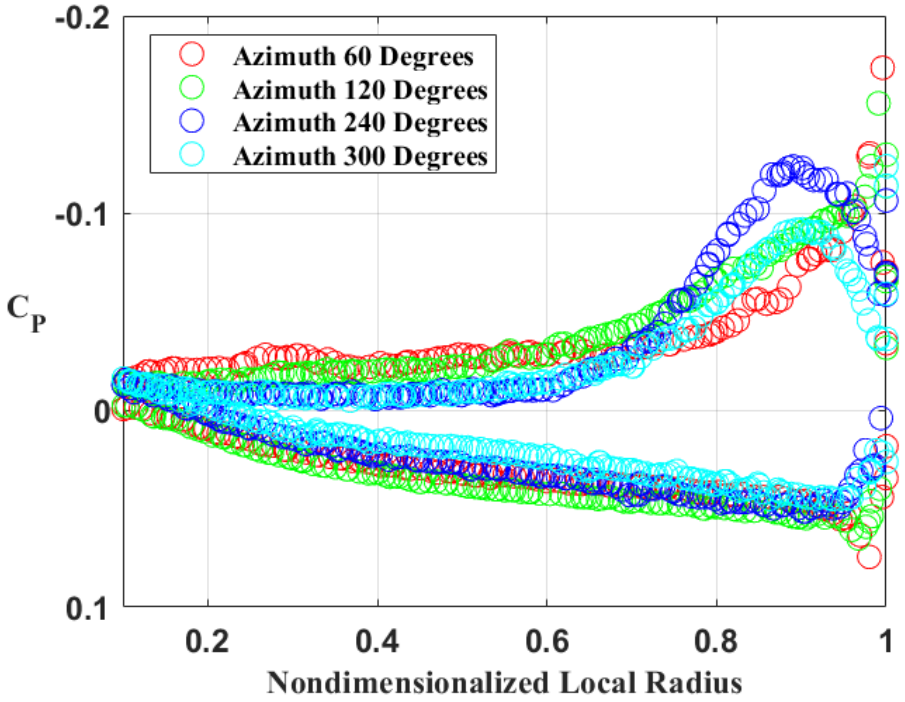

Figure 4.56: Pressure distribution of the bilinearly pitched and bilinearly tapered design

Figure 4.57 shows the side force variation with azimuth in hover for the linearly pitched ($\zeta = 1.2$) aerial screw and the bilinearly varying screw. The phase offset between both cases is found to be inherent to the geometry of the aerial screws themselves. With the linearly pitched screw, the surface normals do not experience significant changes from the first half to second half of the blade. For the bilinear screw, the surface normals change significantly from the first half to second half of the blades. This causes a significant difference in the pressure differentials across the surfaces for both the linear and bilinear case, attributing to a phase shift of 180 degrees between cases.

Table 4.1 closely examines the pressure and skin friction force contributions between the linearly pitched ($\zeta = 1.2$) and linearly tapered ($\eta = 0.5$) aerial screw and the bilinearly pitch ($\zeta_1 = 1.0$, $\zeta_2 = 1.4$) and bilinearly tapered ($\eta_1 = 0.8$, $\eta_2 = 0$) screw. Force contributions are

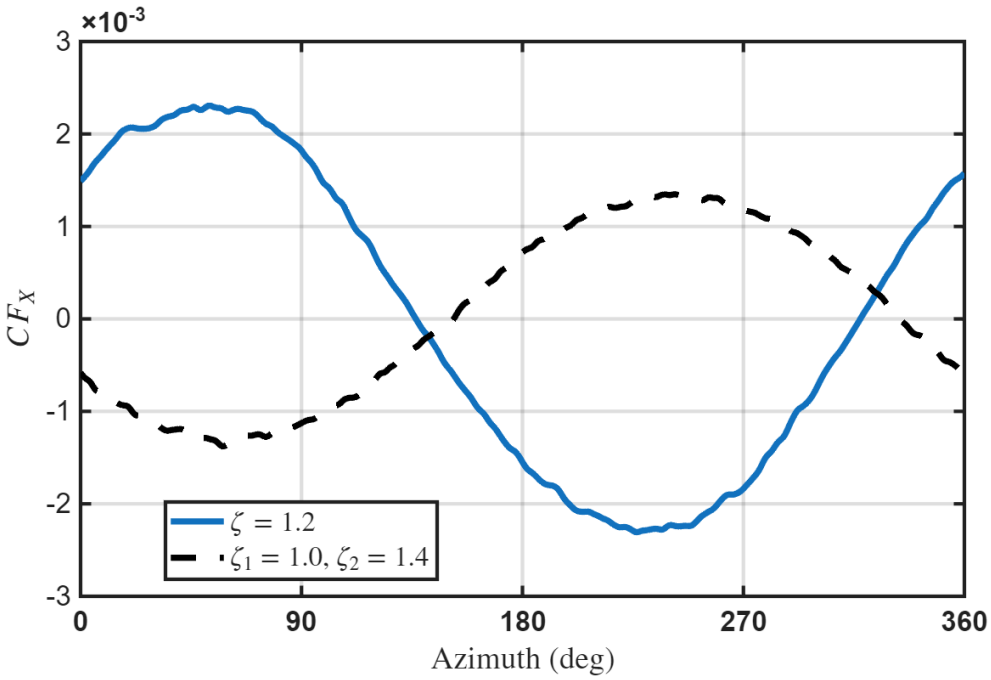

Figure 4.57: Nondimensional side force (CF_X) in hover comparing a $\zeta = 1.2$ linearly pitched screw and the bilinear screw

computed when the screw's leading edge is at an angle of azimuth of $\psi = 0$ degrees. The first half of the screw represents the blade from the leading edge to halfway down the screw and is denoted with the subscript, F_1. The second half of the screw represents the blade halfway down the screw to the trailing edge and is denoted with the subscript, F_2. A resultant force is defined at the net result of forces in x- and y-directions. Similarly this can be defined for the second half of the screw:

$$||F_{p1}|| = \sqrt{F_{p1X}^2 + F_{p1Y}^2} \tag{4.1}$$

$$||F_{f1}|| = \sqrt{F_{f1X}^2 + F_{f1Y}^2} \tag{4.2}$$

$$F_X = F_{p1X} + F_{f1X} + F_{p2X} + F_{f2X} \tag{4.3}$$

$$||F_s|| = \sqrt{F_X^2 + F_Y^2} \tag{4.4}$$

Phase shifting is not prominent in the z-direction and is not assessed here. F_{p1} describes the net resultant force due to pressure contributions for the first half of the screw as F_{p2} describes the same for the second half of the screw. F_{f1} describes the net resultant force due to viscous contributions for the first half of the screw as F_{f2} describes the same for the second half of the screw. The phase shifting due to pressure and viscous contributions is described as the phase offset between pressure and viscous forces in the y-direction over the pressure and viscous forces in the x-direction:

$$\theta_{pj} = \arctan(\frac{F_{pjY}}{F_{pjX}}) \tag{4.5}$$

$$\theta_{fj} = \arctan(\frac{F_{fjY}}{F_{fjX}}) \tag{4.6}$$

Both the linear and bilinear design variations are dominated by the pressure contributions in comparison to the viscous contributions. Comparing magnitudes, the pressure contributions are nearly two orders of magnitude larger than the viscous contributions for both the first and second half of the screw. Therefore, the phase shift seen in Figure 4.57 represents the side force peak lagging the leading edge by nearly 45 degrees. The bilinearly designed screw is out of phase in comparison to the linear screw due to the difference in pressure contributions from the first and

	Linear Screw	**Bilinear Screw**
$\frac{\|F_{p1}\|}{\|F_s\|}$	1.5532	2.2312
θ_{p1}	$-47°$	$-66°$
$\frac{\|F_{p2}\|}{\|F_s\|}$	1.7066	2.8534
θ_{p2}	$99°$	$126°$
$\frac{\|F_{f1}\|}{\|F_s\|}$	0.0771	0.185
θ_{f1}	$117°$	$97°$
$\frac{\|F_{f2}\|}{\|F_s\|}$	0.2242	0.3415
θ_{f2}	$-66°$	$-56.6°$

Table 4.1: Normalized force magnitudes and phase angles for Linear and Bilinear models

second halves of the screw. Both halves of the bilinear design result in larger magnitudes with different phases due to the normal vector geometry, creating the phase shifting.

4.6 Comparison of Best Performing Aerial Screws

The best performing screw designs from linear and bilinear combinations of screw pitch and taper are considered for comparison with a conventional rotor, for both aerodynamic performance and aeroacoustic signature. The geometric distribution of the pitch and taper rates (ζ_1, ζ_2, η_1, η_2) corresponding to the first and second half of the screw surfaces for each of these geometries are in Table 4.2

ID	Description	ζ_1	ζ_2	η_1	η_2
S1	Linear pitch and taper	1.2	1.2	0.5	0.5
S2	Bilinear pitch	1.0	1.4	0.5	0.5
S3	Bilinear taper	1.2	1.2	0.8	0.0
S4	Bilinear pitch and taper	1.0	1.4	0.8	0.0

Table 4.2: Different Aerial Screw Geometry Definitions

The comparison is made at a constant dimensional thrust generated by each of these rotors, which is chosen to match that of screw S1 (best linearly pitched and tapered screw), operating at a tip Mach number of 0.25. The size of all the screws is maintained the same as 1 ft in radius ($R_{\max}$), and the RPMs of the screws S2, S3 and S4 are adjusted to achieve the same target thrust. Table 4.3 shows the operating tip Mach numbers of the different screws and their corresponding figures of merit.

Figure 4.58 shows the normal pressure load coefficient (difference between surface pressures across the top and bottom surface) for screws S1, S2, S3 and S4. Compared to S1, S2 has a lower pitch rate near the leading edge region, resulting in a weaker *da Vinci vortex*. However, this region has smaller axial contributions and larger torque-wise contributions, which favors low power characteristics of S2. The loss in thrust is compensated by the second half region of the screw with aggressive pitch rate.

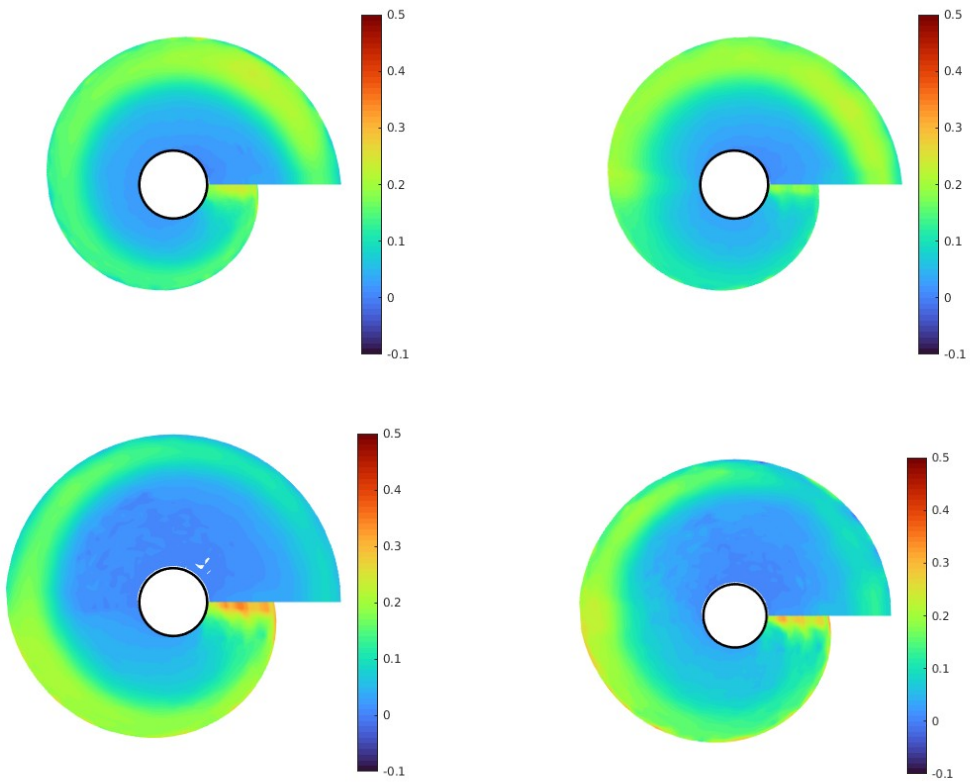

Figure 4.58: Surface Pressure Difference (ΔC_P) across Top and Bottom Surfaces for Screws S1 (top left), S2 (top right), S3 (bottom left) and S4 (bottom right)

For the screw S3, the second half region of the screw is untapered, resulting in less strengthening of the *da Vinci vortex* in this region. This is compensated by an aggressive taper in the first half compared to S1, resulting in improved performance. Screw S4 combines both the variations in pitch and taper profiles, resulting in a much favorable load distribution and improved performance.

4.6.1 Geometry of the Conventional Rotor

As mentioned in the introduction to this chapter, two notional conventional rotors are designed, one with 2 blades and the other with 4 blades. Both rotors have rectangular planforms, with a uniform twist rate of 20° from root to tip, and Clark-Y airfoil throughout the cross section.

The choice of the airfoil is made based on the operating Reynolds number. The collective of the blade is adjusted to achieve an optimal figure of merit. The solidity of each of the rotors is maintained at 0.16.

Since the aerial screws are of extremely high solidity, conventional rotors can not achieve the same thrust at same size and tip speed. Two versions of the conventional rotors are investigated, viz., one with same rotor size but trimmed with RPM and the other with same tip speed but of a larger size.

Table 4.3 shows the operating conditions for the different rotors at matched thrust, and a comparison of the figures of merit for these conditions. The tip speed and rotor size are given relative to Screw 1, and the FM is absolute.

All the conventional rotors we observed to achieve a higher FM compared to aerial screws. Among the conventional ones, the rotors with 4 blades show better performance than those with 2 blades. Also, the larger rotors at smaller RPMs have slightly better performance than smaller rotors with higher tip speeds.

ID	Description	Tip Speed $(M_{\text{tip}}/M_{\text{tip,S1}})$	Rotor Size $(R_{\text{max}}/R_{\text{max,S1}})$	FM
S1	Screw 1 (Linear Pitch and Linear Taper)	1.000	1.000	0.561
S2	Screw 2 (Bilinear Pitch and Linear Taper)	0.981	1.000	0.567
S3	Screw 3 (Linear Pitch and Bilinear Taper)	0.937	1.000	0.591
S4	Screw 4 (Bilinear Pitch and Bilinear Taper)	0.878	1.000	0.640
C2.1	Conventional Rotor (2 blades, Size matched)	1.240	1.000	0.726
C2.2	Conventional Rotor (2 blades, Tip Speed matched)	1.000	1.240	0.731
C4.1	Conventional Rotor (4 blades, Size matched)	1.160	1.000	0.769
C4.2	Conventional Rotor (4 blades, Tip Speed matched)	1.000	1.160	0.771

Table 4.3: Comparison of the Operating Speeds, Rotor Sizes and Figures of Merit for Different Aerial Screws and Conventional Rotors

4.6.2 Investigation of Rotor Wake and Induced Velocities in Hover

The best performing screw designs (S1, S2, S3 and S4) are investigated to understand the effect of vortex-based thrust on the induced velocity and wake behavior. Since the thrust generation is distributed across the length of the aerial screw, the wake behavior is different from the conventional rotor and understanding the induced velocity and wake contraction becomes important to further improve the screw performance.

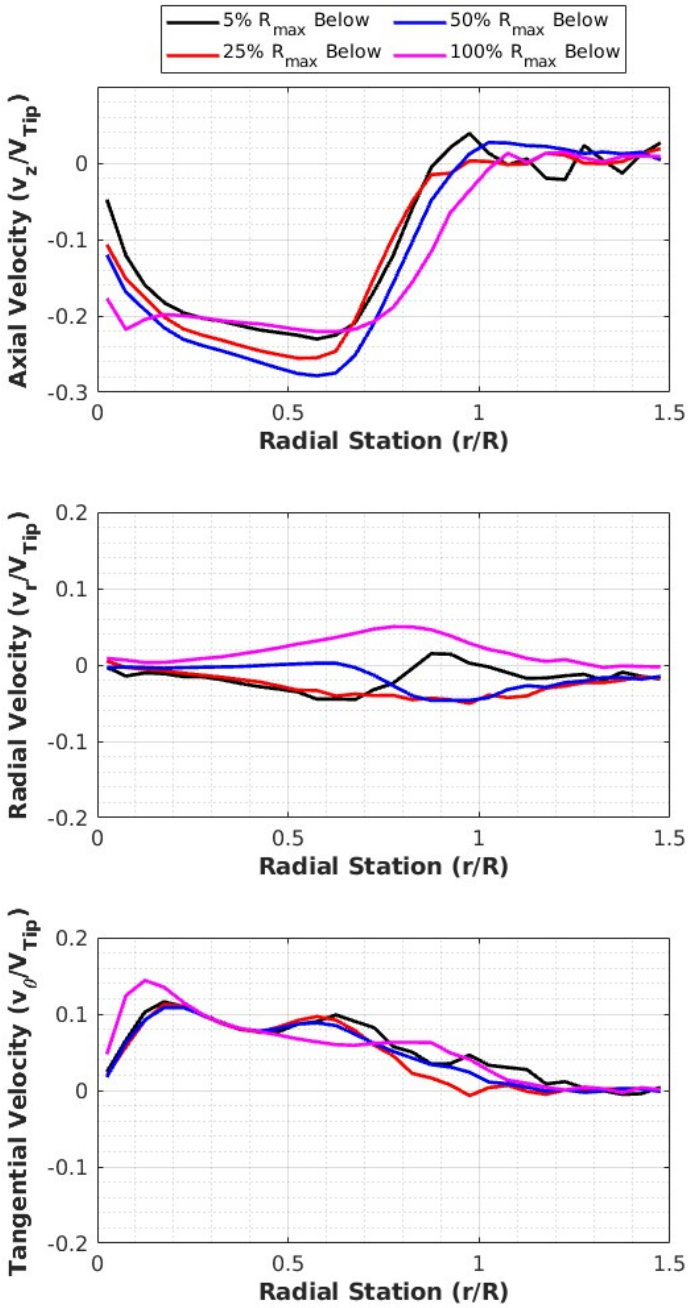

Figure 4.59: Azimuthal Average Wake Velocity Profiles for the Screw S1: Top: Axial Velocity; Middle: Radial Velocity; Bottom: Swirl Velocity

Azimuthal averaged velocity fields are investigated on planes parallel to the rotor plane, at different axial locations below the screw, viz., 5%, 25%, 50% and 100% $R_{\max}$ from the

trailing edge of the rotor blades. Figure 4.59 displays the variation of axial, radial and tangential components of the averaged velocities with radial distance, for screw S1. The velocities are normalized with rotor tip speed, and the radial distances with rotor radius.

It is observed that the wake contracts from $5\%\ R_{\max}$ to $50\%\ R_{\max}$, and then expands beyond. This is a non-ideal contraction of the wake, which is an indication of loss of flow energy to swirl or radial components and thereby lowering the figure of merit.

Radial velocity plot displays inward velocity profiles for wake-ages upto $50\%\ R_{\max}$, indicating desirable wake contraction trends. At $100\%\ R_{\max}$ station, the profile is radially outward, indicating a wake expansion in the region. The swirl velocity remains similar along the axis, and is significant in the inboard regions.

Figures 4.60, 4.61, and 4.62 show the instantaneous snapshot of wake profiles $50\%\ R_{\max}$ below the trailing edge, for screw S4. The coordinate axes are normalized with rotor radius and the wake velocities with rotor tip speed. The axial velocity profile shows nearly uniform downwash region, with a small instantaneous upwash region corresponding to the local vortex induced flow.

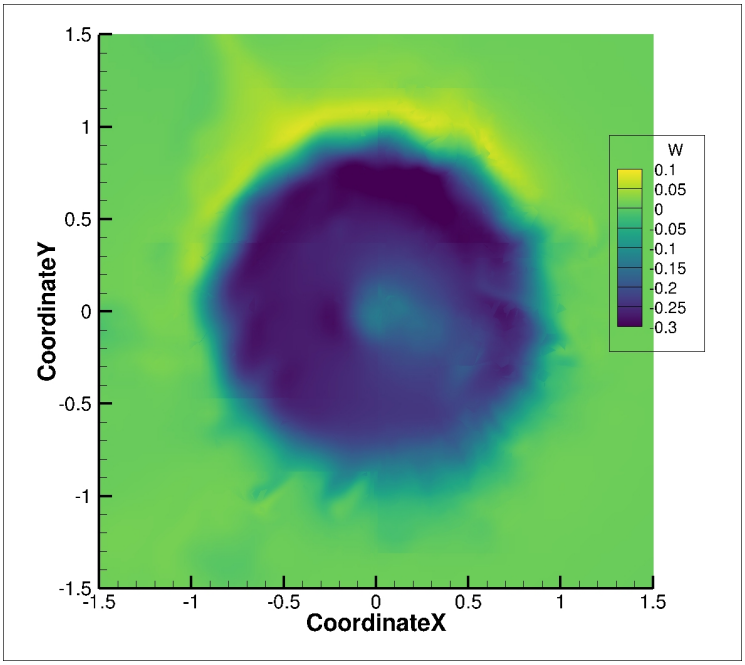

Figure 4.60: Instantaneous Axial Wake Velocity Profile for Screw S4 at an Axial Location 50% Below Trailing Edge

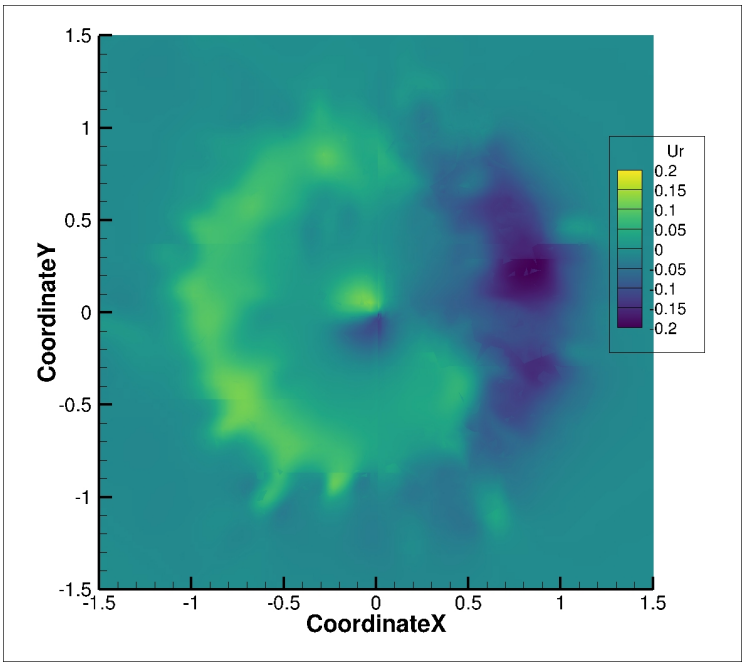

Figure 4.61: Instantaneous Radial Wake Velocity Profile for Screw S4 at an Axial Location 50% Below Trailing Edge

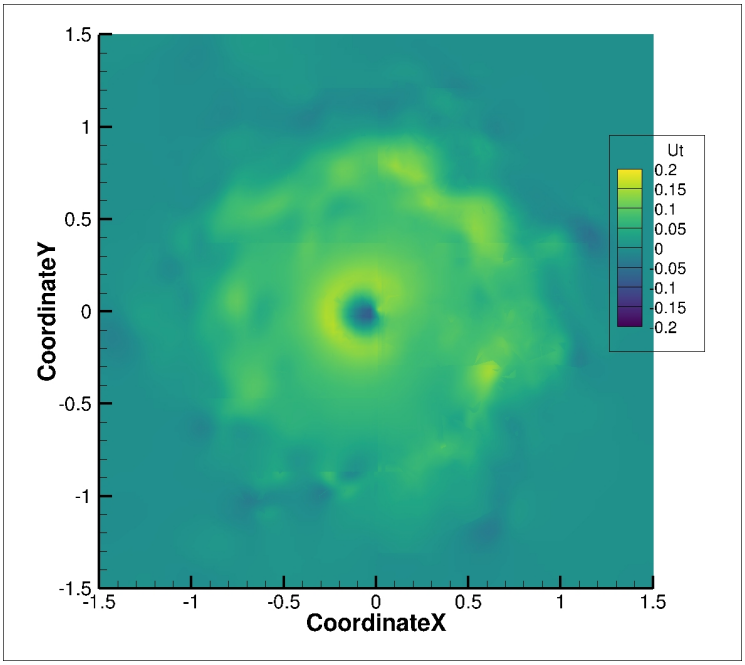

Figure 4.62: Instantaneous Swirl Wake Velocity Profile for Screw S4 at an Axial Location 50% Below Trailing Edge

One interesting observation in the radial velocity profile shows the effect of a single blade asymmetry resulting in radially outward flow in one region due to the presence of da Vinci vortex in the vicinity and a radially inward flow near the diametrically opposite region. Due to the helical nature of the blade, the influence of diametrically opposite points is dissimilar, resulting in a wake geometry that drifts from center. This effect is purely due to single bladed rotors, and can be seen in Figure 4.63.

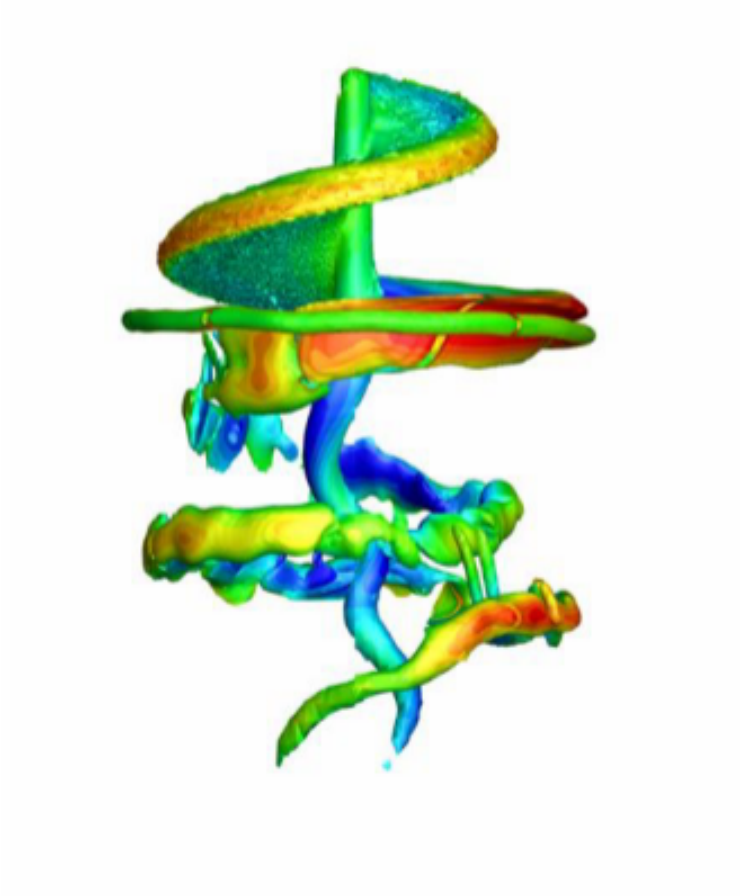

Figure 4.63: Instantaneous Wake Vorticity Iso-contours showing Asymmetry and Wake Drifting

Figure 4.64 shows the comparison of azimuthal averaged wake profiles for different screws. All the screws display a similar wake geometry, with screw S4 showing a complete wake contraction by the axial station $50\%\ R_{\max}$. The interior region of the wake is more uniform for the screw S4, as indicated by a flat radial velocity profile with minor contraction zone in the outboard region. This indicates more ideal wake contraction, as is observed in the high FM of S4. Screws S1, S2 and S3 require larger wake-age to achieve complete contraction, indicating higher losses of axial momentum to swirl.

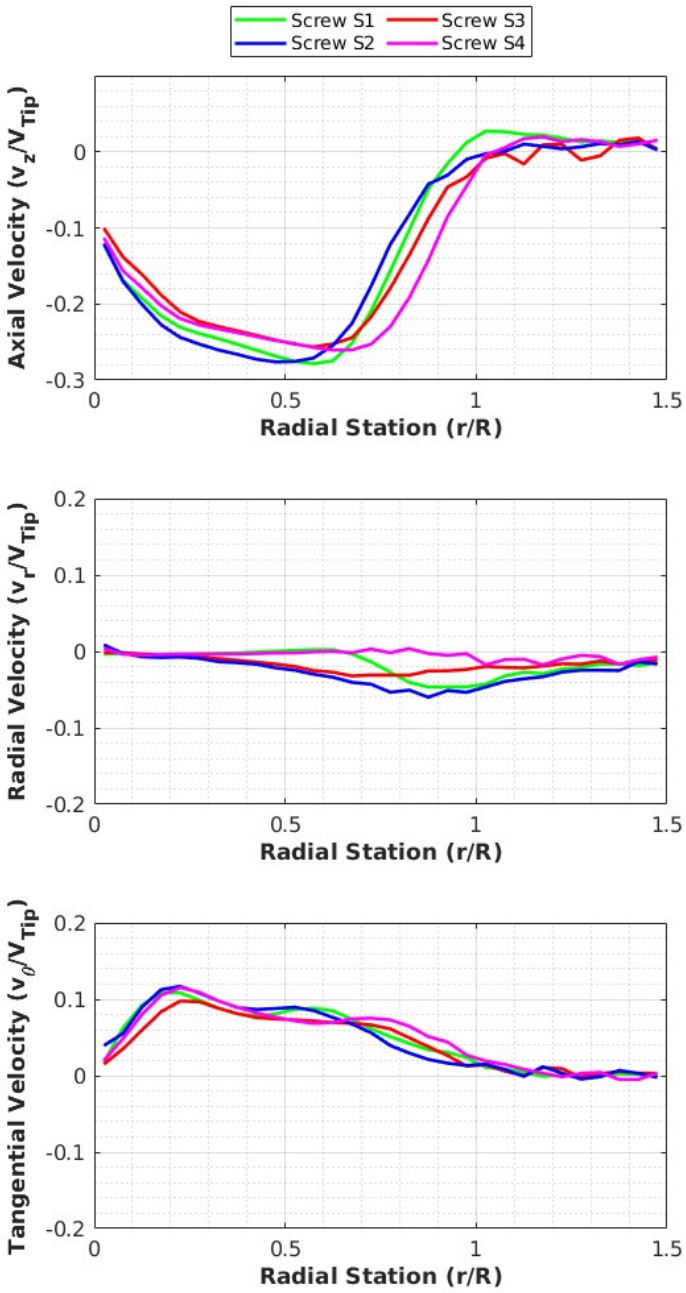

Figure 4.64: Azimuthal Average Wake Velocity Profiles for Different Screws at 50% $R_{\max}$ Axial Station: Top: Axial Velocity; Middle: Radial Velocity; Bottom: Swirl Velocity

The wake analysis in this study provides valuable insights that translate directly into aerial screw design strategies. Among the configurations studied, the bilinear pitch and taper screw

exhibited the most desirable wake characteristics, with complete contraction observed within 50% $R_{\max}$ below the rotor. This early and coherent wake contraction is indicative of efficient momentum transfer and reduced energy loss to non-thrust-contributing components such as swirl and radial outflow. In contrast, linearly pitched and tapered screws exhibited slower contraction and more diffused wake structures, corresponding to a measurable drop in figure of merit. These observations suggest that carefully tuning the azimuthal variation of pitch and taper is critical for optimizing the screw's aerodynamic performance. An aggressive initial taper promotes early *da Vinci vortex* formation, strengthening thrust generation, while a more gradual taper downstream supports sustained vortex coherence. Similarly, a bilinear pitch profile can improve the projection of surface pressure forces in the axial direction, thereby minimizing swirl-induced losses. The wake profile, therefore, serves not merely as a diagnostic outcome but as a key design tool—enabling identification of flow behaviors that directly impact efficiency. By targeting early vortex anchoring, reducing swirl, and promoting inward radial flow near the root, future aerial screw designs can be better tailored to exploit the vortex-based thrust mechanism central to their operation.

4.6.3 Performance Comparison of Screw S4 to Conventional Rotor in Axial and Off-Axis Flight

In this section, the one bladed bilinearly pitched and bilinearly tapered aerial screw (Screw S4) which achieves a $FM = 0.65$ in hover at 4000 RPM is compared to a two bladed conventional rotor in axial and off-axis flows. The conventional rotor's collective is set to achieve an optimal figure of merit in hover. The size of the rotors are identical and the tip speed of the rotor is increased to thrust match the bilinear varying aerial screw.

The bilinear pitch - bilinear taper aerial screw and conventional rotor are compared at three different axial flow states: $\lambda_c = 0.0$ (hover), $\lambda_c = 0.04$, $\lambda_c = 0.08$.

Figure 4.65 shows the variation in thrust and power coefficients among the bilinear aerial screw and conventional rotor as the climb inflow increases from hover. The bilinear aerial screw has a significantly larger thrust coefficient than the conventional rotor, verifying the reason for the increased tip speed of the conventional rotor to thrust match. The thrust coefficient drops 57% from hovering flight ($\lambda_c = 0.0$) to the higher axial climb state ($\lambda_c = 0.08$) for the bilinear screw. Similarly for the bilinear design, the power coefficient drops 40%. For the conventional rotor, the climb rate does not negatively effect C_T and C_P in a similar fashion to the bilinear screw. The thrust coefficient drops 26% from hover and the power coefficient drops 4% from hover, causing the increase in FM^* with increasing λ_c.

Figure 4.66 shows the variation in the efficiency of the bilinear aerial screw and conventional rotor as the climb inflow increases in hover. By definition, the bilinear aerial screw has an effective $\zeta = 1.2$ pitch rate, with the first half of the screw being $\zeta = 1.0$ and the second half, $\zeta = 1.4$. As seen in Figure 4.18, lower pitch rates show drops in efficiencies as the climb inflow increases. Due to the significant drop in thrust as the climb inflow increases, FM^* decreases from 0.65 in hover to 0.58 when $\lambda_c = 0.08$. For the conventional rotor, an increase in FM^* from 0.77 in hover to 0.81 ($\lambda_c = 0.08$) is seen as the thrust coefficient is not significantly affected by the increasing climb inflow.

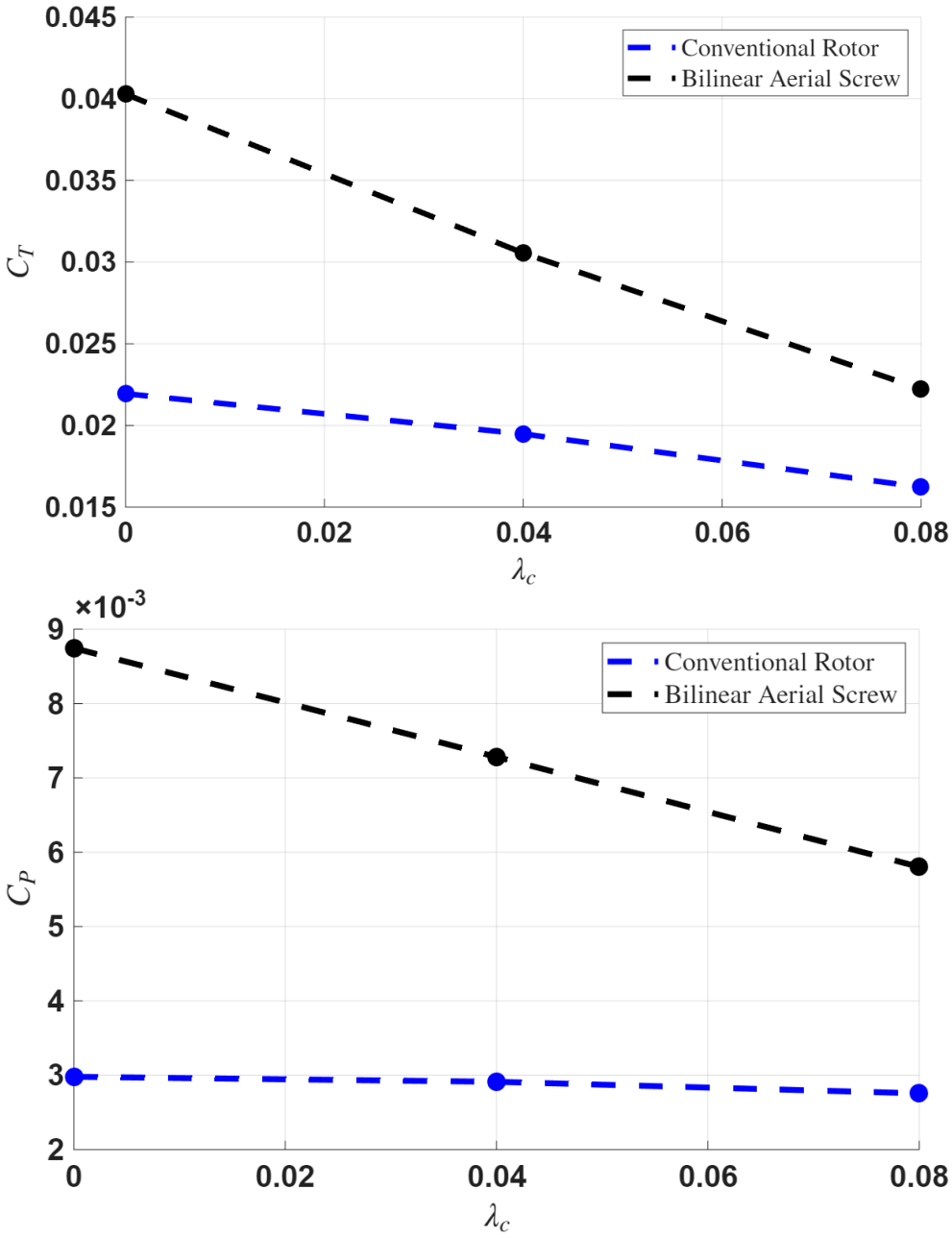

Figure 4.65: Variation of C_T and C_P with axial climb speed for the bilinear screw and conventional rotor

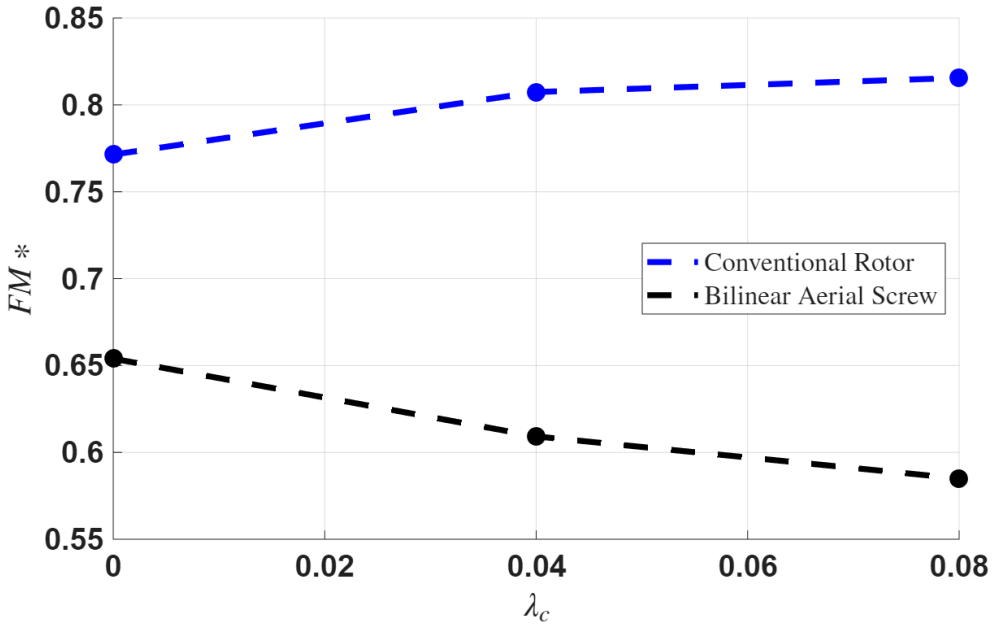

Figure 4.66: Variation of FM^* with axial climb speed for the bilinear screw and conventional rotor

To compare off-axis flight, the bilinearly pitched and tapered aerial screw and conventional rotor are investigated at a matching $\lambda = 0.08$ additional inflow to their respective hover inflows, with 5 degrees off-axis flow from axial climb. Due to the increased tip speed of the conventional rotor, the total additional inflow for the conventional rotor is higher than that of the aerial screw's. Figure 4.67 shows an enlarged view of the propulsive force coefficient as a function of the azimuth before comparison to the bilinear aerial screw. The frequency of oscillation in CF_X is 2/rev, consistent with the number of blades of the conventional rotor. Peaks in CF_X occur when one blade reaches its maximum M_{tip} value over the periodic motion, aligned at $\psi = 90$ degrees.

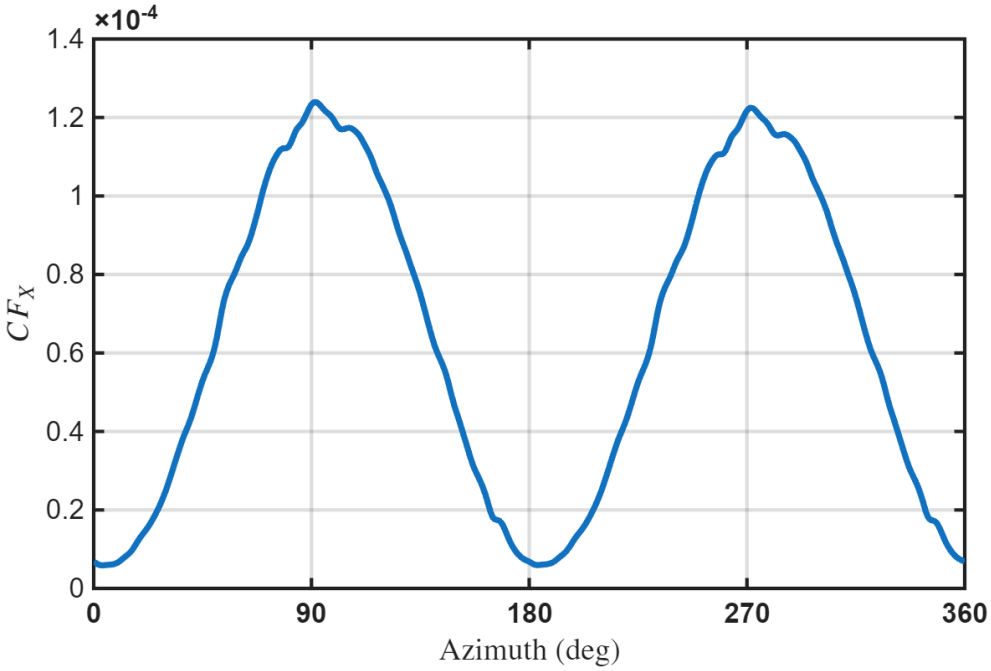

Figure 4.67: Conventional rotor propulsive force coefficient (CF_X) as a function of the azimuth in off-axis flight

Comparing the bilinear aerial screw to the conventional rotor in off-axis flight, the aerial screw has significantly amplified oscillations in CF_X, CM_X, CF_Y and CM_Y as seen in Figures 4.68, 4.69, 4.71, and 4.72. For the propulsive force, the peaks in CF_X have a 174% difference. The percentage difference in the rolling moment, CM_X is similar to that for CF_X. For the side force, the peaks in CF_Y have a 182% difference. The percentage difference in the rolling moment, CM_Y is similar to that for CF_Y. There is a significant variation in the loads along the surface of the screw for a one bladed rotor. This effect is mitigated for the conventional rotor with $N_b = 2$. The 1/rev and 2/rev behaviors for the aerial screw and conventional rotor respectively are not evident in CF_Z and CM_Z. The average lift coefficient of the aerial screw is $CF_Z = 0.022$, 31% higher than that for the conventional rotor of $CF_Z = 0.016$. With the increase in lift, the aerial screw sees an increase in the torque compared to the conventional rotor as well.

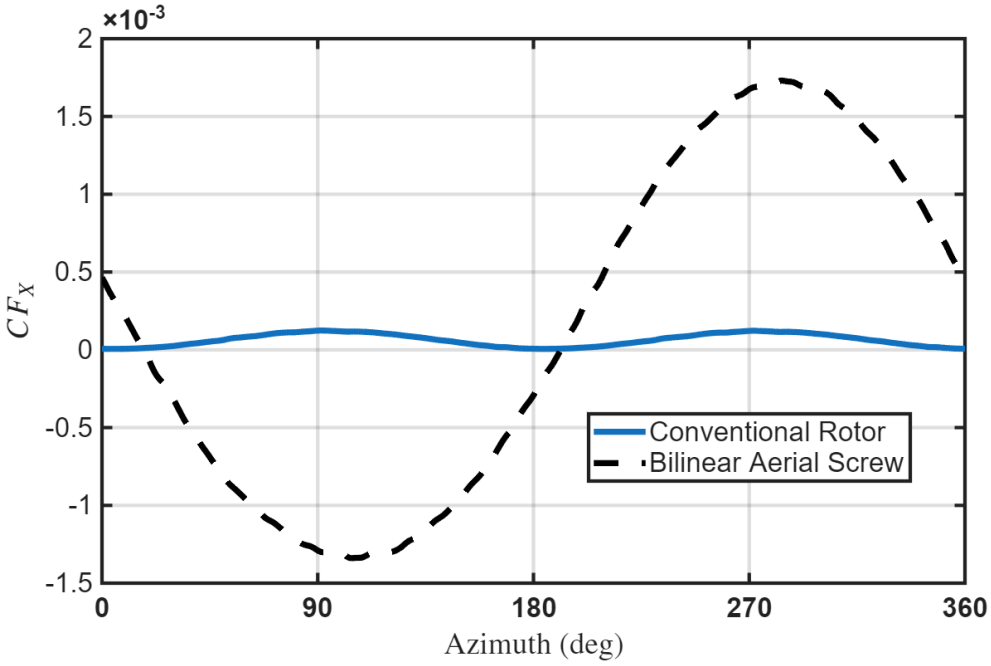

Figure 4.68: CF_X as a function of azimuth for comparison to a conventional rotor

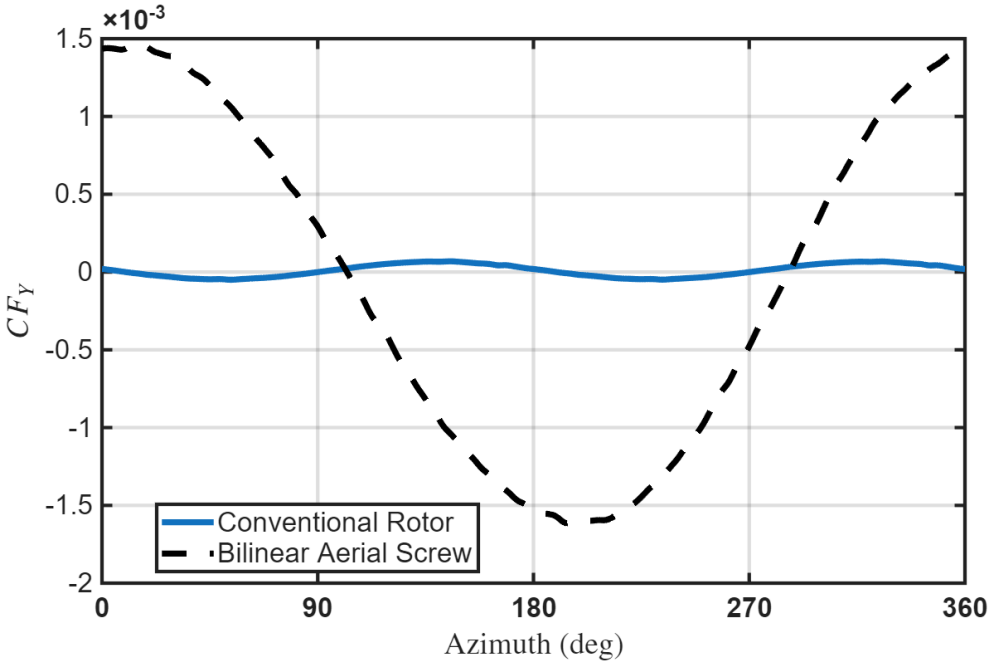

Figure 4.69: CF_Y as a function of azimuth for comparison to a conventional rotor

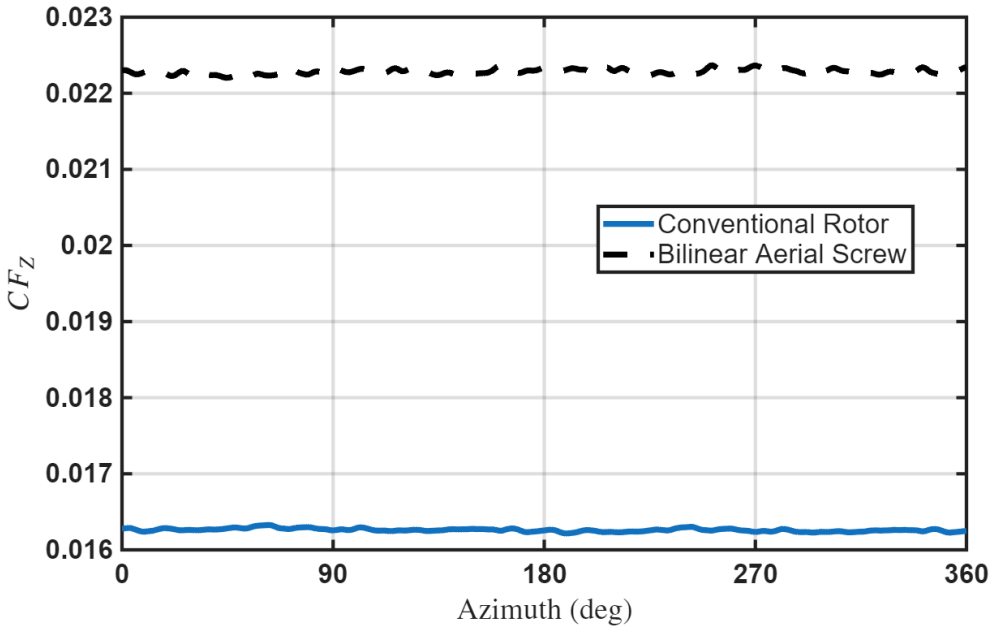

Figure 4.70: CF_Z as a function of azimuth for comparison to a conventional rotor

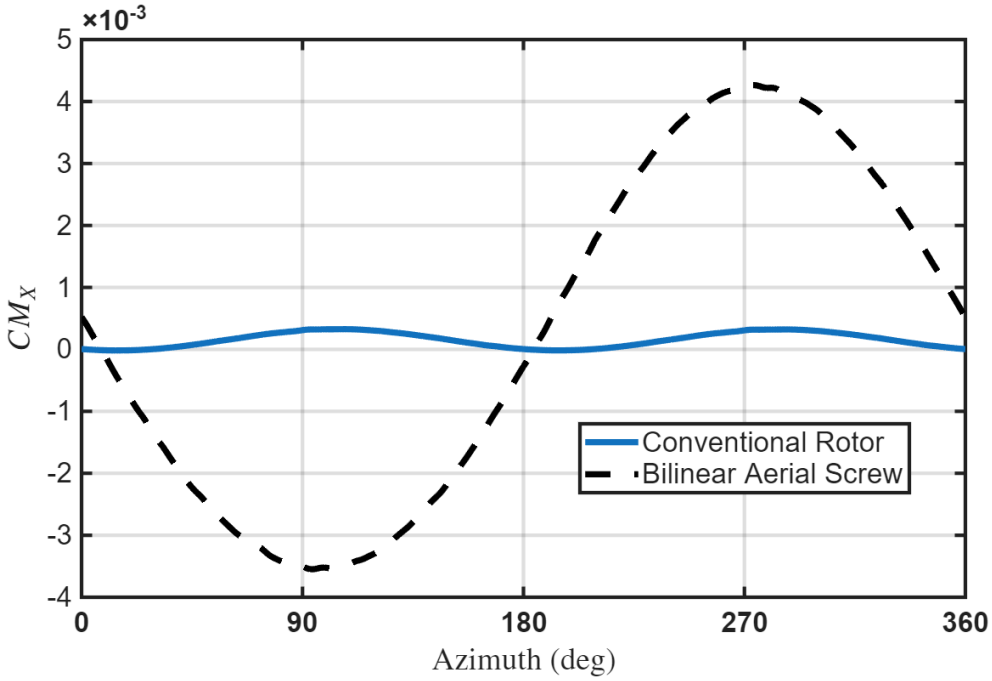

Figure 4.71: CM_X coefficients as a function of azimuth for comparison to a conventional rotor

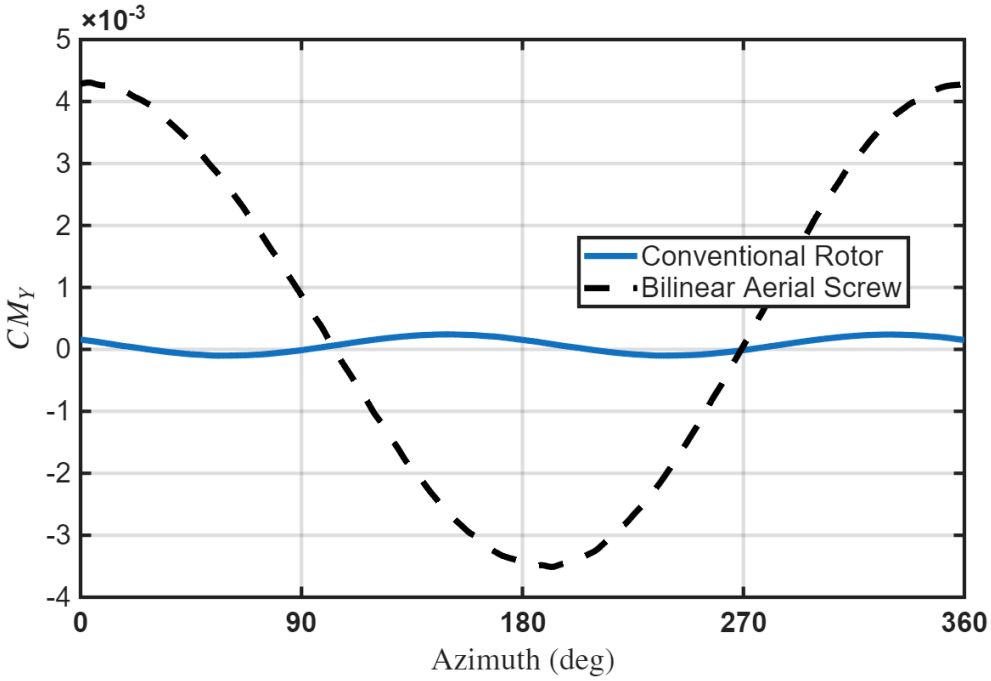

Figure 4.72: CM_Y coefficients as a function of azimuth for comparison to a conventional rotor

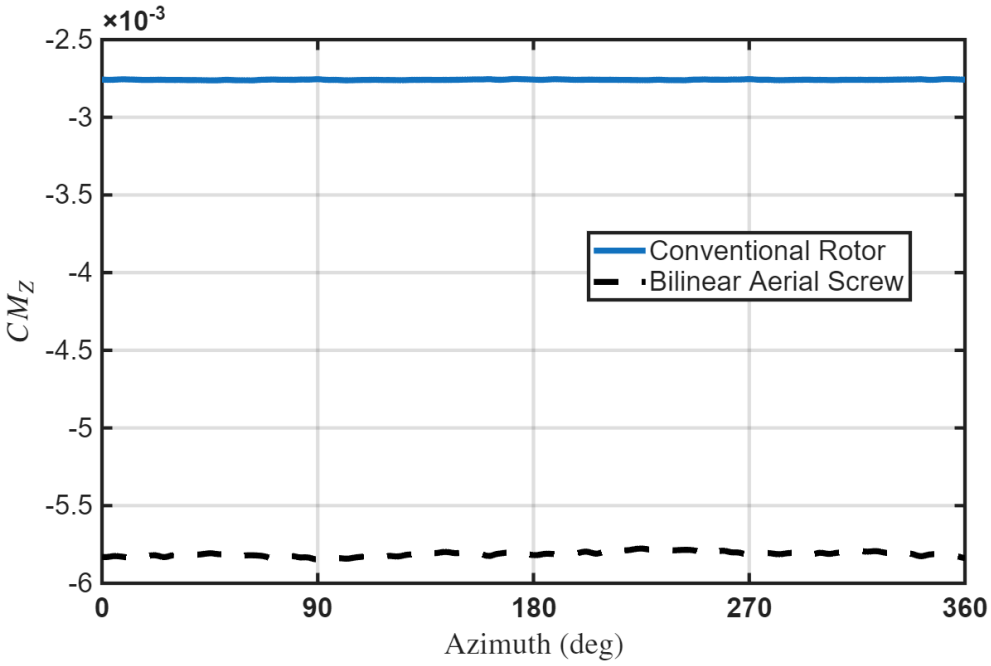

Figure 4.73: CM_Z coefficients as a function of azimuth for comparison to a conventional rotor

4.7 Chapter Summary

This chapter explored the effect of varying aerial screw parameters on the aerodynamics and performance of the unique rotor.

Through computational fluid dynamics (CFD) investigations, the primary thrust mechanism was found to be a shape-conforming vortex at the blade tip - the da Vinci vortex - which functions analogous to vortex lift on delta wings. Inboard sections of the screw were found to contribute little to the rotor's overall thrust generation.

The maximum radius (R_{max}) was found to contribute to increases in the figure of merit as R_{max} increases, with diminishing returns at larger radii. Larger screws operating at larger Reynolds numbers resulted in less dominant viscous effects, contributing to the increase in efficiency.

An increasing number of blades (N_b) was found to significantly decrease the figure of merit of aerial screws for similar pitch and taper rate due to interactional aerodynamics weakening the da Vinci vortex and pushing it inboard.

The effect of linear pitch rate was discussed in depth in this chapter in hover, axial climb, and off-axis climb states. A near optimal linear pitch rate exists at $\zeta = 1.2$, balancing vortex strength against the torque-wise orientation of the blade's surface normal in hover. Beyond this point, aggressive pitch generates a stronger vortex but at a disproportionately higher power cost. The optimal pitch rate shifts upward with increasing climb speed — from $\zeta = 1.2$ in hover, to $\zeta = 1.4$ at $\lambda_c = 0.04$, to $\zeta = 1.8$ at $\lambda_c = 0.08$. Higher pitch rates better sustain the effective angle of attack with increasing climb inflow. Higher pitch rates produced significantly larger oscillatory loads in off-axis flight. There is a 115% difference in the lift coefficient between the $\zeta = 2.0$ and

$\zeta = 1.0$ designs, but this comes with substantially amplified side forces and pitching/rolling moments.

Bilinear variations of pitch rate were investigated with a fixed linear taper rate of $\eta = 0.5$ in hover. It was found that a pitch rate transition from $\zeta_1 = 1.0$ to $\zeta_2 = 1.4$, an effective $\zeta = 1.2$, yielded the highest efficiency in hover with $FM = 0.567$. This pitch variation keeps torque-wise loads low in the first half of the screw while achieving a strong vortex in the second half the screw.

The effect of linear taper rate was discussed in depth in this chapter in hover, axial climb, and off-axis climb states. Performance decreases monotonically beyond $\eta = 0.5$, as the gain in da Vinci vortex strength from aggressive taper is outweighed by the loss of effective lifting area in hover. The influence of taper rate diminishes sharply as climb speed increases. At $\lambda_c = 0.08$, the difference in FM^* between the $\eta = 0.5$ and $\eta = 0.66$ designs collapses to just 0.15%, with pitch rate becoming the dominant parameter. Taper rate variation produces significantly smaller force and moment oscillations than pitch rate variation in off-axis flight, further confirming pitch rate as the dominant design parameter in axial and off-axis climbs.

Bilinear variations of taper rate were investigated with a fixed linear pitch rate of $\zeta = 1.3$ in hover. Bilinear taper rates were applied such that the first half of the screw had an aggressive taper while the second half of the screw was left untapered. Aggressively tapering the first half to $\eta = 0.8$ achieved $FM = 0.59$, a 5% improvement from the best linearly tapered design. The first half of the screw strongly feeds the da Vinci vortex. The untapered second half results in the vortex slightly detaching off of the screw's surface but the increase in lifting area contributes to higher thrust values for reasonable power consumption, increasing the figure of merit.

The best bilinear variations of pitch and taper were combined to create a bilinearly pitched

($\zeta_1 = 1.0$, $\zeta_2 = 1.4$) and bilinearly tapered ($\eta_1 = 0.8$, $\eta_2 = 0.0$) design. This combination resulted in $FM = 0.64$ in hover when $M_{tip} = 0.25$. This was a 13.7% improvement from the best linearly varying design in hover. The bilinear design's initial taper rate feeds the da Vinci vortex with sufficient lifting area in the second half of the blade, additionally leveraging efficient surface normal orientations in the first and second half of the screw. Azimuthal load comparisons between linear and bilinear screw variations reveal phase shifting caused by the difference in surface normal orientations in the bilinear case. This finding suggests an optimized one-bladed aerial screw could cancel or minimize side forces significantly.

A wake analysis of the best performing linear pitch -linear taper, bilinear pitch - linear taper, linear pitch - bilinear taper, and bilinear pitch - bilinear taper designs in hover was investigated. The bilinearly pitched and tapered design achieved the earliest and most complete wake contraction. This indicates more efficient axial momentum transfer and less energy lost to swirl, directly explaining the significant increase in the figure of merit.

Performance comparisons were created between the best performing aerial screws to conventional rotors. While the bilinearly pitched and tapered design outperforms all aerial screws, conventional rotors still achieve higher figures of merit ($FM \approx 0.73 - 0.77$ vs $FM = 0.64$). The conventional rotor increases in efficiency (FM^*) as the climb inflow increases while the bilinear - bilinear screw decreases in efficiency. In off-axis flight, the bilinear screw exhibits significantly larger peaks in side forces, rolling and pitching moments compared to the two-bladed conventional rotor.

Chapter 5: Aeroacoustic Analysis of Aerial Screws

The aeroacoustic analysis of the screws is performed using ACUM [11], the University of Maryland's in-house acoustic prediction toolchain. ACUM utilizes geometric and aerodynamic data from CFD simulations to compute thickness and loading noise components and predict sound pressure levels (SPL) at specified observer locations. The underlying computational framework is based on Farassat's Formulation 1A [12] of the Ffowcs Williams–Hawkings (FW-H) equation [13], which models both the thickness and loading contributions to tonal noise.

The acoustic signatures of various screw designs (S1, S2, S3, and S4) are compared against those of conventional rotors (C2.1, C2.2, C4.1, and C4.2) in hover from Table 4.3. Observers are placed along a circular arc in a plane perpendicular to the rotor axis at a radial distance of 5 meters from the rotor center. For screws S1–S4 and rotors C2.1 and C4.1, this corresponds to approximately 16.5 rotor radii (R). Due to the larger diameters of C2.2 and C4.2, this observer distance represents a slightly smaller non-dimensional value for these rotors.

In this study, only the thickness and loading noise components are modeled using the FW-H formulation within ACUM. The self-noise components, typically modeled empirically, are excluded due to the lack of validated models for the unconventional screw geometries. For consistency, self-noise is also excluded from the conventional rotor predictions.

The input to the acoustic solver is derived from DDES simulations (using HAMSTR),

which provide both the steady blade loading and unsteady pressure fluctuations associated with blade–wake interaction (BWI). These components are used to compute the acoustic signature of each rotor configuration. For the aerial screws, the aerodynamic simulation is resolved every 0.5° for one full rotor revolution. For the conventional rotors with N_b blades, the flow solution is resolved every 0.5° for $1/N_b$ rotor revolutions. The aerodynamics data is replicated for a full rotor revolution using a periodic assumption with period $1/N_b$.

5.1 Thickness Noise

Figure 5.1 shows the variation of the thickness noise acoustic pressure for different observer locations on the circle, for all the rotors.

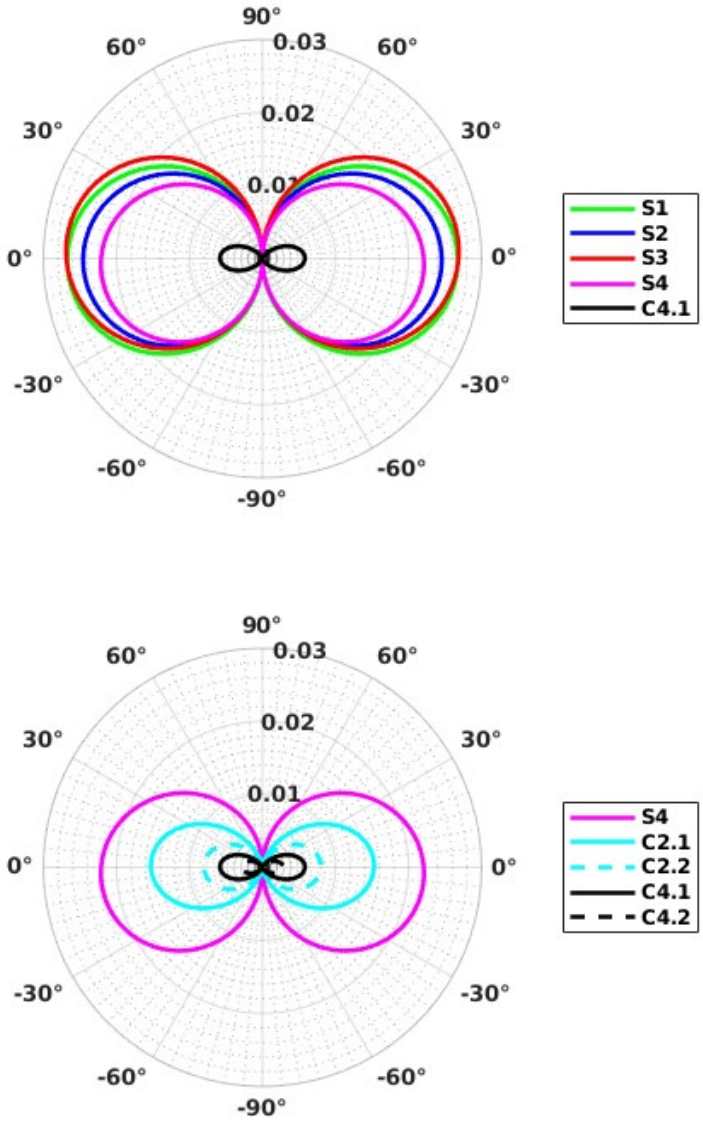

Figure 5.1: Directivity of Thickness Noise (p'_{rms} vs θ), Top: Screws S1, S2, S3 and S4 vs Conventional Rotor C4.1, Bottom: Screw S4 vs Conventional Rotors C2.1, C2.2, C4.1 and C4.2

The aerial screws, due to their distributed geometries, exhibit large thickness noise levels compared to conventional rotors. Similar to conventional rotors, the thickness noise due to aerial screws is dominant in-plane of the rotors and diminishes as the observer moves towards the rotor axis.

Conventional rotors operating at higher speed exhibited larger thickness noise levels compared to larger rotors at lower speeds. Also, the rotors with 4 blades have the least noise levels of all the conventional rotors and aerial screws.

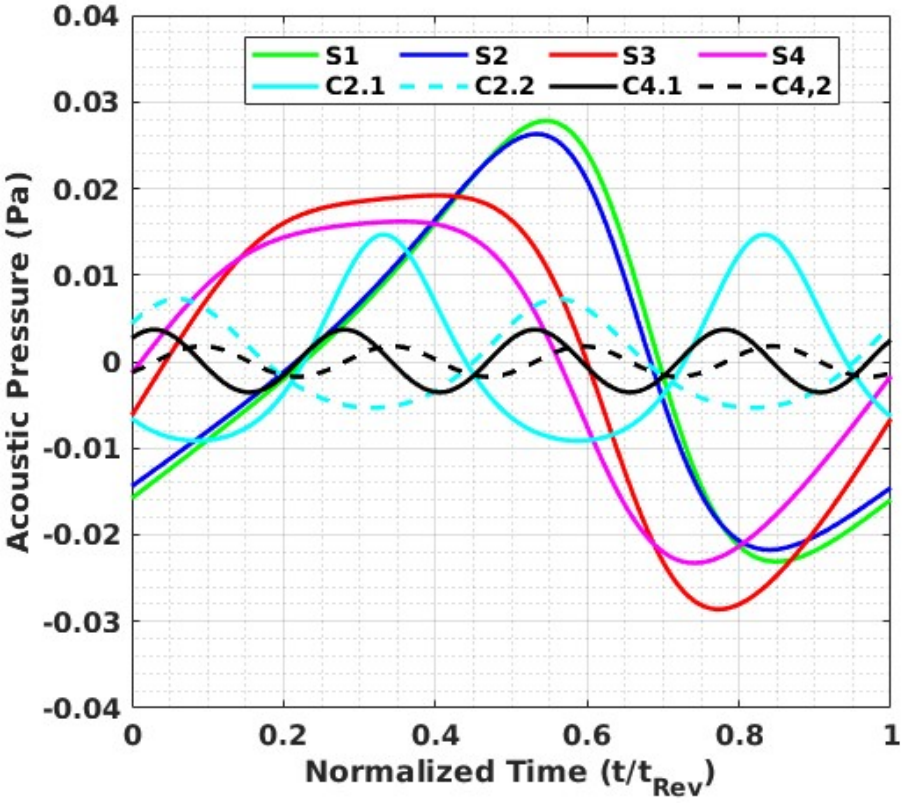

Figure 5.2: Thickness Noise Waveforms for Observer at $\theta = -30^\circ$ for different Rotors

Figure 5.2 shows the acoustic pressure waveforms at an observer located on the circle at 30° declination from the rotor plane. The peak-to-peak amplitudes of aerial screws are large compared to the conventional rotors, as predicted by the acoustic directivity chart. Due to the distributed geometry of the screws, the corresponding waveforms have a distributed frequency spectrum due to the interference pattern of axially distributed acoustic sources. Conventional rotors have dominant blade passage frequency components in the waveforms.

Screws S1 and S2 have similar acoustic waveform, and S3 and S4 have a similar waveform,

indicating that the thickness noise is more sensitive to screw taper distribution than pitch distribution.

While the noise levels of the conventional rotors are lower than the aerial screws, the corresponding blade passage tonal frequencies for screws are $1/\mathrm{Rev}$ and for the conventional rotors are N_b/Rev. With the frequency adjustments for perceived loudness using A-weighting [14], the perceived noise levels of aerial screws is lower than the conventional rotors.

5.2 Tonal Loading Noise (Steady Loads)

Figure 5.3 shows the variation of the acoustic pressure due to loading noise at different observer locations on the circle, for all the rotors. These estimates are based on the steady component of the loads (azimuthal invariants).

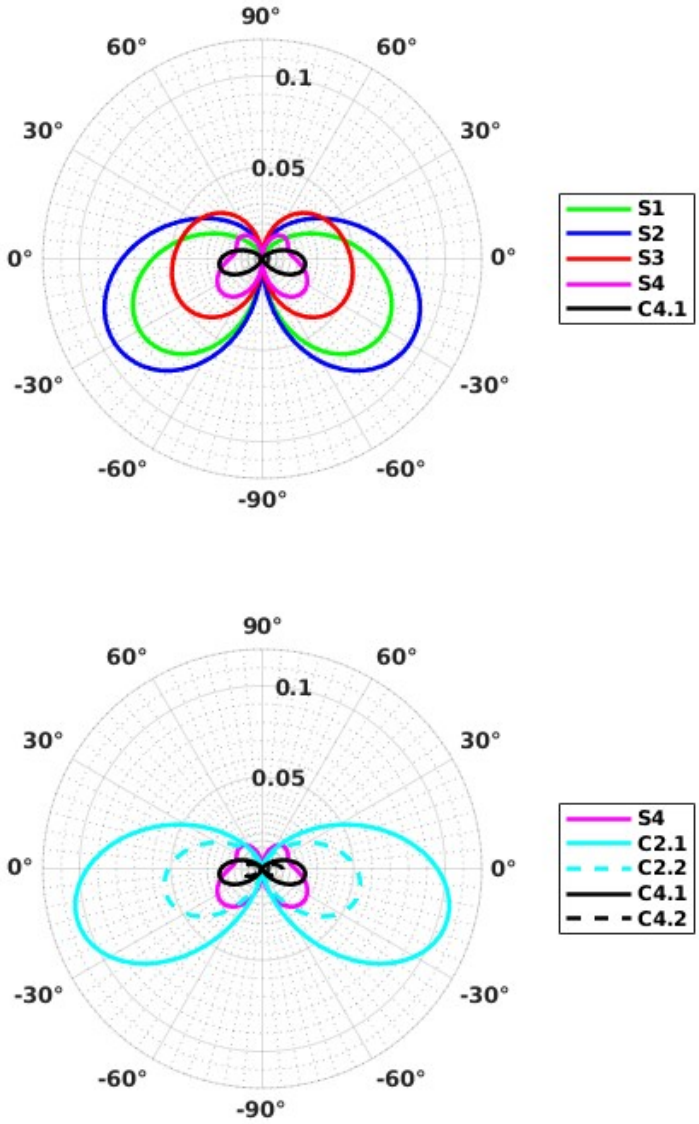

Figure 5.3: Directivity of Loading Noise due to Steady Loads (p'_{rms} vs θ), Top: Screws S1, S2, S3 and S4 vs Conventional Rotor C4.1, Bottom: Screw S4 vs Conventional Rotors C2.1, C2.2, C4.1 and C4.2

The loading noise levels are higher below the rotor plane compared to above, and diminish as the observer moves towards the rotor axis.

Conventional rotors with 2 blades exhibited the highest loading noise levels compared to

all other rotors. Rotor C4.1 and screw S4 show similar noise levels, lower than the other screw geometries. All the screws show maximum noise at a declination of $\sim 30^{\circ}$ from the rotor plane, and conventional rotors show a maximum noise level at $\sim 15^{\circ}$.

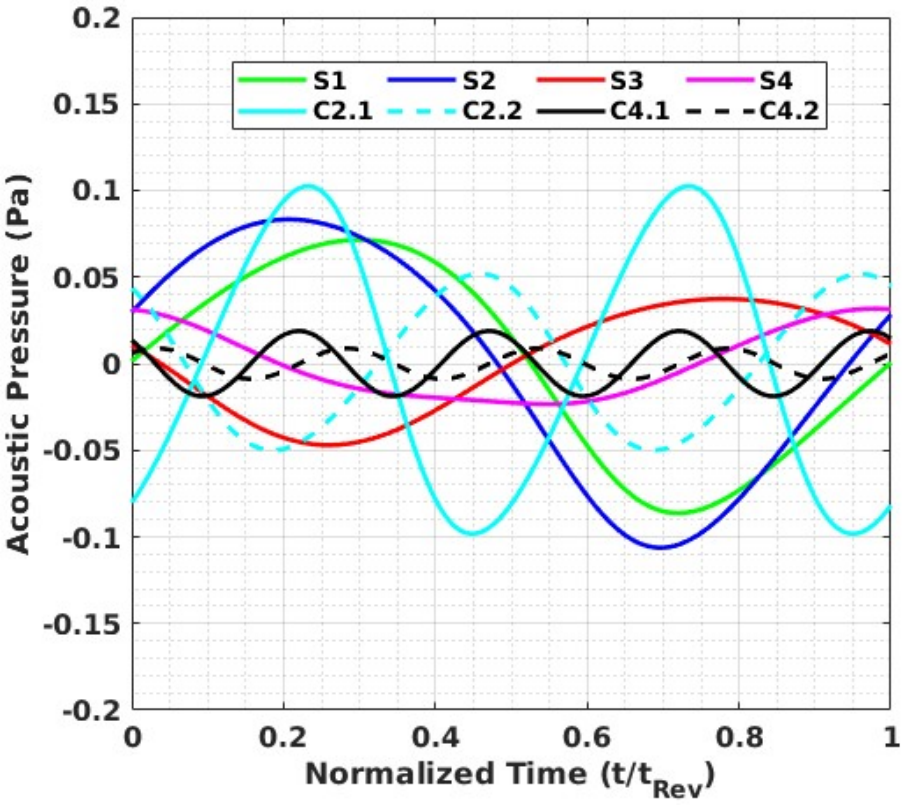

Figure 5.4: Loading Noise Waveforms (Steady Loads) for Observer at $\theta = -30^{\circ}$ for different Rotors

Figure 5.4 shows the acoustic waveforms corresponding to steady loading noise at the observer located at 30° declination to the rotor plane. The peak-to-peak magnitudes of the conventional rotor with 2 blades are highest, followed by the screws S1 and S2. The waveforms corresponding to aerial screws contain higher harmonics of the rotor frequency, due to the distributed nature of acoustic sources.

Similar to the thickness noise, the perceived noise level is lower for the aerial screws for

the steady loading component due to the differences in blade passing frequencies.

5.3 Loading Noise (Unsteady Loads)

DDES simulations are used to resolve larger turbulent structures in the flow, resulting in unsteady blade loads. These unsteady loads include the Blade-Wake interaction (BWI) component, resolved components of turbulence etc. These unsteady loads contribute to a broadband component of the loading noise. While the unsteady components are not periodic with rotor revolutions, the acoustic simulation is performed with the periodic assumptions. These assumptions result is minor inaccuracies to predict the acoustic content at non-multiples of the blade passage frequencies. However, major components of the broadband noise can be predicted using these unsteady loads.

Figure 5.5 shows the contours of root mean square (RMS) value of the fluctuations of surface pressure coefficient for the aerial screws S1, S2, S3 and S4, for upper and lower surfaces. These contours inform the locations of various acoustic sources corresponding to the unsteady loads on the rotors.

On the upper surface of the screw, the leading edge region contributes for the majority of unsteady aerodynamic loading, due to the presence of a LE vortex separation phenomenon. Also, the tip region around the da Vinci vortex also experiences unsteady pressures due to the unsteadiness of the vortex. The regions of pitch rate and taper rate transition in the screws S2, S3 and S4 are secondary zones of unsteadiness.

The lower surface of the screw contributes for the majority of unsteady loads for the aerial screws. These variations are larger towards the trailing edge of the screw, corresponding to the interaction of the screw surface with wake vorticity. The leading edge and tip region are

secondary zones of unsteadiness, caused by the tip leakage of the vortices.

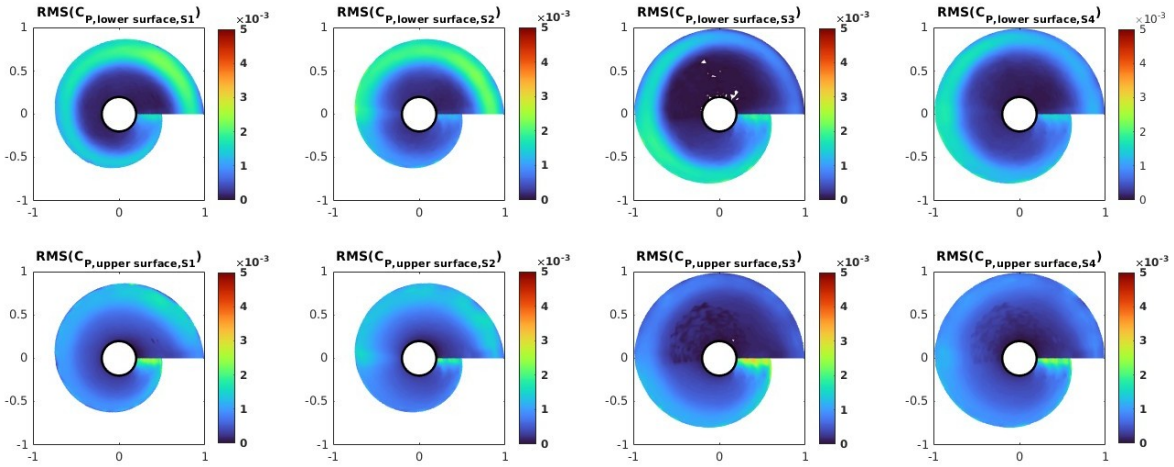

Figure 5.5: Contours of the RMS fluctuations of Surface Pressure Coefficient for Screws S1, S2, S3 and S4

These unsteady loads contribute additional noise components that span a wide range of frequencies. For the aerial screws, the interaction with wake is a continuous event distributed along the rotor revolution. This results in a less impulsive noise signature.

However, for conventional rotors, of all the unsteady components, the BWI events are highly impulsive. These events occur when a blade passes the trailing wake due to the other blades. Due to smaller chord of the conventional rotors and large blade loadings, the duration of the interaction is small and the strength of the interaction is large, resulting in an impulsive load fluctuation.

In case of the rotors C2.x and C4.x, the solidity of the rotors remain the same, and thus C2.x rotors have a wider chord compared to C4.x. Thus, the BWI loads are relatively less impulsive for the rotors with two blades compared to those with 4 blades.

These unsteady loads are used in the noise computations, and the resulting noise directivity is shown in Figure 5.6. While the conventional rotors show a significant noise level in the axial

direction, the aerial screws show a distinctive noise directivity concentrated towards $\sim \pm 15^{\circ}$ from the rotor axis. The unsteady loading noise is smaller for the rotors C2.1 and C2.2, maintaining the directivity pattern of these rotors same as steady loads at angles away from the rotor axis. The directivity pattern of C4.1 and C4.2 is significantly changed to be dominant along the rotor axis due to high impulsive unsteady loads.

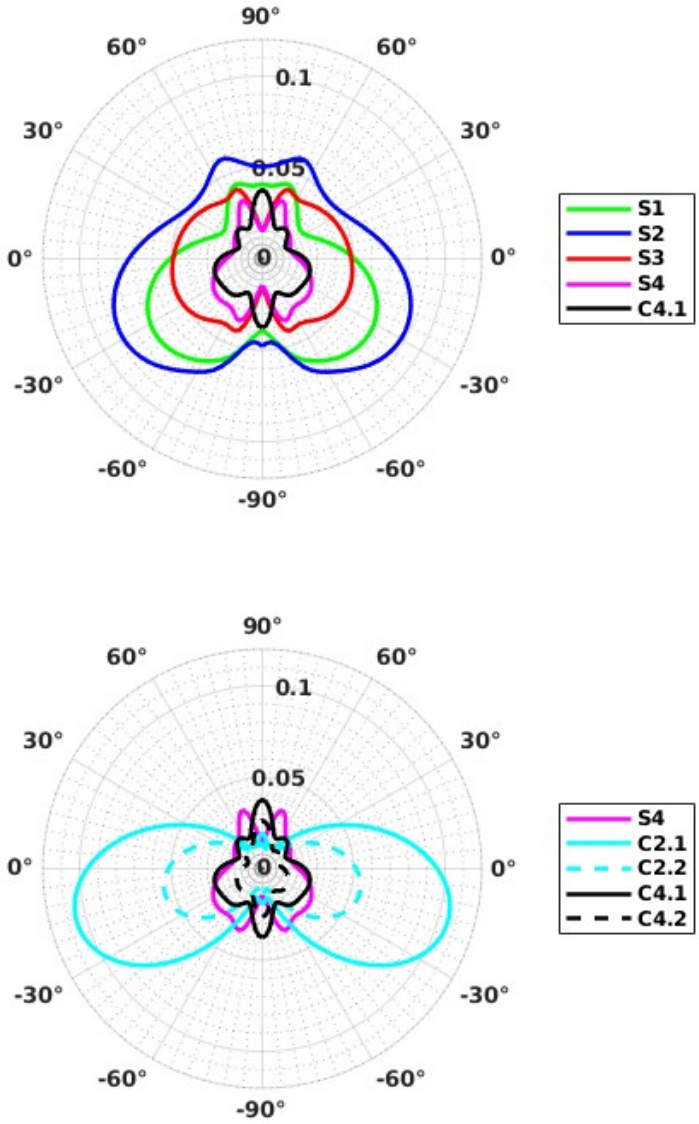

Figure 5.6: Directivity of Loading Noise due to Unsteady Loads (Steady and Blade Wake Interactions combined) (p'_{rms} vs θ), Top: Screws S1, S2, S3 and S4 vs Conventional Rotor C4.1, Bottom: Screw S4 vs Conventional Rotors C2.1, C2.2, C4.1 and C4.2

Figure 5.7 shows the comparison of loading noise waveforms received by observer located at 30° declination form the rotor plane, for the rotors S4, C2.1 and C4.1. With a unsteady acoustic sources distributed over the screw surface, the unsteady waveform of S4 has a wide range of

overtones with diminishing magnitude superposed on the tonal waveform. Rotor C2.1 shows minimal deviation from the steady waveform, with a few distributed impulses due to BWI events. The unsteady waveform of C4.1 shows large and sharp fluctuations due to the impulsive BWI events. These sharp fluctuations contain a wide range of overtones of the blade passage frequency with large magnitudes.

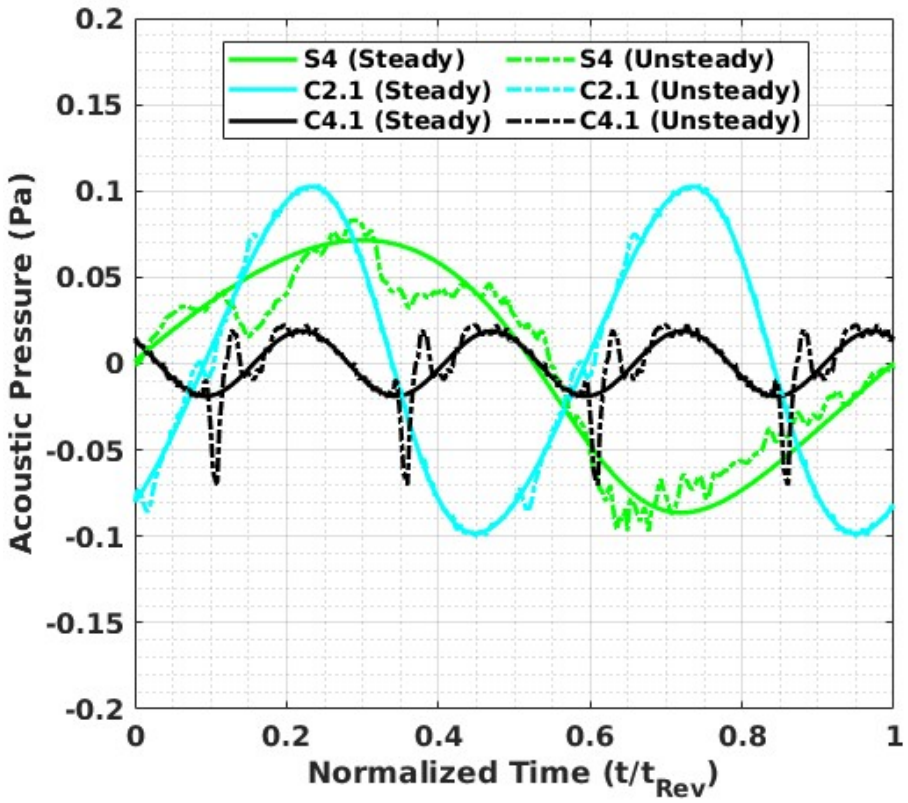

Figure 5.7: Loading Noise Waveforms (Steady vs Unsteady Loads) for Observer at $\theta = -30^\circ$ for Rotors S1, C2.1 and C4.1

Spectral decomposition of these waveforms is shown in Figure 5.8. While the unsteady loads produce a broadband noise signature, the impulsive unsteadiness of rotor C4.1 results in a high magnitude of the broadband spectrum. Due to the high frequency of the components of this noise, the perceived noise level of these components is very high, and is shown in the A-weighted

noise spectrum in Figure 5.8. Figure 5.8 also compares the loading noise frequency spectrum to the tonal noise component due to steady loading. The amplitude of high frequencies is very low for the steady load noise, resulting in pure tones.

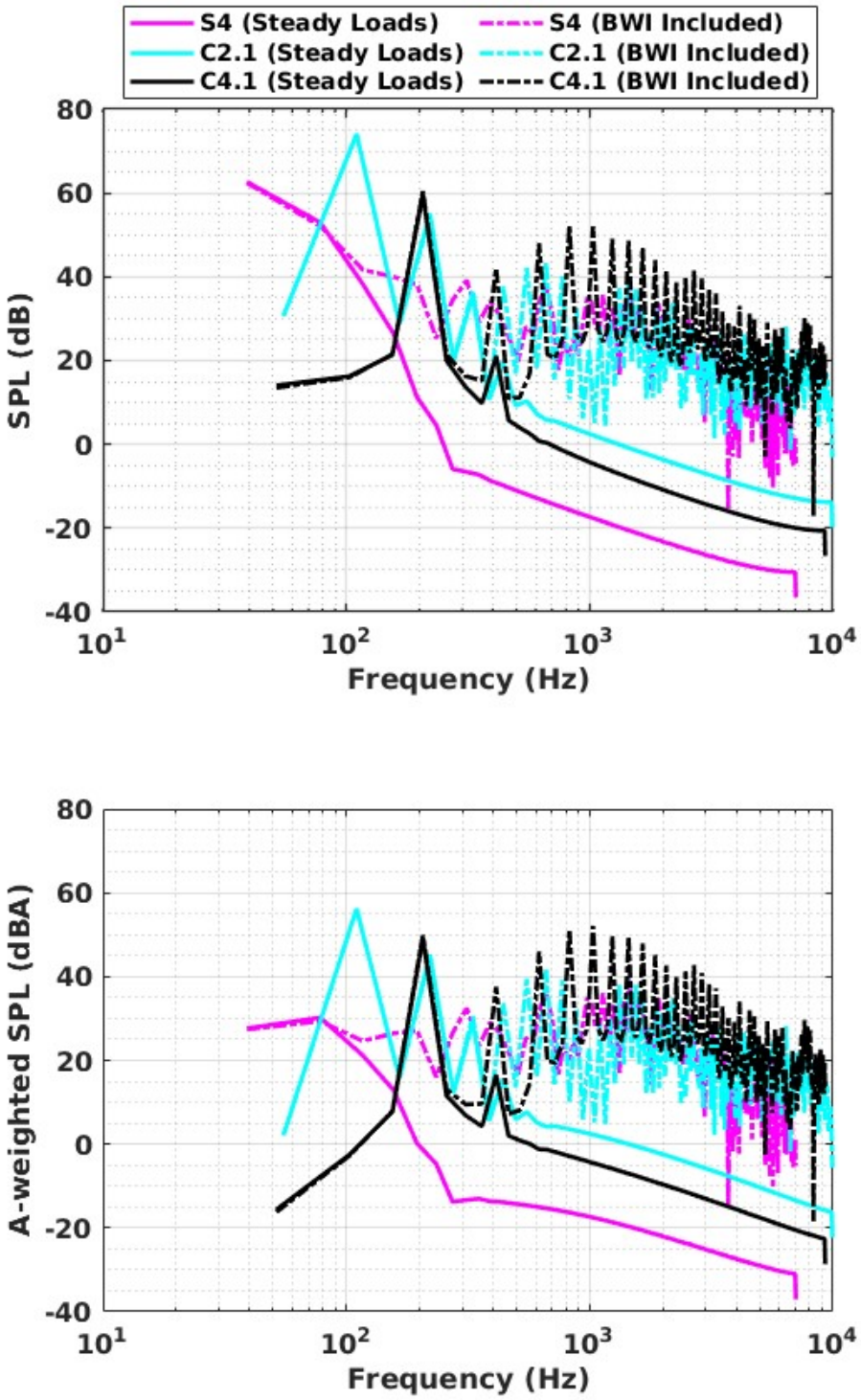

Figure 5.8: Spectral Decomposition of Loading Noise at Observer located at $\theta = -30^{\circ}$ for Rotors S4, C2.1 and C4.1, Top - Sound Pressure Level (SPL) and Bottom - Perceived Noise Level (A-weighted SPL)

The effect of multiple blades, i.e., higher blade pass frequency is seen in the corresponding perceived noise level spectrum in Figure 5.8, where the tonal loading noise due to screw S4 is perceived ~ 30 dB less than the true amplitude, while that of C4.1 is only ~ 10 dB less.

5.4 Total Noise (Thickness and Loading)

All the noise components of thickness and loading are superposed to compute the total noise at each observer location for all the rotors.

Figure 5.9 shows the variation of sound pressure level at each observer location, expressed in dB scale. Overall noise level is low for the rotor C4.2 (except on the rotor axis). However, screw S4 has similar noise levels as rotors C4.x. The rotors with 2 blades have higher in-plane noise levels.

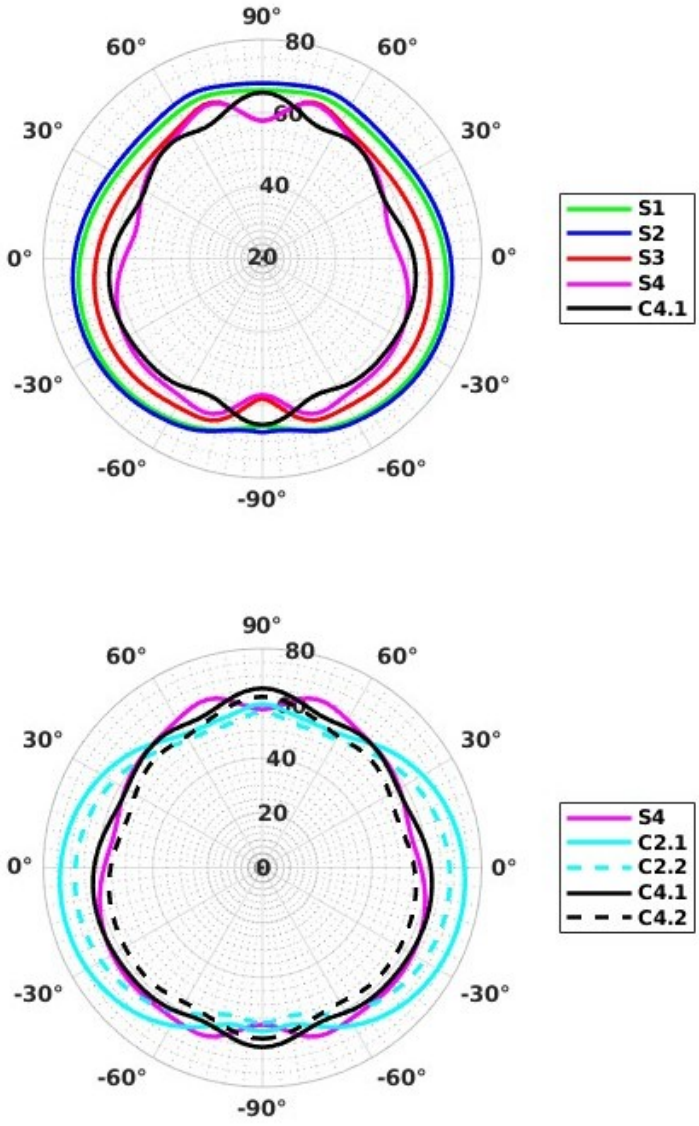

Figure 5.9: Total Noise Directivity for Different Rotors (SPL (dB))

Figure 5.10 shows the variation perceived noise levels, using A-weighting. The tonal components of the aerial screws are significantly attenuated due to their low frequencies, resulting in a unique noise directivity pattern for all the screws. The noise level is low both in-plane and on axis, and is highest at $\sim 15^{\circ}$ on either side of the rotor axis.

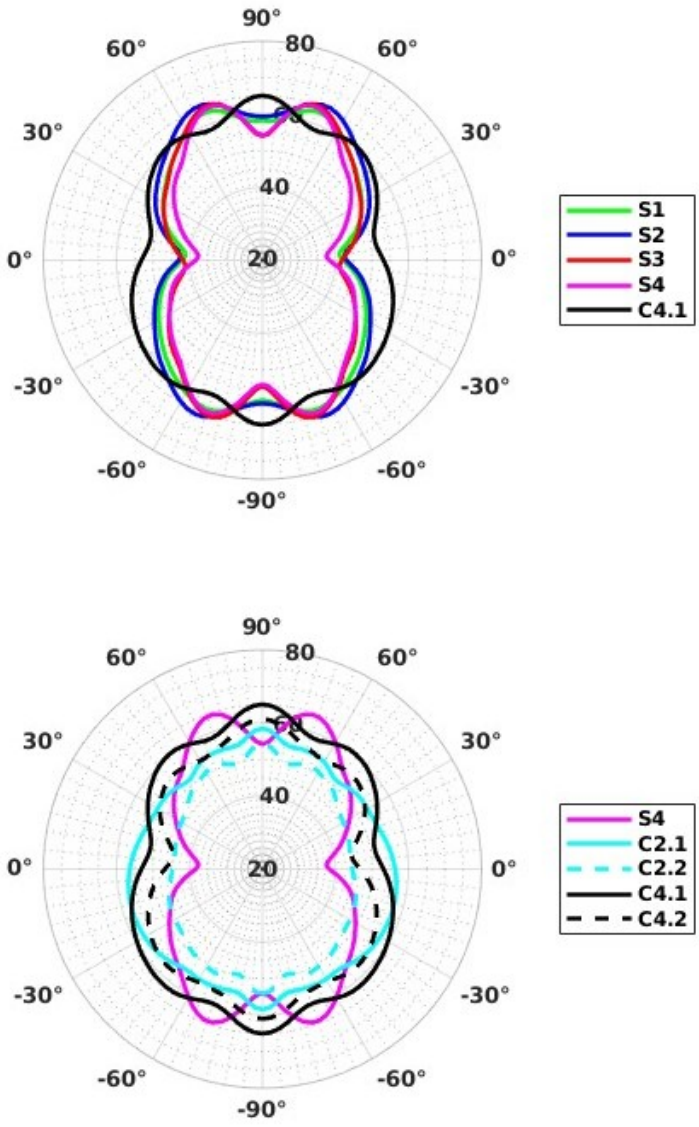

Figure 5.10: Total Perceived Noise Levels for Different Rotors (PNL (dBA))

The noise directivity pattern of the conventional rotors shows a maximum on the rotor axis, due to high frequency content from broadband loading noise. With rotors C2.x having non-impulsive BWI loads, the noise directivity pattern is more in-plane.

5.5 Chapter Summary

This chapter explored the aeroacoustics effects of aerial screw rotors, drawing comparisons to several conventional rotors.

Aerial screws were found to produce significantly higher thickness noise than conventional rotors due to their distributed geometry, creating interference between axially spread acoustic sources. However, because aerial screws operate at 1/rev blade passage frequencies compared to the higher Nb/rev of conventional rotors, A-weighted perceived noise levels favor aerial screws.

The best-performing bilinear screw (S4) produces loading noise comparable to the quieter 4-bladed conventional rotor (C4.1), and substantially less than 2-bladed conventional rotors. Aerial screws reached peak loading noise at a steeper declination (approximately 30 degrees) from the rotor plane than conventional rotors (approximately 15 degrees), reflecting the difference in how their distributed loads radiate.

The 4-bladed conventional rotor (C4.1) suffers from highly impulsive blade-wake interaction events — owing to its small chord and high blade loading — producing large, sharp pressure fluctuations with broadband content at high frequencies that are heavily penalized by A-weighting. By contrast, aerial screws interact with their wakes continuously and gradually throughout each revolution, resulting in a far less impulsive and perceptually quieter broadband signature.

When thickness and loading are combined and A-weighted, aerial screws exhibit a distinctive and favorable directivity pattern — quiet both in-plane and on-axis, with peak perceived noise concentrated around ±15 degrees from the rotor axis. Screw S4 achieves total noise levels comparable to the 4-bladed conventional rotors, while conventional rotors are loudest on-axis due to their high-frequency broadband BWI content.

Chapter 6: Discussion of Results

6.1 Discussion

This body of work presents a thorough investigation into the aeromechanics of aerial screw rotors, inspired by Leonardo da Vinci. Leveraging high-fidelity Computational Fluid Dynamics (CFD) simulations, this work investigates the influence of varying design parameters on the aerodynamics, performance, and aeroacoustics of aerial screws in hover, axial climb and off-axis climb states.

Linear and bilinear pitch and taper variations of one-bladed aerial screws are compared to two and four bladed conventional rotors to compare efficiencies, loads, and noise-signatures in various flight states.

6.2 Future Considerations

While the present studies provide a fundamental understanding of the aeromechanics of aerial screws, there are still several areas requiring further investigation. This collection of works presents a sole computational investigation of aerial screw aeromechanics. Preliminary experimental studies have been conducted yet thorough validation is still to be done for these specific studies [6].

Higher order shaping strategies are a promising avenue to explore in modifying pitch and taper rates. Moving beyond bilinear profiles, future studies can investigate varying pitch and taper functions gradually and smoothly to finely tune local incidence angles and vortex anchoring locations. Optimization techniques or inverse design strategies can be used to identify ideal geometries that maximize performance and efficiency.

One of the most promising areas for aerial screw application lies in the micro-scale or nano-UAV regime, where conventional rotor aerodynamics break down due to low Reynolds number effects, increasing viscous losses, and reduced airfoil performance. Aerial screws, with their vortex-based thrust, are naturally suited to this regime. Their high solidity and shape-conforming vortex structures offer a viable alternative when traditional blade theory is no longer applicable. Investigating aerodynamic performance at scales ranging from a few centimeters to tens of centimeters will be an important next step, particularly for applications in indoor surveillance, swarm robotics, and autonomous inspection.

6.3 Conclusions

These analyses reveal that the da Vinci vortex, a shape-conforming helical vortical structure at the screw's tip, is central to the thrust production in aerial screws through Computational Fluid Dynamics (CFD). This mechanism is similar to vortex lift phenomena observed in swept and delta wings, where it contributes significantly to pressure differentials across the screw surface, thereby enhancing thrust.

The effects of key design parameters—specifically screw pitch and taper—were systematically analyzed. Hover results indicated that increasing pitch initially improves performance by strengthening

axial thrust contributions, but beyond an optimal point, further increases lead to significant losses due to adverse projection of pressure forces. Similarly, variations in taper showed that while an initial aggressive taper strengthens the da Vinci vortex formation, excessive taper leads to a reduced effective lifting area and associated losses in aerodynamic efficiency. Bilinear variations of both pitch and taper were found to yield the highest figure of merit, achieving up to a 13% improvement over purely linear designs. In axial climb, it is found that the pitch rate has a dominant influence on the performance of aerial screws in axial flight in comparison to a variation in taper rate. Designs with high pitch rates perform better in climb states than in hover, but the increase in efficiency, FM^*, is limited. In similar fashion, the best linearly pitched and tapered aerial screw has a low pitch rate of $\zeta = 1.2$, and performance efficiency drops as the climb inflow increases. In off-axis flight, the pitch rate again dominated in effecting the forces and moments as functions of azimuth compared to the effect of the taper rate.

Wake analyses provided crucial insights into the aerodynamic efficiency of different geometries. Efficient screws exhibited rapid and coherent wake contraction within 50% of the rotor radius downstream, minimized swirl velocity near the root, and maintained a stable downwash region. These flow features correlated directly with improved FM values and confirmed that the wake structure is not merely a byproduct of geometry but an active indicator—and driver—of aerodynamic efficiency. This positions wake behavior as a powerful diagnostic and design tool for future aerial screw development.

In addition to aerodynamics, this study performed a detailed acoustic evaluation using both tonal and broadband noise components derived from CFD. Aerial screws, due to their distributed surface and thick chord geometry, exhibited higher absolute thickness and loading noise compared to conventional rotors. However, their blade-passing frequencies occur at much

lower harmonics (1/rev), which results in significantly attenuated perceived loudness under A-weighted acoustic scaling. Furthermore, the broadband loading noise in aerial screws is less impulsive and more spectrally diffuse than in conventional rotors—particularly when compared to 4-blade systems where blade–wake interaction (BWI) creates sharp, high-frequency acoustic peaks. These differences suggest that aerial screws, despite higher raw acoustic power, may offer superior acoustic stealth in urban or low-speed VTOL environments.

When compared to notional conventional rotors, aerial screws were found to produce lower FM values (by about 10–20%), largely due to geometric inefficiencies and non-optimized flow structures. The conventional rotor was found to have significantly lower amplitudes in force and moment oscillations compared to the bilinearly designed aerial screw in off-axis flight. The bilinearly designed aerial screw has higher lift and torque coefficients compared to the conventional rotor. For lift and torque, 1/rev and 2/rev frequency oscillations were not found for the aerial screw and conventional rotor respectively. Despite the fallbacks pertaining to the current state of the art of aerial screws, they also offer several offsetting advantages: (i) favorable perceived noise characteristics, (ii) simpler manufacturing of continuous helical geometries for low-speed applications, and (iii) opportunities for compact, high-thrust VTOL propulsion systems in size- or disk-constrained configurations.

Bibliography

[1] P.M. Lambermont and A. Pirie, *Helicopters and Autogyros of the World* (Barnes, 1970).

[2] B. Baden-Powell, "Experiments with Aerial Screw Propellers," *Aeronautical Journal*, Vol. 8, No. 30, pp. 28–32 (1904).

[3] G.E. Dorrington, H. Ogawa, J. McCarthy, and R. Carrese, "Simulation and Experimental Testing of Leonardo da Vinci's Helical Rotor," 19th Australasian Fluid Mechanics Conference, Mekbourne, Australia, Dec. 8–11, 2014 (2014).

[4] Leonardo Helicopters, "37th Annual Student Design Competition – 2019–2020 Request for Proposal (RFP) – Leonardo's Aerial Screw: 500 Years Later," Vertical Flight Society, 2019.

[5] J. Sutherland, R. Brown, E. Ebewele, E. Fisler, K. Krohmaly, J. Linkins, K. Marepally, A. Prete, I. Semenov, V. Nagaraj, I. Chopra, and A. Datta, "Leonardo's Aerial Screw: 500 Years Later," University of Maryland, 2020.

[6] A. Prete, V. Nagaraj, and I. Chopra, "Revolutionary Flight Vehicle Based on Leonardo da Vinci Aerial Screw: A Paradigm Shift in VTOL Technology," VFS Aeromechanics for Advanced Vertical Flight Technical Meeting, San Jose, CA, Jan. 25–27, 2022 (2022).

[7] A.C. Prete, *Revolutionary Flight Vehicle Based on Leonardo Da Vinci Aerial Screw: A Paradigm Shift in VTOL Technology*, M.S. thesis, University of Maryland, College Park (2022).

[8] S. Prakhar, J-H. Seo, and R. Mittal, "Aerodynamics and aeroacoustics of da Vinci's aerial screw," Physics of Fluids, September 12, 2025 (2025).

[9] Y.S. Jung, B. Govindarajan, and J. Baeder, "A Hamiltonian-Strand Approach for Aerodynamic Flows Using Overset and Hybrid Meshes," VFS 72nd Annual Forum, West Palm Beach, Florida (2016).

[10] E.C. Polhamus, “A Concept of the Vortex Lift of Sharp-Edge Delta Wings Based on a Leading-Edge-Suction Analogy,” NASA TN D-3767 (1966).

[11] M. Amiraux, *Numerical simulation and validation of helicopter blade-vortex interaction using coupled CFD/CSD and three levels of aerodynamic modeling*, University of Maryland, College Park (2014)

[12] Farassat, F., and Succi, G. P., ”The Prediction of Helicopter Rotor Discrete Frequency Noise,” *Vertica*, Vol. 7, No. 4, 1983, pp. 309–320.

[13] Ffowcs Williams, J. E. and Hawkings, D. L. and Lighthill, Michael James, ”Sound generation by turbulence and surfaces in arbitrary motion”, *Philosophical Transactions of the Royal Society of London. Series A, Mathematical and Physical Sciences*, Vol. 264, (1151), 1969, pp. 321–342. DOI: 10.1098/rsta.1969.0031.

[14] Fastl, Hugo and Zwicker, Eberhard, *Psychoacoustics: Facts and Models*, Vol. 22, Springer Series in Information Sciences, Springer, third edition, 2007. DOI: 10.1007/978-3-540-68888-4.